Synthesis and thermoelectric application of conductive polymer capped silicon nanoparticles and composites

Tiezheng Bian

School of Chemistry

University of East Anglia

Norwich UK

2017

A thesis submitted in partial fulfilment of the requirements for the degree of Doctor of Philosophy of the University of East Anglia.

Declaration

I hereby declare that this Ph.D. thesis and the work presented in it are my own, and have not been submitted by me for another degree at this or any other universities. Reference is made to all published work of other authors which I consulted.

Tiezheng Bian

Acknowledgement

Firstly, I would like to thank Yimin Chao, my primary supervisor, for his guidance and continuous support of my PhD study, for his patience, motivation, and immense knowledge.

Secondly, I would like to thank my colleges during this period, Dr Shane Ashby, Dr Qi Wang, Dr Jayshree Ahire, Rouxi Lui, Frederik Huld, Mehrnaz Behray, Ting Li, Ashley Marsh and Chenghao Yue for their friendship.

Thirdly, I would like to thank all collaborators at ISIS, NEXUS, as well as Upali A Jayasooriya (University of East Anglia), Michael J Reece (Queen Mary, University of London), Antony V. Powell (University of Reading) and Carl Redshaw (University of Hull).

Most importantly, I would like to express my love and gratitude to my parents for their support and encouragement in every way possible.

Finally, I would also like to thank The Alan Katritzky Scholarship for the support.

Abstract

A solution reduction synthesis method has been used to produce organic ligand capped silicon nanoparticles in a large scale, and with electrochemical etching method in comparison. Nanoparticles produced are explored in a variety of aspects, including particle size, elemental composition, thermal stability and optical property. These results are used to determine how different ligands could affect the silicon core and the thermoelectric performance.

Polymerisation of thiophene is studied to produce two types of oligomer capped nanoparticles, with the difference that whether the polymerisation happens before or after ligand capping. The order of reactions has an effect on the nanoparticle surface coverage of ligands, which influences other properties such as solubility and thermal stability.

Two types of polymer-capped SiNPs are applied in thermoelectric use via different paths. A terthiophene capped sample was prepared by cold press and work in room temperature (25 °C). The product is suitable for wearable device application due to its flexibility even after doping.

The other polymer capped sample is prepared by SPS with doping of graphene, and is aiming for high temperature (500 °C) applications.

Muon spin spectroscopy is involved during my research as a side project to study the microscopic conductivity between silicon nanoparticles with conductive ligand (phenylacetylene) as bridge. Both SiNPs and model molecule [tetrakis (2-phenylethynyl) silane] are studied using TF - μSR and ALC - μSR along with DFT calculation as theoretical support.

Table of contents

List of figures

List of schemes

List of tables

List of publications

Ashby, S. P., Bian, T., Ning, H., Reece, M. J., & Chao, Y. (2015). Thermal Diffusivity of SPS Pressed Silicon Powders and the Potential for Using Bottom–Up Silicon Quantum Dots as a Starting Material. Journal of Electronic Materials, 44(6), 1931–1935. https://doi.org/10.1007/s11664-014-3599-y

Ashby, S. P., Bian, T., Guélou, G., Powell, A. V., & Chao, Y. (2016). Ligand Doping on the Hybrid Thermoelectric Materials Based on Terthiophene-Capped Silicon Nanoparticles. Journal of Electronic Materials, 45(3), 1260–1265. https://doi.org/10.1007/s11664-015-3988-x

Bian, T., Peck, J. N., Cottrell, S. P., Jayasooriya, U. A., & Chao, Y. (2017). Hybrid Silicon Nanostructures with Conductive Ligands and Their Microscopic Conductivity. Journal of Electronic Materials, 46(5), 3221–3226. https://doi.org/10.1007/s11664-016-4954-y

Yang, W., Zhao, K., Bian, T., Chao, Y., Tamato, T., Xing, F., & Redshaw, C. (2017) Emission and theoretical studies of Schiff-base [2+2] macrocycles derived from 2,2′-oxydianiline, in preparation

Chapter 1 Introductions

Thermoelectric generator has the ability to convert heat into electricity and vice versa. It has been found as the perfect candidate in harvesting waste heat. Other applications such as converting radioactive heat into stable power source or assembling a mobile cooling or refrigerator system with no moving mechanical parts are in limited use or development.

Contents

1.1. Thermoelectric generator (TEG) and energy harvesting

1.1.1. Background

The “Energy crisis” is a topic that has been discussed for a long time. As we are reliant on fossil fuel for most of our energy consumption and the demand is still growing rapidly.[1] The discussion and concern regarding the time when fossil fuel would run out has been going on for centuries. In the meantime, the uneven distribution of resources geographically concentrates energy supplies in a very limited number of countries, some of them, politically unstable. This concern of not being able to get access to the energy supplies has led to conflicts or even wars between nations. Furthermore, emission of greenhouse gases from burning fossil fuels has been a serious issue for a long time. In return, the climate change has worsened due to our energy consumption.

With all the above in mind, the need for an alternative is in high demand. People are looking for a clean, renewable energy source. Sources that are also cheap and easy to access globally. There have been several ideas. Wind power and hydropower have been put into great use in certain places, the same with geothermal energy. Nuclear energy has always been considered as a future source and achieved so much, but the few historic accidents cause public concern with this technology. Solar energy is inexhaustible and so many methods have been developed to harvest the sunlight that has been shining upon us all even since the very beginning. Now a new proposal of thermoelectric energy harvesting is on the table as a new way of fighting the “energy crisis”. With the direct conversion of a temperature difference to electricity, there is no greenhouse gas emission and the resource is everywhere in both natural and man-made environments.

1.1.2. Applications

Following the steps of Benjamin Franklin, Michael Faraday and all the greatest electric scientists, we the human beings have been relying on the energy of electricity for a very long period of time. Based on Faraday's law, kinetic energy could be transformed into electricity by electromagnetic induction. It is the most commonly used method for generating electricity. Whether it is using fossil fuel, biomass or even nuclear, the combination of heat energy and a steam turbine generator is still the most efficient and reliable way of extracting energy, converting to electricity and transferring to wherever it is needed. However, this combination is not so efficient after all. With normal efficiency of less than 50% and higher temperature required for higher efficiency, the amount of energy going into waste in power plants is quite considerable, with most in the state of heat.[2-3] A cooling tower may serve the heat engine by maintaining the low temperature of the cold sink, but it still witnesses the waste of large amount of heat. If only there was a way of utilizing this waste heat.

This is where thermoelectric generator comes into play. With the ability of heat-electricity conversion with a layer of thermoelectric module, the thermoelectric generator would be leading a secondary energy extraction in power plants, targeting waste heat.

A thermoelectric generator is a solid structure with no moving parts. Unlike engine generator, the robustness of the device makes TEG very low maintenance. It means more flexible applications while using less space. It could be attached to all sorts of heat source to produce electricity such as waste energy. Unnecessary heating causes lots of trouble and inconvenience in all aspects of human activities, hence, thermoelectric generators would also be the perfect solution of putting them into good use. A well-constructed device named thermoelectric self-cooling module dedicates itself to prevent the problem

of overheating.[4] By utilizing the unwanted heat, converting to electricity and supporting the cooling system, the temperature will be under control without extra electricity consumption. Heat is also an energy source that could be easily accessed during human activity, but electricity is much more useful in modern society. The flexibility of TE modules provides a portable solution for conversion between these two. In the occasion of exploring unpopulated areas or simply living in places where electrical grid hasn't reached, a simply constructed TE generator will provide a basic supply of electricity without the influences of weather or time. Speaking of weather, thermoelectric generator is also a way of utilizing solar energy. It transforms the absorbed heat into electricity, sometimes alongside a photovoltaic generator. Solar energy is cheap and never going to be exhausted. And with the help of a thermal-concentrating device, TE generator would have a boost in efficiency.[5] Another type of small size TE modules had their eyes on wearable devices. Using body heat as energy source, a wearable electronic device would not need to be taken off for charging any more.[6] Outer space is another area where thermoelectric generator would be of great use. TE generators are not affected by essentially anything. It could operate in the back of a planet or outer rim of the solar system where solar energy is virtually non-existence. The ultra-low temperature of outer space would act as the perfect cold sink so that the efficiency would be in its prime. Radioisotope thermoelectric generators (RTG) are equipped in most space exploring vessels already as the durable and stable power output would support the projects in a basic level and as the last resort.[7]

By reversing the energy conversion direction, thermoelectric modules could be used for cooling as well. When comparing to compressor cooling, a refrigerator using TE cooling will have smaller functional parts and be much quieter. The advantages are much more

obvious in the field of portable cooling systems. Cooling box for picnic or organ transportation will be more efficient with a thermoelectric module installed.

Thermoelectric materials come in all sorts of categories. Alloys and other inorganic materials tend behave better in high temperature situations. While organic materials such as polymer and its composites might not be able to stand for high temperature but instead obtain other unique properties such as transparency and softness, which could contribute to some portable devices or even wearable devices.[8]

The efficiency of a thermoelectric generator is defined as the portion of new power output within the total heat input.[9] And the maximum efficiency is calculated as:[10]

$$\eta_{max} = \frac{T_h - T_c}{T_h} \frac{\sqrt{1+ZT}-1}{\sqrt{1+ZT}+\frac{T_c}{T_h}} \qquad (1.1)$$

where $T = \frac{T_h+T_c}{2}$, T_h, and T_c are average temperature, source temperature (hot) and sink temperature (cold), respectively. If figure of merit (ZT) was infinite, the efficiency of TEG would reach Carnot limit.

1.1.3. Thermoelectric effects

The dimensionless figure of merit, ZT, is used to describe the ability of a thermoelectric material to efficiently generate thermoelectric power, and it could be explained with the formula[11]:

$$ZT = \frac{\sigma S^2 T}{\lambda} \qquad (1.2)$$

where S is the Seebeck coefficient, σ is the electrical conductivity and λ is the thermal conductivity.

In order to improve the thermoelectric performance, a variety of properties are in need of optimization, some of them even in conflict. As shown in the equation, in order to

achieving a high figure of merit, a high thermopower and electrical conductivity, as well as a low thermal conductivity are in equally necessary. However, these figures are determined by interrelated material properties. By targeting each value one by one, methods are introduced to achieve better figure of merit.

1.1.3.1. Seebeck coefficient

Seebeck coefficient, also known as thermopower, is the quantity of measuring the thermoelectric voltage of certain material against a temperature difference through its bulk. The unit commonly used is microvolts per kelvin (μV/K). The name thermopower gives us a glimpse of what the property is, while the more official name, Seebeck coefficient, is related to the Seebeck effect, both in honour of Thomas Johann Seebeck.

The Seebeck effect is the direct conversion of heat to electricity, which is employed as one of two major functions using thermoelectric materials. A temperature gradient in a material induces the shift of charge carriers to disperse in an uneven way. With the temperature gradient applied onto the material, hot end obtains faster movement of the carriers than the other, causing further diffusion of the charge carriers. This builds up a higher density of charge carriers in the cold end, producing an electric potential to push carriers back to the hot end of the material. This diffusion of charge carriers qualifies as a current generated by an electromotive force, which is essentially what Seebeck effect is. The potential created by this electromotive force can be described as a function of the gradient in temperature (T):

$$V = -S\Delta T \qquad (1.3)$$

where V is the electric potential, S is the Seebeck coefficient, and ΔT is the gradient in temperature. When given an n-type material, the free charge appears to be electron, and the cold end shows a negative potential. If the free charges are positive, it will produce a

positive potential in the cold end. In the carriers' point of view, both n-type and p-type are welcomed but in separation. Mixed carriers will lead to a cancellation in induced Seebeck voltage.

As the formula suggests, Seebeck coefficient can be calculated by measuring the temperature difference and electric voltage between two ends of the material.

The Seebeck coefficient is defined using equation[11]:

$$S = -\frac{\Delta V}{\Delta T} \qquad (1.4)$$

where ΔV is the voltage difference and ΔT is the temperature difference between two ends.

However, the voltage shift cannot be measured directly using a voltmeter, as it shows not only the Seebeck effect of the target material but also the material used in making the leads of the instrument. Alternatively, the relative Seebeck coefficient is introduced as the electrodes are inevitable. By arranging a thermocouple, the thermoelectric voltage of the material and the electrodes are measured at the same time. The resulting measurement of Seebeck coefficient contains two parts:

$$S_{measure} = S_{electrode} - S_{bulk} = \frac{\Delta V_{electrode}}{\Delta T} - \frac{\Delta V_{bulk}}{\Delta T} \quad (1.5)$$

Using a material with known Seebeck coefficient as electrode, the value of the material in discussion would be calculated afterwards.

In the case of the mentioned known Seebeck coefficient of certain materials, the absolute Seebeck coefficient is needed so that a valid reference could be established. In order to measure the absolute Seebeck coefficient, the Thomson coefficient (μ) is utilized. Due to the nature of Seebeck effect, the Seebeck coefficient will be zero when the temperature

is set at absolute zero. With that in mind, the absolute Seebeck coefficient is obtained according to the equation with the value of μ[11]:

$$S(T) = \int_0^T \frac{\mu(T')}{T'} dT' \quad (1.6)$$

In practice, there are several ways of altering the Seebeck coefficient of one material, mainly in the aspect of tuning charge carrier diffusion status. With the charge carrier also determining the electrical conductivity, two parameters change at the same time, sometime in opposite directions. Under the circumstance, the power factor is introduced to determine the usefulness of the material in a thermoelectric application. The value is perfect in sufficiently monitoring the improvement due to the tuning of charge carriers. As part of the figure of merit ZT equation,

$$Power\ factor = \sigma S^2 \quad (1.7)$$

where S is Seebeck coefficient and σ is electrical conductivity.

A higher power factor means the material tend to generate more energy. But a high efficiency is not guaranteed. For that, thermal conductivity of the material must be put into consideration. Essentially, a good thermoelectric material would have a higher power factor and a lower thermal conductivity.

1.1.3.2. Thermal conductivity

Thermal conductivity is the ability of transporting heat through the material. The process is conducted by phonons and electrons, in which phonon transport mode takes a major role in the development of a thermoelectric material as a higher portion of electron transport mode indicating a lower Seebeck coefficient. The phonon movement is also described as lattice wave, which is largely affected by the lattice defects.

$$\lambda = \lambda_L + \lambda_e \quad (1.8)$$

Nano structuring of the materials is one of the most commonly used and efficient way of manufacturing a better thermoelectric material. As mentioned before, phonon takes a huge role in conducting heat. The phonon possesses a mean free path of 500 nm or longer.[12] On the other hand, electron has a mean free path in a much smaller scale. When materials are reduced into nano scales, the cut-off in phonons causes a reduction in thermal conductivity while the electrical motions stay the same. In the case of silicon, doping with boron or phosphorus contributes to the considerable decrease of thermal conductivity in a similar manner due to its impact on phonon scattering at the impurity atoms.[13]

1.1.4. Device assembly

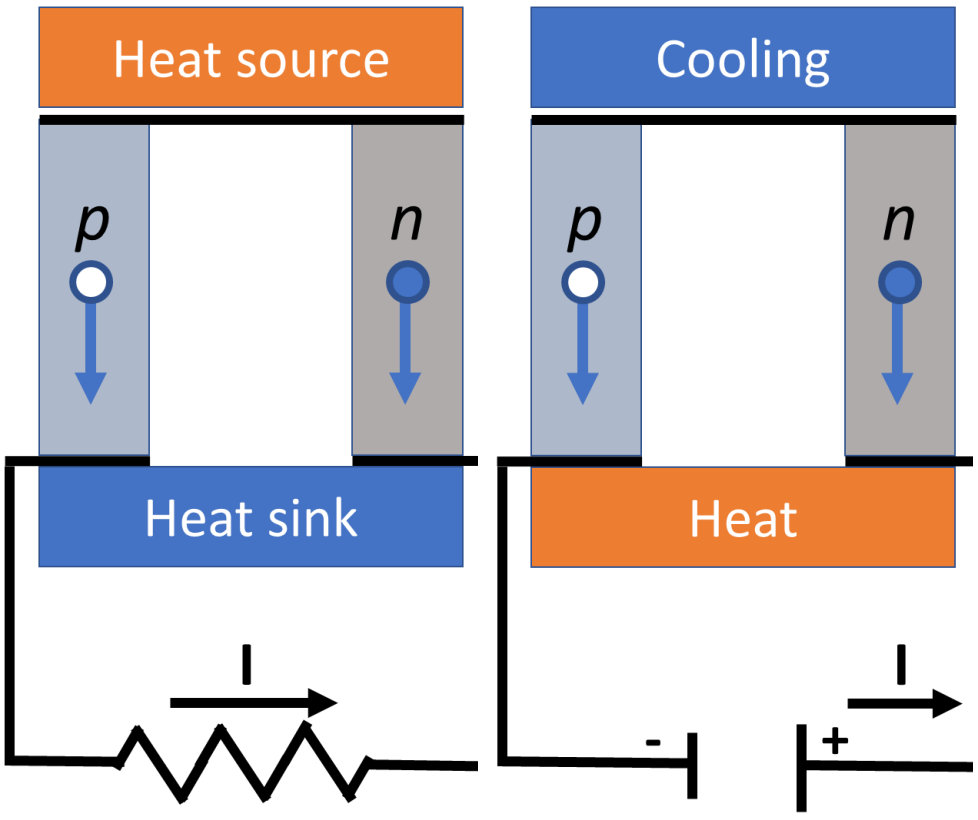

Figure 1 Thermoelectric couple

Figure 1 shows a thermoelectric couple assembled with both n-type and p-type materials.

When connecting the hot end of the two types of materials electrically and a load across the cold end, the potential induced by the Seebeck effect will produce a current flow through the load, making the device an electrical power generator.

When applying an external potential onto the unit, the charges are forced to move from one end to the other. With the heat carried by the charges, a steady heat flow is produced by the unit, named Peltier cooling.

A thermoelectric module contains a set of TE couples (Figure 2**Error! Reference source not found.**).[14] By adding external electrical cables and substrates on both sides of the thermoelectric elements, the module could be sealed and ready for use.

Thermoelectric modules are constructed in various methods to achieve different size and shapes for specific purposes.

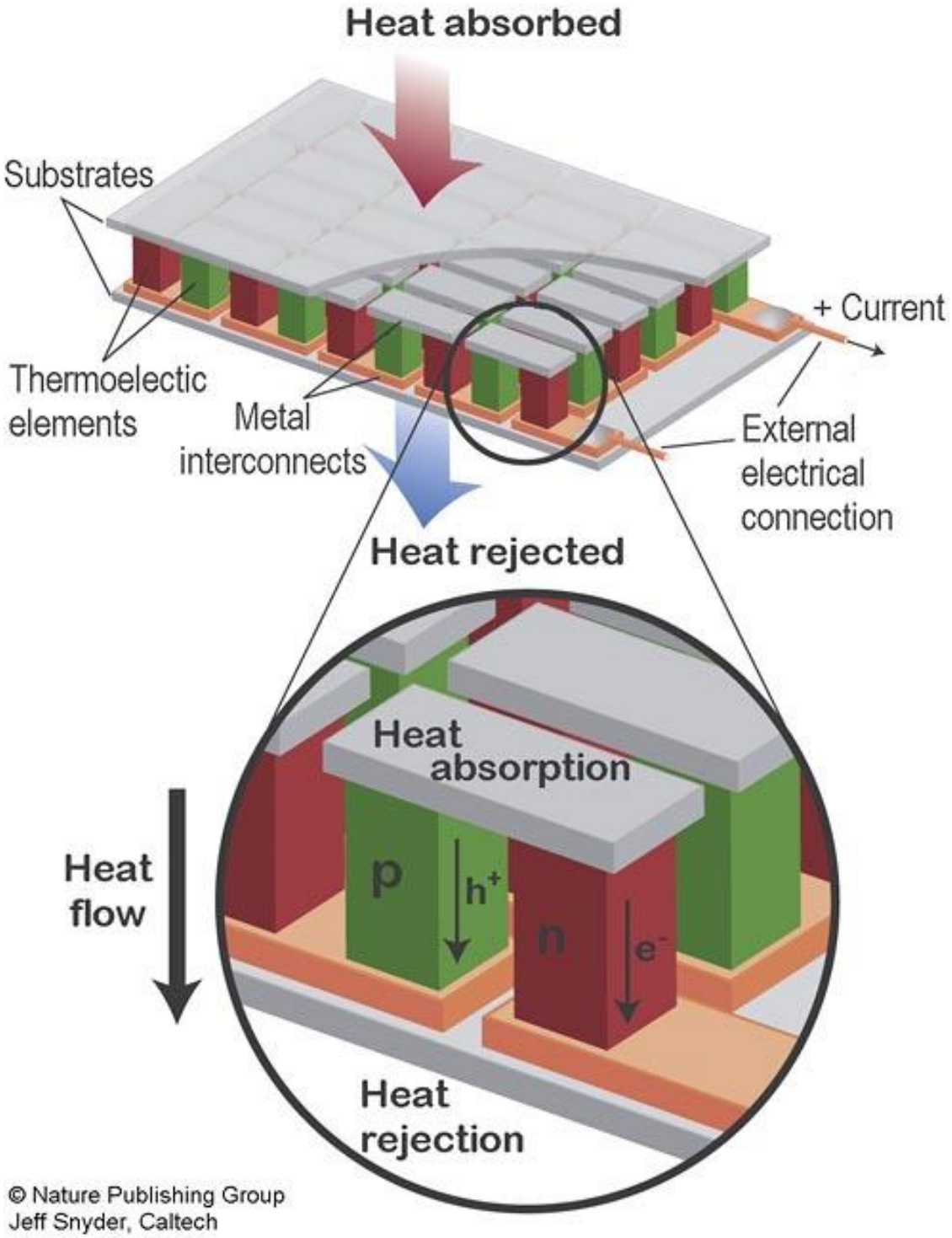

Figure 2 Thermoelectric module for electricity generation[14]

In the field of automobile waste heat recovery, a relatively large size system would be used as weight is not a problem. Zhang et al.[15] have assembled TEG modules with a size of 2.7 by 2.7 cm using small uncouples and the whole system containing 400 of them to achieve sufficient power for real life applications. The chosen materials, nanobulk half-Heuslers, behave well in high temperature due to the nature of engine exhaust.

A TE module is not necessarily assembled by putting thermoelectric couples into a package. With laser cutting and thermal spray techniques, a module with multiple TE legs could be manufactured with ease.[16] This method would strengthen the structure of the modules and save space at the same time.

In some applications, a thermoelectric module is needed to be thin and flexible. With their target at wearable devices, a series of film or ribbon type TE modules are developed to serve as the case.[6, 17-18]

With custom-made fabric as substrate, Mahmud et al.[19] have avoided the fabrication of individual TE couple as well, while put together a flexible module for wearable use. By knitting silver thread into the fabric as conductor between TE legs, the structure is further simplified.

The assembly of several layers of thin films could also provide a wearable TE module.[6] With the printing of not only TE materials but also conductors, this method gives an insight into the automated mass production of TE modules.

The key in fitting TE module into various circumstances is to choose the right substrate type, dimensions and working temperature, and most importantly, the choice of materials.

1.2. Thermoelectric materials

1.2.1. Inorganic materials

Bismuth telluride alloys are the most commonly used thermoelectric materials. They are used in building most commercial devices.[20] A reported ZT of close to 1 was half a century ago with bulk Bi_2Te_3, showing its long-standing advantage in the field of thermoelectric applications.[21] With the solid solubility within Bi_2Te_3, Sb_2Te_3 and Bi_2Se_3, a series of alloys show similar or higher ZT than Bismuth Telluride in different temperatures between 100 to 300 K.[22] With undoped Bismuth Telluride being a p-type material, its Seebeck coefficient is corresponding to the concentration of telluride.[20] When the amount of telluride increases, Seebeck coefficient decreases until it becomes n-type. With this type of property, simply doping of the material could generate a working thermocouple and then a working module.

More recently, with the discovery of size dependent thermal conductivity coefficient, nanotechnology has been used to develop new TE materials. At the same time, old fashioned materials have been modified as well to achieve a better performance.

Ball milling followed by hot pressing is a popular way in fabricating nanostructure materials from bulk. Using this technique to manufacture alloys would be a step further in the developing of TE material more efficiently.[20]

Superlattice is another powerful approach. With the ability to control transports of phonon and electron, significant advances in superlattice based devices have been made.[23]

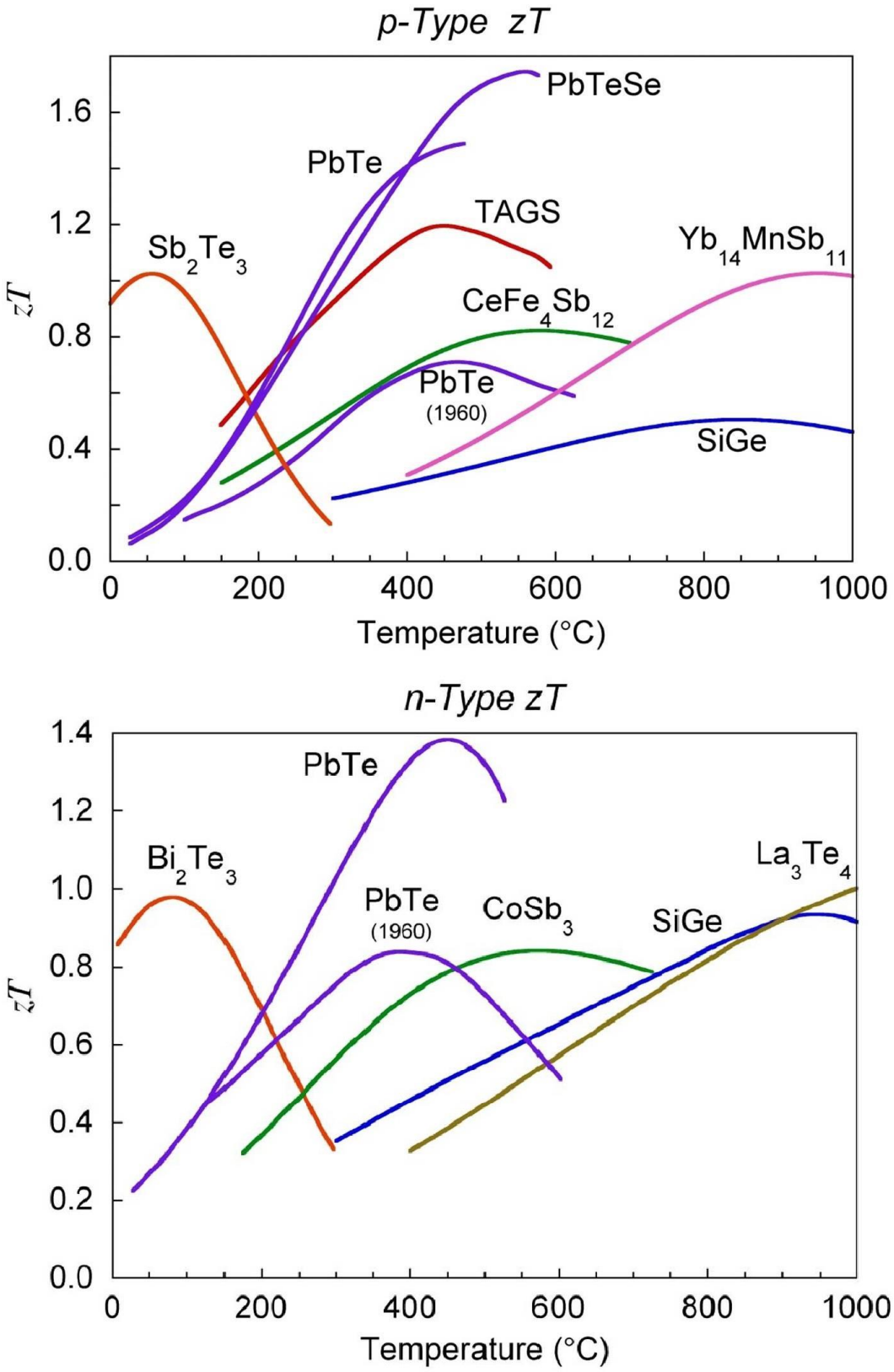

Figure 3 ZT of inorganic materials depending on temperature where most materials show increases in TE performance with temperature rise until peaks reached. [14]

With the absence of bismuth, group IV elements still show great potential when combining with telluride or germanium. PbTe and SiGe based materials could achieve good performance in higher temperatures (above 500 K). [14]

PbTe is another traditional TE material used in commercially available devices. It is easily altered, with impurities known as dopants, into both n-type and p-type materials. Doping changes the band structure near the Fermi level.[24] The dopant tunes the carrier concentrations inside the material, but it also might reduce the crystal symmetry of the material which has further influence on the performance.[25] The crystal symmetry has direct effect on electronic density of state and bandgap. The manufacture of lead telluride quantum dot superlattice is a current way of altering the material, resulting in a lower lattice thermal conductivity and in turn an improved ZT.[26]

SiGe holds the best performance of the three traditional materials in high temperature range, leading to a role in the radioisotope thermoelectric generator. Nano structuring makes this a highly promising material due to the reduction in its thermal conductivity.[27-28] Furthermore, this approach expands its peak performing temperature range. With the micro-fabricated modules in development, silicon germanium alloy has potential in other fields of applications operating in room temperature.[29]

Skutterudite is one type of antimony-based compounds with promising thermoelectric potential.[30] Upon doping, both n-type and p-type skutterudite material could be manufactured due to its special crystalline structure. This structure contains voids which can be filled with rare earth elements and reduce thermal conductivity during the process due to increasing lattice phonon scattering. [31] Multifilling with La, Ba, Ga, and Ti will produce *p*-type skutterudite, and Yb, Ca, Al, Ga, and In are required in *n*-type skutterudite.

The skutterudite is reported to have capability in temperature range higher than commercially available bismuth telluride.[32]

$Yb_{14}MnSb_{11}$ is another one of the newly-developed materials in thermoelectric field. Zintl compound possesses a naturally low thermal conductivity. As a highly promising p-type material, $Yb_{14}MnSb_{11}$ is also doped to alter carrier concentration for better performance. Lu doping[33] is a successful approach with an increase in electrical conductivity. This material is a potential replacement for SiGe, which operates in the high temperature range.[34]

1.2.2. Organic materials

With advantages such as low toxicity, low cost and easy fabrication, organic polymers have been given more attention as a type of potential thermoelectric materials.

There are several types of conductive polymers which are suitable candidates for thermoelectric applications, such as polyaniline(PANI), polypyrrole(PPy), polyacetylene(PA) and polythiophene(PT) derivatives.[35] The low thermal conductivity of polymers is an advantage in the field of thermoelectric materials. With the right amount of doping, an increase in electric conductivity could be achieved in order to hit a higher figure of merit. Noting that the doping level will also affect the Seebeck coefficient of the material as the higher charge carrier density can cause a decrease in the property.[11, 35-37]

Commonly, polymers undergo degradation above 300 °C which results in a limited field of applications. However, their flexibility is an advantage over inorganic materials. Polymer based thermoelectric modules are easy to process and could fit anywhere. There is also the option of transparency.[11, 37-38] For instance, organic thermoelectric module

could be manufactured by a simple step of moulding.[11] Scaling up and mass production would not be an issue with this method.

Polythiophene is the backbone of many organic thermoelectric materials with top performances such as poly(3-alkylthiophene) (P3AT) and poly(3,4-ethylenedioxyselenophene) (PEDOT). The conjugated structure of the material holds a high charge density as well as high mobility of charge carrier, thanks to the n–π* electronic transition and π–π stack structure within the material.[39]

During the exploring of doping which holds the balance between Seebeck coefficient and electrical conductivity, two doping methods are utilized. One way of fabricating poly(3,4-ethylenedioxythiophene) polystyrene sulfonate (PEDOT: PSS) is by a two-step method of doping and dedoping.[37] The doping (oxidation) gives an increase in electrical conductivity but also a drop in Seebeck coefficient. The second step reduce the charge carrier density and pull the Seebeck coefficient back up with only minor effects over electrical conductivity. Besides PSS, other counter-ions have been used.[36] A secondary doping step instead of dedoping could also help achieve a better figure of merit.[40] The increasing ratio of PEDOT in the bipolaron states ensures a rise in electrical conductivity as well as Seebeck coefficient.

PEDOT: PSS is one product which attracts major attention due to its water solubility as well as its transparency.[37] There are also polymer blends based on this. A novel nanofilm of PEDOT: PSS and PT/P3AT bilayer is made with the intention of increasing electrical performance by quantum effect.[41]

Polymer could also be the part of a composite. The addition of carbon is one common solution for higher electrical conductivity. A composite of polythiophene and multiwalled carbon nanotube is fabricated to get a boost in electrical conductivity with

only slight changes in Seebeck coefficient and thermal conductivity.[42] In the case of the composite of poly(3-octylthiophene)(P3OT) and carbon fibre,[43] the combination of high Seebeck coefficient of polymer and high electrical conductivity of carbon presents a promising product. A similar situation occurs with poly (3-methylthiophene methine)s(PMMs) and graphite composite. The preparation also provides a new method of solution mixing.[44] Another well-developed mixing method is in-situ polymerization in solution, where low-dimensional carbon material such as graphene or carbon nanotube are effective additives for PEDOT: PSS.[45] The strong electronic interactions between polymers and nanostructured carbon improve electrical conductivity.

1.2.3. Silicon based materials

As a semiconductor and an abundant element in the earth crust, silicon has been investigated for all sorts of applications. In the field of thermoelectric materials, it is also a candidate for a sustainable material for the future. As an undoped bulk material, silicon possesses a very high Seebeck coefficient (440 μV/K), which gives a huge advantage prior to the further modification.

With the thermoelectric performance determined by figure of merit, a high Seebeck coefficient is not the only parameter to consider. With that being said, the electrical conductivity of undoped silicon is not high enough for a high-performance TE material, and the thermal conductivity is too high.

As a well-known semiconductor, improvement in electrical conductivity is hardly a problem. Both n-type and p-type doping techniques are very well-developed, which is essential for TE applications, as a module needs both to work, preferably with ZTs in the same level. However, with an existing interrelationship between doping and its Seebeck coefficient,[13] blindly increasing doping level is never a good idea. The increase of charge

carrier will significantly reduce the Seebeck coefficient, which, as mentioned before, is a large advantage for a semiconductor like silicon. Of course, in rare case, a simultaneous increase of both electrical conductivity and Seebeck coefficient could be achieved.[46] But for most scenarios, a balance must be found between modified electrical conductivity and Seebeck coefficient.[47]

The major shortcoming that is keeping silicon becoming an effective TE material is the thermal conductivity, which is hundred-fold higher than Bismuth Telluride.

Luckily, as a conquest during improving figure of merit for most inorganic TE materials, there is not a shortage of methods in decreasing thermal conductivity of the material. In the case of silicon, which has the diamond like lattice structure, heat transfer within the bulk mainly relies on phonons rather than electrons. As a result, enhancement of phonon scattering becomes the obvious solution.

Doping of bulk silicon is the first way of many. With boron or phosphorus atoms imbedded in the bulk material, these impurities cause the phonon scattering.[48-49] The increasing electron density in the doped material would induce phonon scattering as well.[49]

The most commonly exploited method in phonon scattering is by creating grain boundary in the material. Reducing thermal conductivity by nano-structuring materials gives the entire industry a huge boost as the mean free path (MFP) of phonon is investigated. Nano materials scatter phonons with size smaller than the individual phonon MFPs.[50] With the MFP distribution of silicon measured, it is discovered that majority of heat is carried by phonon with MFP more than 100nm.[51]

Phonon scattering occurs on the grain boundary in nanostructured silicon materials, preventing/slowing heat flow through the whole bulk.

The most straightforward way of fabricating nanostructured materials is by sintering nano powder into a bulk. This is also an effective way of making alloys or composites. Gas phase synthesis is a clear choice when it comes to manufacturing nanostructured powder. Microwave plasma is a universal way of producing nano-size doped silicon, silicon/silicide composite or Si-Ge metallic nano alloy.[52-53] With the nanoparticle diameters varying between 10 to 20 nm, the grain sizes are well below phonon MFPs. Spark plasma sintering could produce alloys with better mechanical as well as thermoelectric properties by simply mixing elemental powders with desired ratio. Various grain sizes could be seen by SEM in the product with visible borders, where phonon scattering occurs.[54]

By employing silica as an outer layer of silicon nanocrystalline, improvement was achieved as silica obtains a similar thermal conductivity as glass.[55] Behaving as a more efficient grain boundary as amorphous silica layer further scatters phonons. However, the silica also blocks the electron from moving around effectively. With that in mind, a nanowindow between nanoparticles are established to utilize the silica without compromising the original electrical conductivity.[56]

Nanowires are another way to approach in creating silicon nano materials. Nanowire have been examined as both individual wires and arrays.[57-60] With detailed investigation upon individual nanowires show hundred-fold decrease in thermal conductivity comparing to bulk silicon.[57-58] Nanowire synthesis is easily scaled up to produce arrays of suitable dimensions,[57] which cannot be said when dealing with a lot of other materials.

A number of studies have investigated how modification of silicon nanowires affect the thermoelectric properties. A variety of diameters of wires are synthesized using different methods and experimental conditions, from 10nm to 50nm.[57, 59] Further modification of

nanowires has an impact on thermal conductivity as well. Roughened surfaces of the nanowires suppress the heat flow within the material by mimicking amorphous material, causing phonon boundary scattering to increase.[57] Similar results appeared when adjustable porosity was introduced into silicon nanowire arrays.[60] Chemical etching method provided a convenient way of manufacturing nanowire arrays with various controllable pore size and wire length, which have a visible effect on thermoelectric properties.

Silicon nano film or membrane is the obvious next option. With the computer simulation utilizing density functional theory and Boltzmann transport equation, it appears the nano-size thin film contains less charge carriers, which causes the reduction in thermal conductivity but also a Seebeck coefficient and electrical conductivity comparable to the bulk material.[61] As a result, an optimized figure of merit is obtained with a system difficult to scale up. Sputtering is a practical and efficient way of fabricating nano film material with all sorts of elemental combination. With the formation of Si-Ge alloy, phonon scattering at grain boundaries ensures a decrease in thermal conductivity.[62]

1.3. Nanomaterials

Silicon is not a particularly good material for thermoelectric applications. However, nanotechnology comes to rescue this abundant element from not being able to participate in this new generation of energy conversion devices

1.3.1. Introduction and quantum confinement

Quantum confinement is a concept mentioned extensively when talking about nanomaterials.[63] The effect takes place when the scale of a material is reduced to a size that the energy band structure is affected. When one dimension of a particle is near or

even smaller than the Bohr exciton radius, the particle will no longer be able to move around freely, hence the name confinement. As the confinement happens, the energy states become discrete and bandgap size-dependent. It also explains the blue shift occurs in nanoparticles.

With electrons confined in different numbers of directions, the quantum confinement structures are classified into quantum wells, quantum wires and quantum dots, corresponding to the confinement in one, two and all three directions respectively.

By exploring the density of electronic states, the influence of confinement becomes clear. The density of states is the number of states in a certain energy level that is occupied by electrons. With a bulk material, the density of states appears to be continuous. It gets quantized as more number of dimensions are confined, shown in Figure 4.

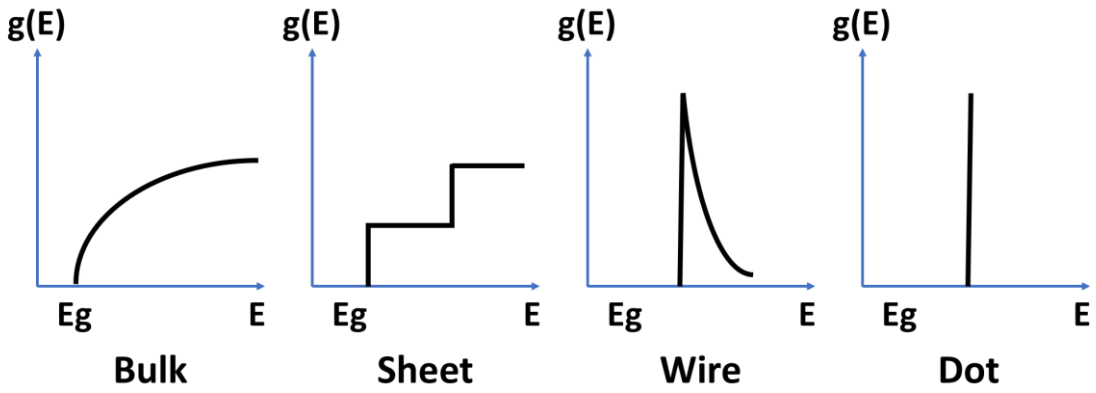

Figure 4 Density of states in semiconductor

As a result, nanomaterials tend to possess electronic, magnetic or optical properties different from the bulk material. The exceptionally small-scale structure also means the relative surface area is larger than other materials, which leads to improvements in strength, reactivity and absorbency.

Some specialties of nanomaterials have been utilized for a very long time in human history, from nanotubes in Damascus steel[64] to metallic nanoparticles in glazes of pottery.[65] Ancient civilisations may not know the microstructure or the energy states, but the advantages brought by nanomaterials are hard to ignore.

1.3.2. Developing nanomaterials

With so many advantages in theory, the development of nanomaterials has been going on for quite some time. Nanomaterials are represented a wide variety of fields, using a wide array of different materials, for use in all kinds of applications. Here are some of the wider studied materials with multiple applications not only in research but also in everyday life.

Generally, gold nanoparticles are synthesized by chemically reduction of chloroauric acid ($HAuCl_4$). The most common reductant in use is sodium citrate.[66] During the process, reflux is required for the formation of particles, for particle growth happens during boiling. The alteration of reaction duration often affects the product. Size of nanoparticle also varies as the concentration of reducing agent changes, which in turns affects the colour of the resulting solution.

Producing multi-shape gold nanoparticles is achieved in aqueous solution as well.[67] All different products are manufactured with essentially the same method with a bit tweaking on the contents within the solution for particle growth, triangular, cubic and hexagonal shapes are formed.

The surface modification takes a huge role in developing nanoparticles and thiol group is often selected as the terminus for attaching an organic functional group onto the gold nanoparticles. The surface reaction could take place simultaneously as the nucleation and growth of the nanoclusters.[68] The low cytotoxicity of gold nanoparticles introduces the material into the field of pharmaceutical development. Simply utilizing EPR effect, gold

nanoparticle can penetrate blood vessels and attach onto tumour cells, making it an efficient drug carrier.[69] Polyethylene glycol (PEG) is often decorated on particle surface in order to prevent reticuloendothelial system-mediated clearance. Another application in treating cancer is the manipulation of the optical properties of the nanomaterial. Gold nanoparticles could act as a sensor for detecting cancer cells even in early stage of the disease.[70] The fluorescence of the nanoparticle can be distinguished from the one of tissues, and the large relative surface area ensures the high concentration around targets. Drugs are not the only thing that gold nanoparticles can carry. Biomolecules such as peptides, proteins ,and nucleic acids could use this carrier for therapeutic reasons.[71]

Single-walled carbon nanotube (SWCNT) possesses a structure of a sheet of rolled graphene. There are three different types depending on the chirality, namely armchair, zigzag and chiral.[72] Each type has a different bandgap from the other, even with the same diameter. With the sensitivity between electronic property and chiral structure, a synthetic method to control the type of product is essential to the material transformation from experimental to practical. The chirality is characterised by an (m, n) index, describing the lattice vector along which the graphene sheet is rolling. A single chirality in the manufacture of SWCNT would bring out the highest potential in the desired property.[73] However, a mixture of different types of nanotubes will be synthesized in most occasions. There are three main methods utilised in the synthesis of carbon nanotubes, arc discharge[74], laser ablation[75], and chemical vapor deposition (CVD) synthesis.[76] The first two methods heat up pure graphite to evaporation temperature by employing high energy source and protective gas. The CVD method is conducted at a relatively lower temperature with hydrocarbon as carbon source. Multi-walled carbon nanotubes (MWCNT) contain more than one layer of graphene-structure wall. The multilayer structure gives MWCNT high tensile strength properties which are novel to SWCNT,[76]

making it a suitable choice in fields where a strong but light-weighted material is required. When used in bulk materials such as carbon reinforces resins, which rely on its mechanical properties, MWCNT are also known as hollow carbon fibre. In these applications it is a similar or better substitute to carbon fibre.[77] However, some CNT also possess high electrical conductivity which can be of great use.[78] When adding in their flexibility and transparency as a nanomaterial, carbon nanotubes can be made into conductive films when combined with polymers.[79]

With tuneable diameter and length, CNT is a fine material for encapsulation of other substance.[77] Various composite products are used as catalysts[80] or electrodes[81].

1.4. Conductive polymers

Organic compounds such as polymers, are not a good candidate when it comes to typical electronic applications. Polymers like rubbers and plastics are used as electronic wrappers and enclosures for a long time and still unreplaceable. The property that makes them ideal for this is their electrical insulation.

However, the development of conductive polymers, more specifically the intrinsically conductive polymers (ICPs), is a booming industry. Conductive polymers as well as conductive polymer composites (CPCs) are new candidates in the field of energy storage and conversion.[82] Conductive polymers, though not being thermoplastics, are easily processed to fit the desired function and form.

The conductivity of polymers comes from their π-conjugated polymeric chain. As shown in Figure 5, there are two main types of polymer backbones supporting this property, the polyene type such as polyacetylene and the aromatic type such as polypyrrole (PPy) and PEDOT-PSS. And there is polyaniline (PANI) which sometimes falls into the latter type

but with N in the outside of the aromatic cycle leading to indirectly linked cycles. However, the performance can be equally good.

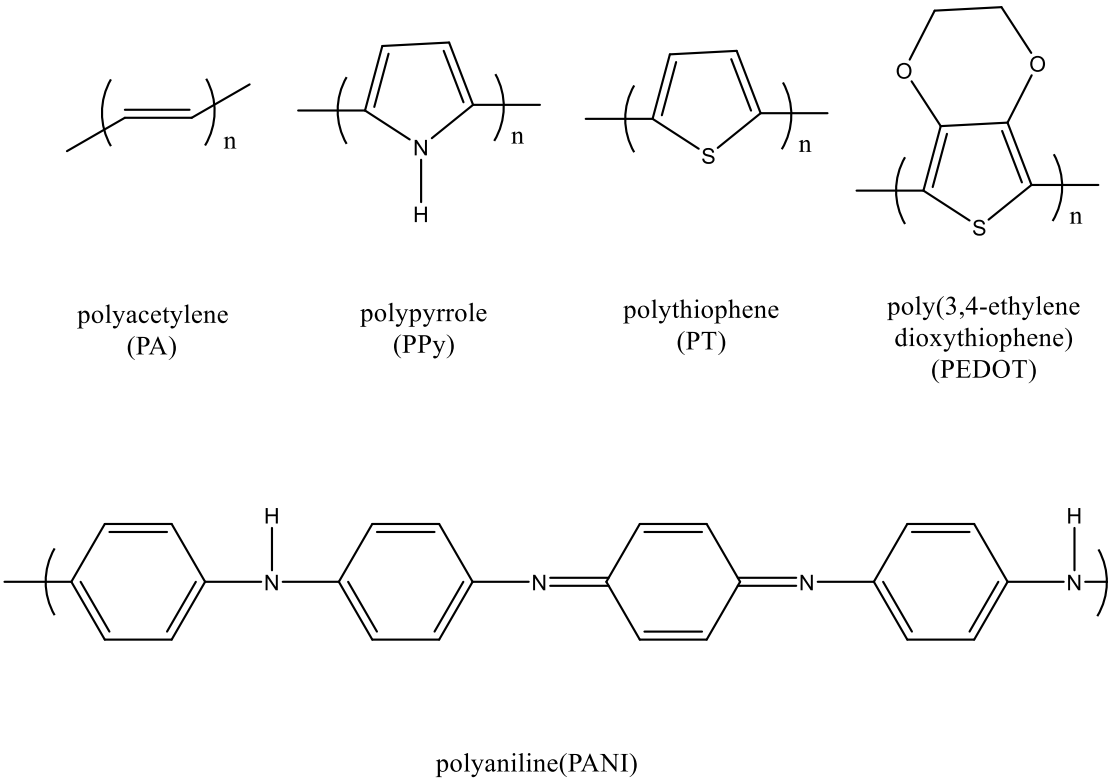

Figure 5 Examples of conductive polymers

In polyacetylene, the charge is conducted by conjugated double bonds. The π-orbitals can be described as shown in Figure 6. Ethylene possess a band gap of 6.7 eV. When a π-conjugated system of double bonds is formed, the band gap between HOMO and LUMO shrinks with butadiene of 5.8 eV and octatetraene of 3.1 eV. The polyacetylene, which contains an infinite length of conjugated system, has a band gap of 1.5 eV.[83] This band gap is similar to the GaAs (1.4 eV) and Silicon (1.1 eV), which are well-known semiconductors. The original value of conductivity is only 10^{-10} to 10^{-8} S/cm. However, with lightly doping, the electrical conductivity of polyacetylene can increase several orders and reach 0.1 S/cm.

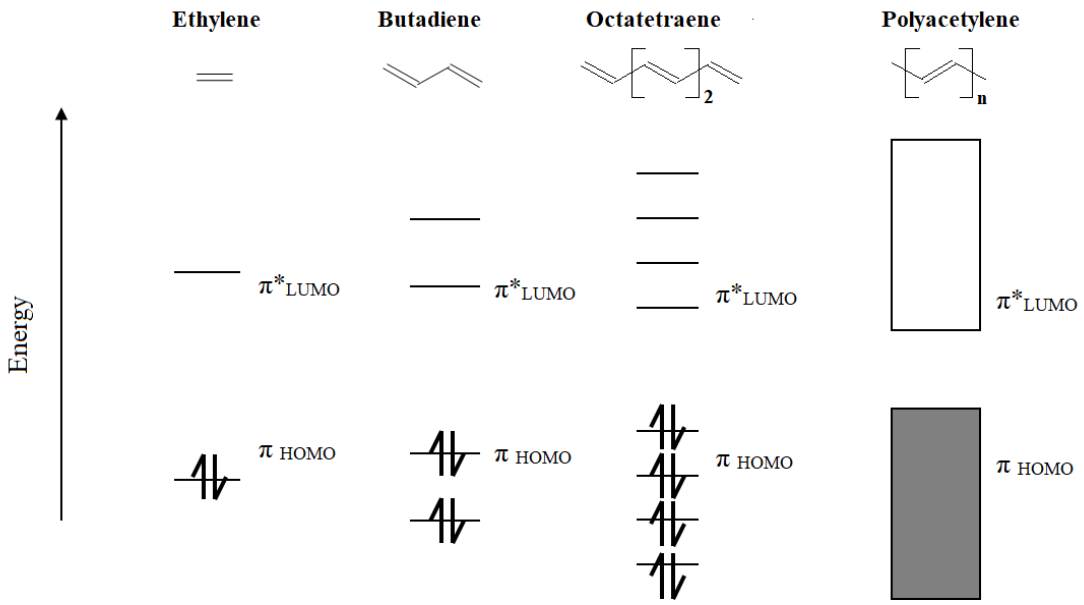

Figure 6 Polyacetylene π-orbitals

Aromatic polymers hold a similar convergence in the HOMO-LUMO gap from oligomers to polymer with the final band gaps spreading between 2.0 eV to 1.5 eV opposing to the dimers with band gaps around 5.0 eV.[84]

With a proper doping, the conductivity of these polymers can reach 10^5 S/cm, which is essentially a conductor, like a metal.[85-86] The electrochemical doping employs a metal electrode and small counterion to provide extra charge carriers as well as maintaining the electro-neutrality. The chemical doping method depends on the redox reactions. Often in vapour or solution phase, the dopant oxidises the polymer and leaves the counterion imbedded in the structure in one step. [83]

Polymer as a material can be processed in all sorts of ways in order to support their functions in the devices. In the area of energy conversion and storage, conductive polymers and their composites are seen for several applications with entirely different manufacturing approaches.

With porous nanosheet structure achieved during polymerisation, followed by a stacking process forming multi-layer thin film, PPy is used as supercapacitor electrode. The porous structure ensures the high charge/discharge efficiency as it provides easy access for mobile protons.[87]

The in-situ polymerisation of PANI is utilized to form a coating for silicon nanoparticles in the construction of lithium-ion battery anode. The solution based synthesis provides an evenly dispersed coating mechanism as well as potential scalability for mass production. A further 3D framework is formed to maintain a good conductivity between particles.[88]

A wet-spin method assisted by a hot-drawing process is used to manufacture PEDOT/PSS fibres in the application of electroactive materials. The flexibility of the fibre makes it suitable for wearable heaters as the fibre could also stand very high-amp current. A electromechanical response discovered makes the material a candidate for electromechanical actuators as well.[18]

1.5. Graphene

Graphene is one of those materials getting attention in all sorts of fields. The single layer carbon sheet is conjugated by atoms bonded in a hexagonal lattice, just like graphite. However as a nanomaterial, it obtains a variety of special properties, such as high Young's modulus (1 TPa), high charge carrier mobility (15000 $cm^2 \cdot V^{-1} \cdot s^{-1}$),[89] high surface area (2630 m^2/g) and high fracture strength (130 GPa) etc.[90] These excellent mechanical and electrical properties make the material as a promising candidate for energy-storage, specimen carrier, polymer composites and thermoelectric materials. Its

thermal conductivity (~5000 $W \cdot m^{-1} \cdot K^{-1}$)[91] is also higher than most traditional materials, which is not ideal for a thermoelectric material but might be attractive in other applications.

There are several methods of synthesizing graphene. In the early state of exploring the material, micromechanical exfoliation was used to produce small amount but high purity samples so that the fundamental study could be carried on.[92] With the help of atomic force microscope, the product can reach the size of several microns. This also inspired the method to demonstrate the making of graphene by using scotch tape. The peel-off method was not able to produce large-area films, which was succeeded using CVD technique.[93]

With clean metal substrate and gas protection during growth, CVD method shows the promise in the manufacture of high-quality monolayer graphene, especially for large scale applications.

Besides large-scale growth route, a large-scale exfoliation method is also discovered using a liquid-phase process in organic solvents.[94]

Non-chemical exfoliation is not the first solution method of manufacturing graphene. Chemical reduction method is another common method by reducing exfoliated graphite oxide. It is promising in the production of large amount of material with low cost.[95] The intense/harsh chemical reaction gives oxygen impurities and defects, and that is why this product is also referred as reduced graphene oxide (rGO), distinguishing from large-scale oxygen-free graphene.

During the development of organic thermoelectric materials, graphene's exceptionally high electrical conductivity along with its transparency are a good fit. In the meantime, there is the obstacle of it possessing equally high thermal conductivity.[96] The gapless

band structure also leads to a low Seebeck coefficient, which is a bad condition for achieving high figure of merit .The solution will be opening a band gap large enough for only one type of charge carrier moving around in the material.[97] Inducing disorder in the uniformed structure of graphene using plasma is one of the solutions.[98] However electrical conductivity will be decreased due to the disorder. This process is suitable for few-layer graphene, but will do some serious damage on rGO because of its pre-existing low conductivity.

When discussing thermal conductivity of graphene, things could be complicated. The value differs among studies, mainly due to different defects and substrates.[99] The theoretical value is difficult to reach even with a large-scale, single-layer sample. Phonon-electron scattering is the dominant one in the theoretical large graphene film; but in practice, thermal conductivity is largely affected by phonon scattering in the substrate, boundaries and edge roughness.[100]

The thermal property is also highly anisotropic. Thermal conductivity in in-plane direction is hundred times better than the one at cross plane direction, which is limited by the interface with adjacent material. This fact leads to graphene performing as a grain boundary.[101]

When combining with inorganic materials for thermoelectric applications, one of two situations in favour of better TE performance could occur. Firstly, an enhancement in electrical conductivity is achieved due to the high intrinsic charge carrier density in graphene. The other one could come as a surprise, but a reduction in thermal conductivity could be managed as well with the addition of graphene into the material.

Skutterudite is one of the most promising thermoelectric materials.[102] By introducing graphene into the engineering of grain boundaries in the crystalline material, the anisotropy serves the cause well by reducing thermal conductivity.

In the case of p-type $Bi_{0.5}Sb_{1.5}Te_3$, graphene comes with two gains. The boost in carrier concentration increases the electrical conductivity; and the additional phase boundaries help with the phonon scattering, decreasing the thermal conductivity.[103]

The production of PbTe/Graphene composites results in an electrical enhancement as well. Meanwhile, a reduction of PbTe size in the process causes more interfaces between crystallites and lowers the thermal conductivity.[104]

In the field of organic thermoelectric material development, graphene serves the purpose differently. PANI is a conductive polymer with potential in TE applications. A solution dispersion method was used with the help of graphene to synthesize the polymer. PANI uses graphene as a template and gains a better formation during the polymerisation.[105] In this process, graphene with fewer defects is required to achieve the best results.

PANI/Graphene would perform better with a further doping by p-Toluenesulfonic acid (pTSA).[106] Due to the π-π interaction, this material would have a high mobility of charge carriers.

Another case taking advantage of the π-π interaction took place using PEDOT.[107] The in-situ polymerisation uses the graphene as a template, resulting in a hybrid structure with increased power factor. Graphene could also act as an electrical bridge to increase electrical conductivity in other scenarios.[45]

1.6. Muon spin spectroscopy

A muon is a lepton with a charge of -1e and a spin of ½. It is similar to an electron but with 207 times of its mass and a mean lifetime of 2.197 μs. It could be found in cosmic rays but for research purpose a concentrated beam is required, generated from a synchrotron. Just like any other elementary particles, muon has an antiparticle with equal spin and mass but a positive charge called positive muon, or antimuon. In synchrotron facilities, positive muons are generated by hitting a graphite target with proton beam. Pion will be produced after proton being impinged on the target. With a mean lifetime of 26 ns, pion will decay and emit muon. When pion decays near the surface of the target, the surface muon would have 100% polarisation so that the experiments are performed non-resonantly even in the ALC-μSR.[108] Meanwhile, high-energy muon beam would have a polarisation below 80%, in which the pions escaping the target at high energies. When implanted into the sample, positive muon would behave like a proton with only ninth of its mass. With a short lifetime, muon would finally decay into positron (or electron depending on the charge) and two neutrinos. During this period of time, positive muon could capture an electron to form a muonium, a light isotope of proton, and then be added onto an unsaturated bond to form a muoniated radical. Unlike neutron experiments, which relies on scattering, muon spectroscopy detects the positron produced. Using forward and backward detectors, the asymmetry of muon polarisation could be monitored indirectly.

1.6.1. Avoided level crossing muon spin resonance

Avoided Level Crossing Muon Spin Resonance (ALC-μSR) is one type of Longitudinal Field Muon Spin relaxation (LF-μSR) as it is conducted in an external field along the axis of muon spin. It monitors the integration of polarization instead of time dependence.

ALC-μSR is known to study the dynamic and local environment of the muoniated radicals. In a high magnetic field, the eigenstates of radicals are considered as pure Zeeman states. However, when the field applied reaches a specific value, the mixing between states with muon, electron or nucleus spins causes a loss in time-integrated asymmetry and gives a sharp peak when polarization is plotted against external magnetic field. The level crossing resonances are measured by quantifying the forward backward asymmetry of the muon spin in an applied field. This would provide information on the local hyperfine fields felt by the muon.[109] The technique is best explained using a simple energy diagram of a muon interacting with an electron,[110] called a Breit-Rabi diagram, illustrated in Figure 7.

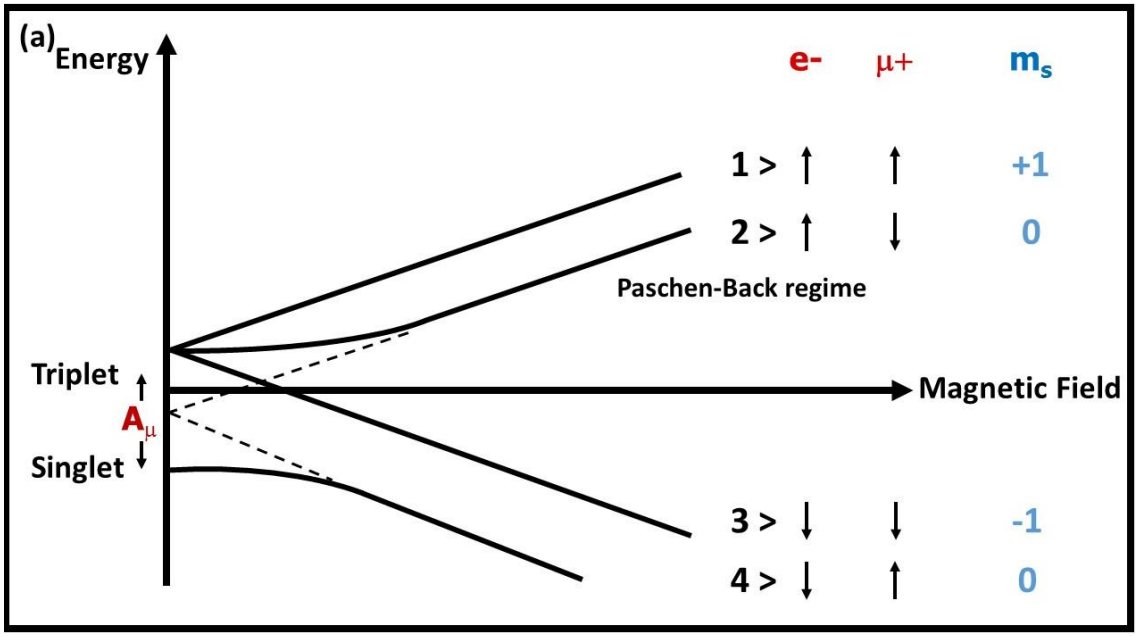

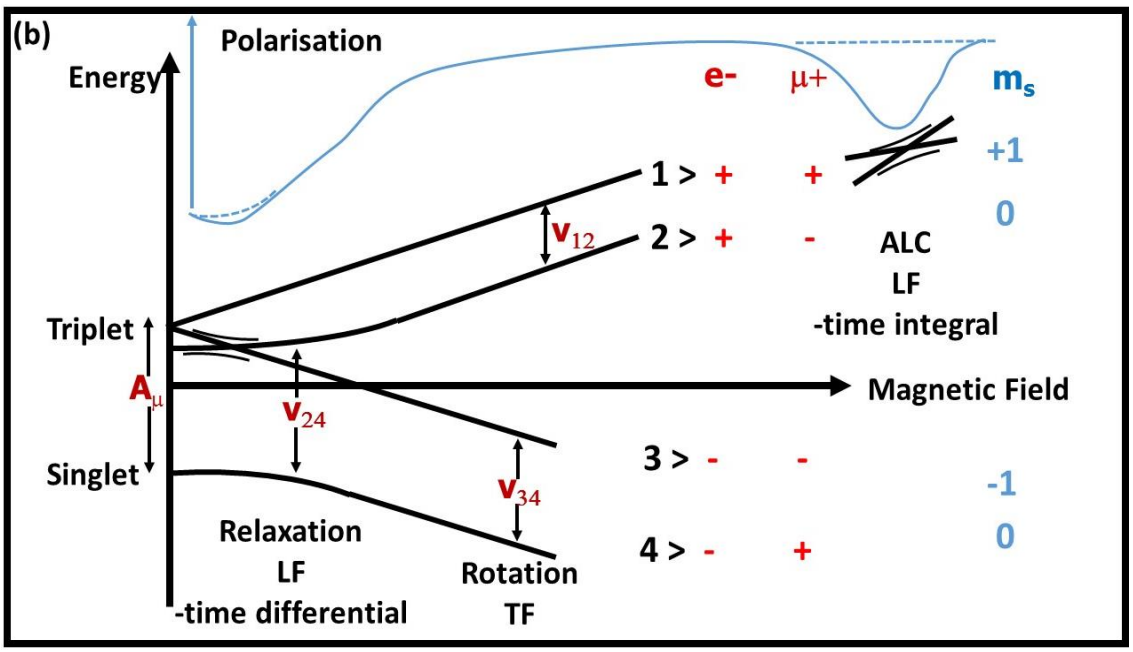

Figure 7 The Breit-Rabi diagram

At low applied fields there is mixing of some of the states as shown by their curving in the above diagram, but at higher fields well above that corresponding to the hyperfine field, the mixing disappears as shown by straight line parts of the states which are now pure Zeeman states of the system. At high enough fields the states cross each other, but for example if the hyperfine interaction is anisotropic one would find these states mix with each other and thus appear to avoid each other instead of crossing. This is the so called avoided level crossing, and the mixing of the states thus causes a loss in the muon polarisation, which is measured by scanning polarisation against applied field. The field at which this happens is given by the hyperfine interactions in the muoniated system. In muonium there are only two spins involved, that of the muon and the electron. However, in a molecule where there are other atoms with nuclear spin such as hydrogen, these spins too should be mixed into the above diagram, and thus resulting in more level crossings.

Based on the difference in total magnetic quantum number, ALC transaction is sorted into three different types ($\Delta M=0, 1, 2$). When $\Delta M=0$, $\Delta 0$ in short, two states have the

same electron spin but the opposite muon and proton spins. It's also called a muon-nucleus spin flip-flop. The peak position is given by the formula:[111]

$$B^{\Delta_0} = \frac{1}{2}\left|\frac{A_\mu - A_X}{2(\gamma_\mu - \gamma_X)} - \frac{A_\mu + A_X}{2\gamma_e}\right| \quad (1.9)$$

Where as in Δ1, the only difference is the muon spin. The value of the external magnetic field is determined by:[111]

$$B^{\Delta_1} = \frac{1}{2}\left|\frac{A_\mu}{\gamma_\mu} - \frac{A_\mu}{\gamma_e}\right| \quad (1.10)$$

where A is the hyperfine coupling constant and γ is the gyromagnetic ratio.

Since the peak position is related to the hyperfine coupling of muon and proton in the radicals, the variation of hyperfine coupling constant can be used to determine the position of the muonium as well as the dynamics.[112] The computer simulation is a good way of predicting the polarization of muon spin as well as the interaction between muons, electrons and nuclei.

1.6.2. Transverse field muon spin rotation

Muon spin rotation is conducted with an external magnetic field applied transverse to the muon beam direction and the muon would rotate under the influence. With muon being implanted into the sample, capturing an electron to form a muonium and then being added to an unsaturated bond before decay, two precession frequencies are expected in the Fourier transform of muon time spectra when a radical is formed relating to one available muon site. Frequencies are given by the formula:

$$\omega = \left|\gamma_\mu B \pm A/2\right| \quad (1.11)$$

where ω is the frequency, B is external magnetic field and A is hyperfine coupling constant.[113]

The corresponding correlation peak would be discovered as this pair of peaks in Fourier transform spectrum is related to this given value of hyperfine coupling constant A_{μ}.[114]

1.7. Summary and Thesis Overview

With the mind on developing silicon nanoparticles in the application of thermoelectric, my doctoral research has been focusing on the synthesis and modification of the material in order to achieve better performance. With most thermoelectric properties measured elsewhere, minor alterations of the material are done based on the preliminary analysis of the material mainly in the subject of conductivities. The research started with the manufacture of silicon quantum dots with diameter of 5 nanometres. The first approach is called a top-down method, which utilizing a chemical-electrical procedure upon the silicon wafer as raw material. The production of nanoparticle and surface modification are in two steps. With the base of crystalline wafer, unified products are gathered. Downside of this method is the yield as only milligrams are obtained with one reaction. Synthesis are soon redirected into another method known as bottom-up. Using a solution reduction approach, silicon nanoparticles are grown from atoms. Mass production is essential for thermoelectric research as the manufacture of material is not the whole journey. Enough products are obtained with the solution synthesis. The main mission in developing a silicon based thermoelectric material is to improve the electrical conductivity and that is the guideline being following. The organic ligand used for surface modification started with phenylacetylene, a polyacetylene-based polymer with side groups. The overlapping of ligands improved the interaction between nanoparticles, with proof in micro-conductivity research using muon spin spectroscopy. The second step is terthiophene as the oligomer has a longer reach from the surface. When a further development is in order, the pre-oligomerisation is not an option as terthiophene already

shows problem relating to surface coverage. Higher coverage and longer chain are obtained with the capping of thiophene and polymerisation afterwards. Another step has been added into the synthesis of nanoparticles after the ligand attachment. Already gathering much attention, producing a graphene composite became a further step for increasing electrical conductivity. With the assistance of in-situ polymerisation and spark plasma sintering technique, graphene is firmed combined with silicon nanoparticles and better conductivity is achieved along with the option of high temperature application.

In this thesis, a detailed account of my research is presented. Chapter 1 is the background and literature review of my field of research, including the introduction of not only TE, nanotechnology and conductive polymer but also graphene and muon as specially part of my work.

In Chapter 2, methodology and results will be introduced and explained. Chapter 3 focuses on the production of thiophene and terthiophene capped silicon nanoparticles. This is the early stage of this research and conductive polymers especially with TE applications are looked into. Chapter 4 introduces graphene as part of the improvement of the polythiophene functionalized silicon nanoparticles. Detailed analysis is conducted on both self-made graphene and final products. Chapter 5 is on a side track exploring the possible application of muon spin spectroscopy in micro-conductivity research. With conductive ligand capped silicon nanoparticle as research subject, the work expands the scope of μSR as a mean of research.

Reference

1. C. B. Vining, *Nature materials* 8, 83 (2009).

2. R. Viswanathan, K. Coleman, and U. Rao, *International Journal of Pressure Vessels and Piping* 83, 778 (2006).

3. J. Bugge, S. Kjær, and R. Blum, *Energy* 31, 1437 (2006).

4. A. Martínez, D. Astrain, and A. Rodríguez, *Energy* 55, 1114 (2013).

5. W.-H. Chen, C.-C. Wang, C.-I. Hung, C.-C. Yang, and R.-C. Juang, *Energy* 64, 287 (2014).

6. S. J. Kim, J. H. We, and B. J. Cho, *Energy & Environmental Science* 7, 1959 (2014).

7. G. L. Bennett, J. J. Lombardo, R. J. Hemler, G. Silverman, C. W. Whitmore, W. R. Amos, E. W. Johnson, R. W. Zocher, J. C. Hagan, and R. W. Englehart, *AIP Conference Proceedings* 969, 663 (2008).

8. Z. U. Khan, J. Edberg, M. M. Hamedi, R. Gabrielsson, H. Granberg, L. Wågberg, I. Engquist, M. Berggren, and X. Crispin, *Advanced Materials* 28, 4556 (2016).

9. K. Gaurav, and S. K. Pandey, (2016).

10. B. Sherman, R. R. Heikes, and R. W. Ure, *Journal of Applied Physics* 31, 1 (1960).

11. O. Bubnova, Z. U. Khan, A. Malti, S. Braun, M. Fahlman, M. Berggren, and X. Crispin, *Nat Mater* 10, 429 (2011).

12. J. K. Bohrer, K. Schröer, L. Brendel, and D. E. Wolf, *arXiv preprint arXiv:1701.07303*, (2017).

13. G. Schierning, *physica status solidi (a)* 211, 1235 (2014).

14. G. J. Snyder, and E. S. Toberer, *Nature materials* 7, 105 (2008).

15. Y. Zhang, M. Cleary, X. Wang, N. Kempf, L. Schoensee, J. Yang, G. Joshi, and L. Meda, *Energy Conversion and Management* 105, 946 (2015).

16. M. Tewolde, G. Fu, D. J. Hwang, L. Zuo, S. Sampath, and J. P. Longtin, *Journal of Thermal Spray Technology* 25, 431 (2015).

17. P. D. Mitcheson In *Energy harvesting for human wearable and implantable bio-sensors*, 2010/08//; IEEE: pp 3432.

18. J. Zhou, M. Mulle, Y. Zhang, X. Xu, E. Q. Li, F. Han, S. T. Thoroddsen, and G. Lubineau, *J. Mater. Chem. C* 4, 1238 (2016).

19. A. R. M. Siddique, R. Rabari, S. Mahmud, and B. V. Heyst, *Energy* 115, 1081 (2016).

20. Y. Ma, Q. Hao, B. Poudel, Y. Lan, B. Yu, D. Wang, G. Chen, and Z. Ren, *Nano Letters* 8, 2580 (2008).

21. D. A. Wright, *Nature* 181, 834 (1958).

22. H. Alam, and S. Ramakrishna, *Nano Energy* 2, 190 (2013).

23. R. Venkatasubramanian, E. Siivola, T. Colpitts, and B. O'Quinn, *Nature* 413, 597 (2001).

24. Y. Takagiwa, Y. Pei, G. Pomrehn, and G. J. Snyder, *Appl Phys Lett* 101, 092102 (2012).

25. Y. Takagiwa, Y. Pei, G. Pomrehn, and G. Jeffrey Snyder, *APL Materials* 1, 011101 (2013).

26. T. C. Harman, P. J. Taylor, M. P. Walsh, and B. E. LaForge, *Science* 297, (2002).

27. X. W. Wang, H. Lee, Y. C. Lan, G. H. Zhu, G. Joshi, D. Z. Wang, J. Yang, A. J. Muto, M. Y. Tang, J. Klatsky, S. Song, M. S. Dresselhaus, G. Chen, and Z. F. Ren, *Appl Phys Lett* 93, 19 (2008).

28. G. Joshi, H. Lee, Y. Lan, X. Wang, G. Zhu, D. Wang, R. W. Gould, D. C. Cuff, M. Y. Tang, M. S. Dresselhaus, G. Chen, and Z. Ren, *Nano Letters* 8, 4670 (2008).

29. A. Samarelli, L. Ferre Llin, S. Cecchi, J. Frigerio, D. Chrastina, G. Isella, E. Müller Gubler, T. Etzelstorfer, J. Stangl, Y. Zhang, J. M. R. Weaver, P. S. Dobson, and D. J. Paul, *Solid-State Electronics* 98, 70 (2014).

30. J. R. Salvador, J. Y. Cho, Z. Ye, J. E. Moczygemba, A. J. Thompson, J. W. Sharp, J. D. König, R. Maloney, T. Thompson, J. Sakamoto, H. Wang, A. A. Wereszczak, and G. P. Meisner, *Journal of Electronic Materials* 42, 1389 (2012).

31. J. Q. Guo, H. Y. Geng, T. Ochi, S. Suzuki, M. Kikuchi, Y. Yamaguchi, and S. Ito, *Journal of Electronic Materials* 41, 1036 (2012).

32. J. R. Salvador, J. Y. Cho, Z. Ye, J. E. Moczygemba, A. J. Thompson, J. W. Sharp, J. D. Koenig, R. Maloney, T. Thompson, J. Sakamoto, H. Wang, and A. A. Wereszczak, *Phys Chem Chem Phys* 16, 12510 (2014).

33. C. Yu, Y. Chen, H. Xie, G. J. Snyder, C. Fu, J. Xu, X. Zhao, and T. Zhu, *Applied Physics Express* 5, 031801 (2012).

34. S. R. Brown, S. M. Kauzlarich, F. Gascoin, and G. J. Snyder, *ChemInform* 37, 1873 (2006).

35. M. Culebras, C. Gómez, and A. Cantarero, *Materials* 7, 6701 (2014).

36. M. Culebras, C. M. Gómez, and A. Cantarero, *Journal of Materials Chemistry A* 2, 10109 (2014).

37. S. H. Lee, H. Park, S. Kim, W. Son, I. W. Cheong, and J. H. Kim, *Journal of Materials Chemistry A* 2, 7288 (2014).

38. T. Park, C. Park, B. Kim, H. Shin, and E. Kim, *Energy & Environmental Science* 6, 788 (2013).

39. B. Senthilkumar, P. Thenamirtham, and R. Kalai Selvan, *Applied Surface Science* 257, 9063 (2011).

40. C. Yi, A. Wilhite, L. Zhang, R. Hu, S. S. Chuang, J. Zheng, and X. Gong, *ACS Appl Mater Interfaces* 7, 8984 (2015).

41. Y. Liu, N. Nishiwaki, K. Saigo, and R. Sugimoto, *Bulletin of the Chemical Society of Japan* 86, 1076 (2013).

42. L. Wang, X. Jia, D. Wang, G. Zhu, and J. Li, *Synthetic Metals* 181, 79 (2013).

43. D. Wang, Y. Su, D. Chen, L. Wang, X. Xiang, and D. Zhu, *Composites Part B: Engineering* 69, 467 (2015).

44. J. Li, C. Lai, X. Jia, L. Wang, X. Xiang, C.-L. Ho, H. Li, and W.-Y. Wong, *Composites Part B: Engineering* 77, 248 (2015).

45. D. Yoo, J. Kim, S. H. Lee, W. Cho, H. H. Choi, F. S. Kim, and J. H. Kim, *J. Mater. Chem. A* 3, 6526 (2015).

46. N. Neophytou, X. Zianni, H. Kosina, S. Frabboni, B. Lorenzi, and D. Narducci, *Nanotechnology* 24, 205402 (2013).

47. N. F. Hinsche, I. Mertig, and P. Zahn, *J Phys Condens Matter* 24, 275501 (2012).

48. B. Touami, and D. V. Osborne, *Journal of Physics C: Solid State Physics* 15, 6719 (1982).

49. M. Asheghi, K. Kurabayashi, R. Kasnavi, and K. Goodson, *Journal of applied physics* 91, 5079 (2002).

50. K. T. Regner, D. P. Sellan, Z. Su, C. H. Amon, A. J. McGaughey, and J. A. Malen, *Nature communications* 4, 1640 (2013).

51. A. J. Minnich, J. A. Johnson, A. J. Schmidt, K. Esfarjani, M. S. Dresselhaus, K. A. Nelson, and G. Chen, *Physical Review Letters* 107, 095901 (2011).

52. T. Claudio, N. Stein, D. G. Stroppa, B. Klobes, M. M. Koza, P. Kudejova, N. Petermann, H. Wiggers, G. Schierning, and R. P. Hermann, *Phys Chem Chem Phys* 16, 25701 (2014).

53. G. Schierning, J. Stoetzel, R. Chavez, V. Kessler, J. Hall, R. Schmechel, T. Schneider, N. Petermann, H. Wiggers, S. Angst, D. E. Wolf, B. Stoib, A. Greppmair, M. Stutzmann, and M. S. Brandt, *physica status solidi (a)* 213, 497 (2016).

54. S. Bathula, B. Gahtori, M. Jayasimhadri, S. K. Tripathy, K. Tyagi, A. K. Srivastava, and A. Dhar, *Appl Phys Lett* 105, 061902 (2014).

55. A. Miura, S. Zhou, T. Nozaki, and J. Shiomi, *ACS Appl Mater Interfaces* 7, 13484 (2015).

56. Y. Nakamura, M. Isogawa, T. Ueda, S. Yamasaka, H. Matsui, J. Kikkawa, S. Ikeuchi, T. Oyake, T. Hori, J. Shiomi, and A. Sakai, *Nano Energy* 12, 845 (2015).

57. A. I. Hochbaum, R. Chen, R. D. Delgado, W. Liang, E. C. Garnett, M. Najarian, A. Majumdar, and P. Yang, *Nature* 451, 163 (2008).

58. D. Li, Y. Wu, P. Kim, L. Shi, P. Yang, and A. Majumdar, *Applied Physics Letters* 83, 2934 (2003).

59. A. Kikuchi, A. Yao, I. Mori, I. Yamashita, T. Ono, and S. Samukawa In *Thermal conductivity of 10 nm-diameter silicon nanowires array fabricated by bio-template and neutral beam etching*, Nanotechnology (IEEE-NANO), 2016 IEEE 16th International Conference on, IEEE: 2016; pp 505.

60. T. Zhang, S. Wu, J. Xu, R. Zheng, and G. Cheng, *Nano Energy* 13, 433 (2015).

61. C. Mangold, S. Neogi, and D. Donadio, *Appl Phys Lett* 109, 053902 (2016).

62. J. A. Taborda, J. J. Romero, B. Abad, M. Munoz-Rojo, A. Mello, F. Briones, and M. S. Gonzalez, *Nanotechnology* 27, 175401 (2016).

63. E. Roduner, *Chemical Society Reviews* 35, 583 (2006).

64. M. Reibold, P. Paufler, A. A. Levin, W. Kochmann, N. Patzke, and D. C. Meyer, *Nature* 444, 286 (2006).

65. S. Padovani, C. Sada, P. Mazzoldi, B. Brunetti, I. Borgia, A. Sgamellotti, A. Giulivi, F. d'Acapito, and G. Battaglin, *Journal of Applied Physics* 93, 10058 (2003).

66. G. Frens, *Nature* 241, 20 (1973).

67. T. K. Sau, and C. J. Murphy, *J Am Chem Soc* 126, 8648 (2004).

68. M. Brust, M. Walker, D. Bethell, D. J. Schiffrin, and R. Whyman, *Journal of the Chemical Society, Chemical Communications*, 801 (1994).

69. G. Ajnai, A. Chiu, T. Kan, C.-C. Cheng, T.-H. Tsai, and J. Chang, *Journal of Experimental & Clinical Medicine* 6, 172 (2014).

70. A. B. Chinen, C. M. Guan, J. R. Ferrer, S. N. Barnaby, T. J. Merkel, and C. A. Mirkin, *Chem Rev* 115, 10530 (2015).

71. F. K. Alanazi, A. A. Radwan, and I. A. Alsarra, *Saudi Pharm J* 18, 179 (2010).

72. H. Dai, *Accounts of Chemical Research* 35, 1035 (2002).

73. J. R. Sanchez-Valencia, T. Dienel, O. Groning, I. Shorubalko, A. Mueller, M. Jansen, K. Amsharov, P. Ruffieux, and R. Fasel, *Nature* 512, 61 (2014).

74. N. Arora, and N. N. Sharma, *Diamond and Related Materials* 50, 135 (2014).

75. P. A. Danilov, A. A. Ionin, S. I. Kudryashov, S. V. Makarov, N. N. Mel'nik, A. A. Rudenko, V. I. Yurovskikh, D. V. Zayarny, V. N. Lednev, E. D. Obraztsova, S. M. Pershin, and A. F. Bunkin, *Laser Physics Letters* 11, 106101 (2014).

76. A. Eatemadi, H. Daraee, H. Karimkhanloo, M. Kouhi, N. Zarghami, A. Akbarzadeh, M. Abasi, Y. Hanifehpour, and S. W. Joo, *Nanoscale Research Letters* 9, 393 (2014).

77. M. F. L. S. H. T. R. H. B. a. De Volder, A. J. Hart, M. F. L. De Volder, S. H. Tawfick, R. H. Baughman, and A. J. Hart, *Science* 339, 535 (2013).

78. N. Behabtu, C. C. Young, D. E. Tsentalovich, O. Kleinerman, X. Wang, A. W. K. Ma, E. A. Bengio, R. F. ter Waarbeek, J. J. de Jong, R. E. Hoogerwerf, S. B. Fairchild, J. B. Ferguson, B. Maruyama, J. Kono, Y. Talmon, Y. Cohen, M. J. Otto, and M. Pasquali, *Science* 339, 182 (2013).

79. H. Lin, L. Li, J. Ren, Z. Cai, L. Qiu, Z. Yang, and H. Peng, *Sci Rep* 3, 1353 (2013).

80. G. Zhong, H. Wang, H. Yu, and F. Peng, *Journal of Power Sources* 286, 495 (2015).

81. X. Zheng, J. Deng, N. Wang, D. Deng, W. H. Zhang, X. Bao, and C. Li, *Angew Chem Int Ed Engl* 53, 7023 (2014).

82. Y. Shi, and G. Yu, *Chemistry of Materials* 28, 2466 (2016).

83. O. Bubnova, and X. Crispin, *Energy & Environmental Science* 5, 9345 (2012).

84. S. S. Zade, and M. Bendikov, *Organic Letters* 8, 5243 (2006).

85. A. G. MacDiarmid, *Angewandte Chemie - International Edition* 40, 2581 (2001).

86. B. J. Worfolk, S. C. Andrews, S. Park, J. Reinspach, N. Liu, M. F. Toney, S. C. B. Mannsfeld, and Z. Bao, *Proceedings of the National Academy of Sciences* 112, 14138 (2015).

87. D. P. Dubal, S. H. Lee, J. G. Kim, W. B. Kim, and C. D. Lokhande, *Journal of Materials Chemistry* 22, 3044 (2012).

88. H. Wu, G. Yu, L. Pan, N. Liu, M. T. McDowell, Z. Bao, and Y. Cui, *Nature communications* 4, 1943 (2013).

89. K. S. Novoselov, A. K. Geim, S. V. Morozov, D. Jiang, Y. Zhang, S. V. Dubonos, I. V. Grigorieva, and A. A. Firsov, *Science* 306, 666 (2004).

90. M. C. Wang, C. Yan, L. Ma, N. Hu, and M. W. Chen, *Computational Materials Science* 54, 236 (2012).

91. A. a. Balandin, S. Ghosh, W. Bao, I. Calizo, D. Teweldebrhan, F. Miao, and C. N. Lau, *Nano Lett.* 8, 902 (2008).

92. X. Lu, M. Yu, H. Huang, and R. S. Ruoff, *Nanotechnology* 10, 269 (1999).

93. K. S. Kim, Y. Zhao, H. Jang, S. Y. Lee, J. M. Kim, K. S. Kim, J. H. Ahn, P. Kim, J. Y. Choi, and B. H. Hong, *Nature* 457, 706 (2009).

94. Y. Hernandez, V. Nicolosi, M. Lotya, F. M. Blighe, Z. Sun, S. De, I. T. McGovern, B. Holland, M. Byrne, Y. K. Gun'Ko, J. J. Boland, P. Niraj, G. Duesberg, S. Krishnamurthy, R. Goodhue, J. Hutchison, V. Scardaci, A. C. Ferrari, and J. N. Coleman, *Nature nanotechnology* 3, 563 (2008).

95. S. Stankovich, D. A. Dikin, R. D. Piner, K. A. Kohlhaas, A. Kleinhammes, Y. Jia, Y. Wu, S. T. Nguyen, and R. S. Ruoff, *Carbon* 45, 1558 (2007).

96. Y. Xu, Z. Li, and W. Duan, *Small* 10, 2182 (2014).

97. M. C. Nguyen, V. H. Nguyen, H.-V. Nguyen, J. Saint-Martin, and P. Dollfus, *Physica E: Low-dimensional Systems and Nanostructures* 73, 207 (2015).

98. N. Xiao, X. Dong, L. Song, D. Liu, Y. Tay, S. Wu, L.-J. Li, Y. Zhao, T. Yu, H. Zhang, W. Huang, H. H. Hng, P. M. Ajayan, and Q. Yan, *Acs Nano* 5, 2749 (2011).

99. A. A. Balandin, S. Ghosh, W. Bao, I. Calizo, D. Teweldebrhan, F. Miao, and C. N. Lau, *Nano letters* 8, 902 (2008).

100. E. Pop, V. Varshney, and A. K. Roy, *MRS Bulletin* 37, 1273 (2012).

101. R. Lundgren, P. Laurell, and G. A. Fiete, *Physical Review B - Condensed Matter and Materials Physics* 90, 64 (2014).

102. P.-a. Zong, R. Hanus, M. Dylla, Y. Tang, J. Liao, Q. Zhang, G. J. Snyder, and L. Chen, *Energy Environ. Sci.* 10, 183 (2017).

103. D. Suh, S. Lee, H. Mun, S.-H. Park, K. H. Lee, S. Wng Kim, J.-Y. Choi, and S. Baik, *Nano Energy* 13, 67 (2015).

104. J. Dong, W. Liu, H. Li, X. Su, X. Tang, and C. Uher, *Journal of Materials Chemistry A* 1, 12503 (2013).

105. L. Wang, Q. Yao, H. Bi, F. Huang, Q. Wang, and L. Chen, *Journal of Materials Chemistry A* 2, 11107 (2014).

106. M. O. Ansari, M. M. Khan, S. A. Ansari, I. Amal, J. Lee, and M. H. Cho, *Chemical Engineering Journal* 242, 155 (2014).

107. K. Xu, G. Chen, and D. Qiu, *Journal of Materials Chemistry A* 1, 12395 (2013).

108. S. J. Blundell, *Chemical Reviews* 104, 5717 (2004).

109. C. J. Rhodes, *Annual Reports Section "C" (Physical Chemistry)* 97, 315 (2001).

110. U. A. Jayasooriya, and R. Grinter, In *Encyclopaedia of Applied Spectroscopy*, Andrews, D. L., Ed. Wiley-VCH: Weinheim, Germany, 2009; pp 153.

111. I. McKenzie, *Annual Reports Section "C" (Physical Chemistry)* 109, 65 (2013).

112. N. J. Clayden, *Phys. Scr.* 88, 068507 (2013).

113. S. J. Blundell, *Chem Rev* 104, 5717 (2004).

114. B. W. Lovett, S. J. Blundell, J. S. Stiessberger, F. L. Pratt, T. Jestaadt, W. Hayes, S. P. Cottrell, and I. D. Reid, *Physical Review B* 63, (2001).

Chapter 2. Materials and Experimental Methods

Silicon nanoparticles capped with organic ligands as well as the silane molecules are produced by using chemical reactions in solution. Materials are characterised by using elemental and structural analysis along with size measurements for the nanoparticle silicon core. Thermoelectric properties are measured afterwards with bulk pellets made of the ligands capped silicon nanoparticles, they are discovered separately to put together for assessing the performance.

Contents

2.1. Synthesis methods

2.1.1. Electrochemical etching method for nanoparticles synthesis

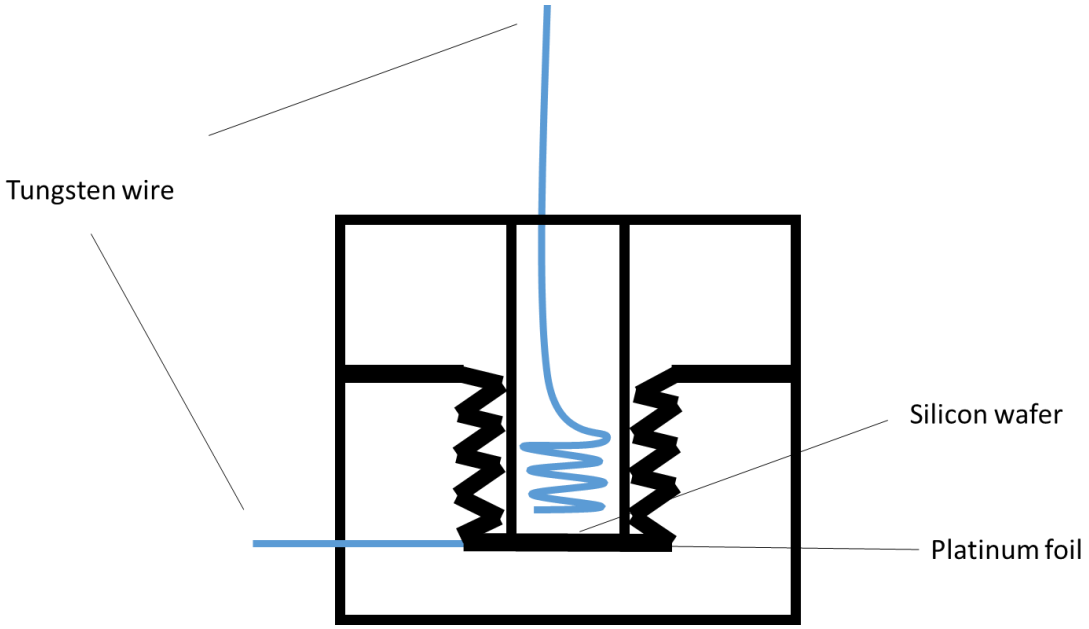

Figure 8 Electrochemical etching kit: a PTFE cell with tungsten as electrode

Silicon nanoparticles were synthesized by electrochemically etched using a mixture of aqueous HF solution and ethanol inside a custom-made PTFE cell. The electric current used was 300 mA and the etching time was 5 minutes.[1] Prior to the etching, the silicon wafer (111) was cut into square chips of 1.25 cm × 1.25 cm with a diamond cutter. Then these chips were dipped into the etching solution, in order to remove oxide from the surface. This solution is made by mixing 48% HF solution in water with ethanol to a ratio of 1:1. Afterwards, the silicon chip was placed inside the cell and on top of a platinum foil. The polished side of the chip was put upwards and exposed to the chemical etching solution. A rubber seal was used on top of the silicon chip to keep the solution in the upper part of the cell from leaking out. With the chip acting as anode, tungsten wire was chosen as cathode as it is resistant to HF. The power source used for the etching was a Keithley Source Meter 2601 which could maintain a constant current during the

experiment as well as stopping the process automatically. The resulting H-terminated silicon nanoparticles were dried under vacuum for at least 2 hrs to remove any residual hydrofluoric acid and then stored under nitrogen. Each chip yields 2.5 mg of product.

2.1.2. Sodium naphthalide reduction method

2.1.2.1. Synthesis of phenylacetylene capped SiNPs

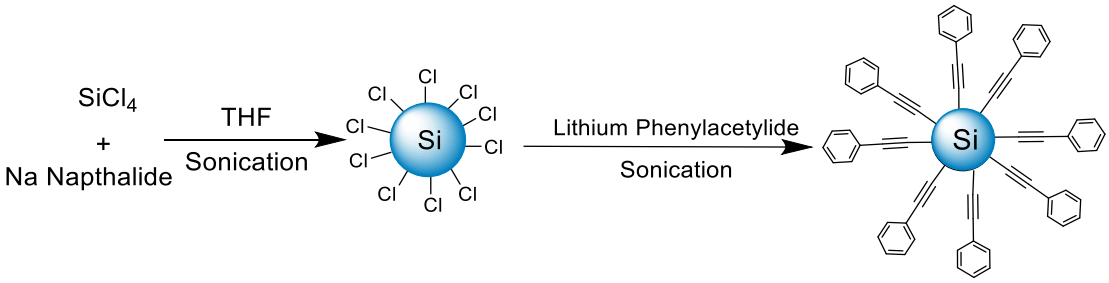

Scheme 1 Synthesis of phenylacetylene capped SiNPs

1 g of sodium and 4.2 g of naphthalene were added to a flask and flushed with nitrogen. 70 ml of dry THF was added to this and the mixture was ultra-sonicated for 2 hrs to give a dark green suspension. This was added to a flask with a stirring bar containing 1 ml of $SiCl_4$ dispersed in 200 ml of THF. The solution immediately turned into a brown suspension.[2-3]

To this suspension, phenylethynyl lithium solution was added 15 min later. This was prepared by reacting a solution of phenylacetylene (1.5 ml) in dry THF (20 ml) with 11.5 ml of n-BuLi (1.6 M in hexane), to give a cloudy suspension after 30 mins at RT. The mixture was refluxed for 12 hrs. After the reaction was completed, the mixture was quenched with ethanol and washed with water. The product was extracted with diethyl ether followed by separation. The solvent was removed and sample was heated under vacuum in an oil bath to get rid of naphthalene. The product was an orange crystalline powder and one batch yields 300 mg.

Characterization and thermoelectric application development of this material are done by Shane Ashby. [3]

2.1.2.2. Synthesis of thiophene capped SiNPs

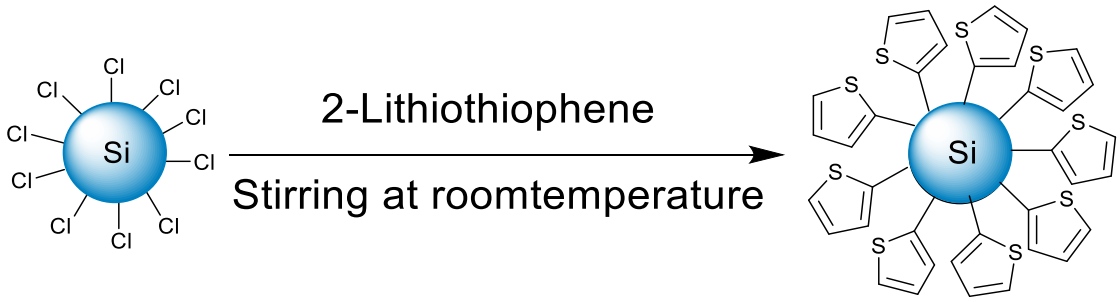

Scheme 2 Synthesis of thiophene capped SiNPs

1 g of sodium and 4.2 g of naphthalene were added to a flask and flushed with nitrogen. 70 ml of dry THF was added to this and the mixture was ultra-sonicated for 2 hrs to give a dark green suspension. This was added to a flask with a stirring bar containing 1 ml of $SiCl_4$ dispersed in 200 ml of THF under nitrogen.

The clear solution immediately turned into a brown suspension.[2-3]

To this suspension, thiophenyl lithium solution was added. This was prepared by reacting a solution of thiophene (1.5 ml) in dry THF (20 ml) with 11.5 ml of n-BuLi (1.6 M in hexane), to give a cloudy suspension after 30 mins at RT. The mixture was stirred at RT for 12 hrs. After the reaction was completed, the mixture was quenched with ethanol and washed with water. The product was extracted with diethyl ether followed by separation.

The solvent was removed and sample was heated under vacuum in an oil bath to get rid of naphthalene. The product was a dark brown wax and one batch yields 300 mg.

2.1.2.3. Synthesis of terthiophene capped SiNPs

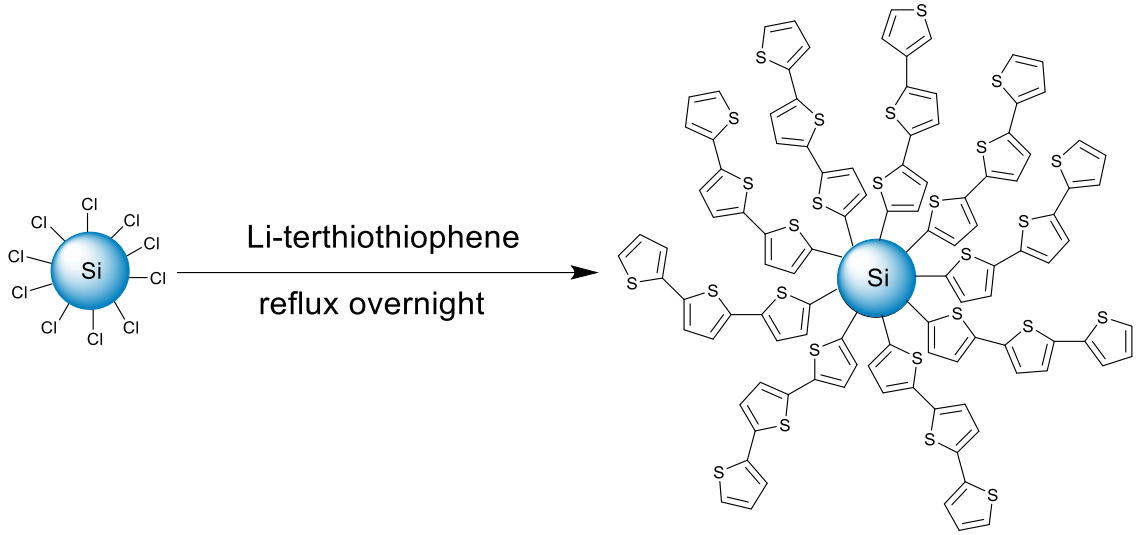

Scheme 3 Synthesis of terthiophene capped SiNPs

1 g of sodium and 4.2 g of naphthalene were added to a flask and flushed with nitrogen.

70 ml of dry THF was added to this and the mixture was ultra-sonicated for 2 hrs to give a dark green suspension.

This was added to a flask with a stirring bar containing 1 ml of $SiCl_4$ dispersed in 200 ml of THF. The solution immediately turned into a brown suspension.[2-3]

To this suspension, terthiophenyl lithium solution was added. This was prepared by reacting a solution of terthiophene in dry THF (20 ml) with 11.5 ml of n-BuLi (1.6 M in hexane), to give a cloudy suspension after 30 mins at RT. The mixture was heated at reflux for 12 hrs. The terthiophene was synthesized prior to this procedure.

After the reaction was completed, the mixture was quenched with ethanol and washed with water. The product was extracted with diethyl ether followed by separation. The solvent was removed and sample was heated under vacuum in an oil bath to get rid of naphthalene. The product was a dark yellow crystalline solid and one batch yields 400 mg.

2.1.2.4. Synthesis of polythiophene capped SiNPs

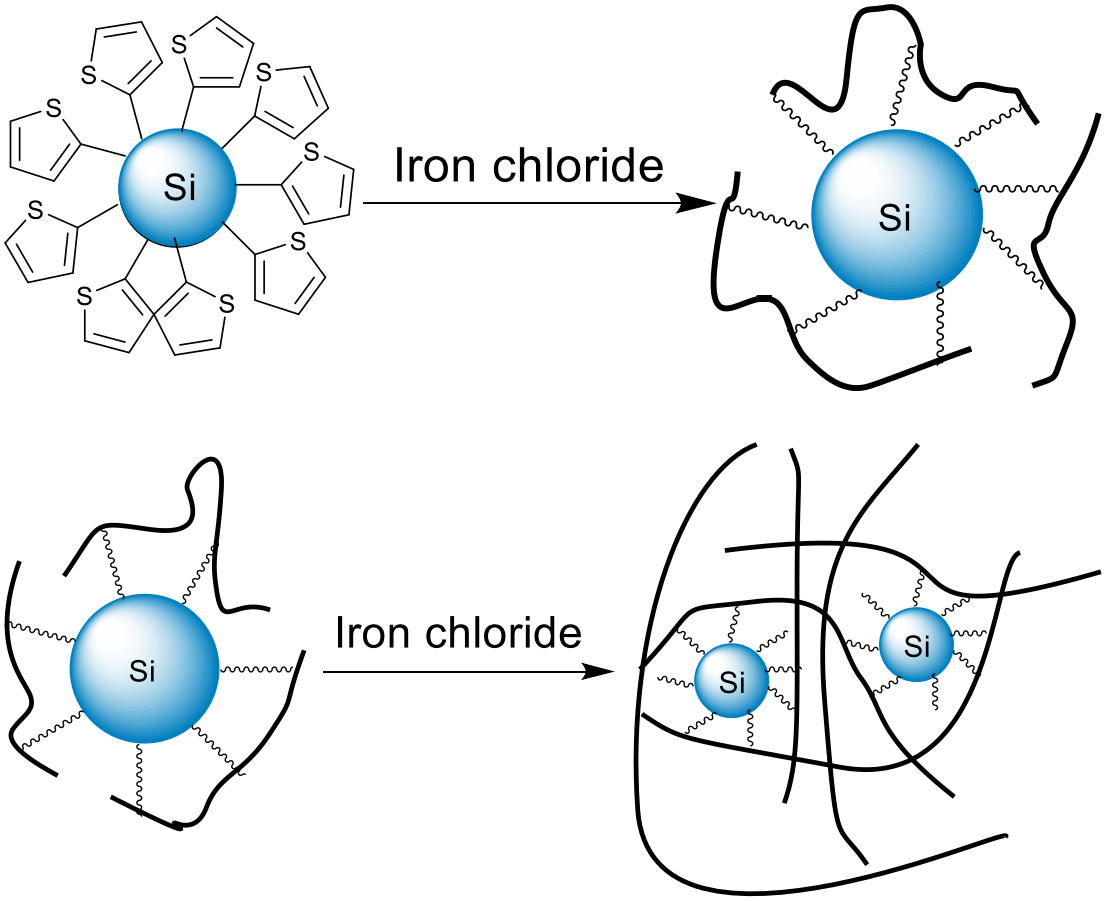

Scheme 4 Synthesis of polymer capped SiNPs

Thiophene capped SiNPs (0.15 g) were dissolved in a mixture of 15 ml of dry chloroform and 1 mL of thiophene monomer.

4.8 g $FeCl_3$ was dispersed in 35 ml of dry chloroform in ultrasonic bath.

$FeCl_3$ dispersion was added dropwise into previous solution while stirring.[4]

Mixture was stirred for 5 hrs before put into fridge overnight.

100 ml of methanol was added into the chilled mixture, causing precipitation.

After filtration, dark red solid was obtained.

2.1.2.5. Doping of polymer capped SiNPs

Polymer capped SiNPs (0.2 g) was added into a round bottom flask with a stirring bar.

Certain amount of $NOBF_4$ was mixed with SiNPs.[4]

Flask was attached to Schlenk line and flushed with nitrogen.

Under the inert gas atmosphere, 5 ml of dehydrate chloroform was introduced.

Mixture was stirred overnight at RT.

Solvent was evaporated and product was obtained.

The product appeared to be black powder.

2.1.3. Synthesis of tetrakis (2-phenylethynyl) silane

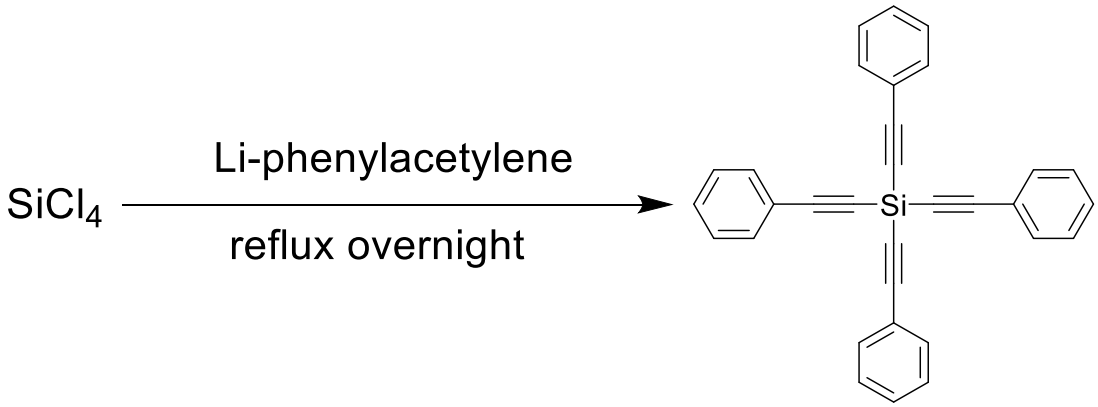

Scheme 5 Synthesis of tetrakis (2-phenylethynyl)silane as model molecule[5]

The model molecule used in muon experiments were synthesized using a THF solution based method.

1ml of $SiCl_4$ was dispersed in 200 ml of THF.

To this, phenylacetylene lithium solution was added. [It was prepared by reacting a solution of phenylacetylene (3.8 ml) in dry THF (20 ml) with 22 ml of n-BuLi (1.6 M in hexane), to give a cloudy suspension after 30 mins at RT]

The mixture was refluxed for 4 hrs.

After the reaction was completed, the mixture was dried and recrystallized in chloroform. A final product of white needle-like crystal was obtained.

2.1.4. Synthesis of 2,2':5',2"-terthiophene

Terthiophene was synthesized following method published by Smeets et al.[6] using Grignard reagent with dichloro(diphenylphosphinopropyl)nickel ($NiCl_2$[dppp]) as catalyst.

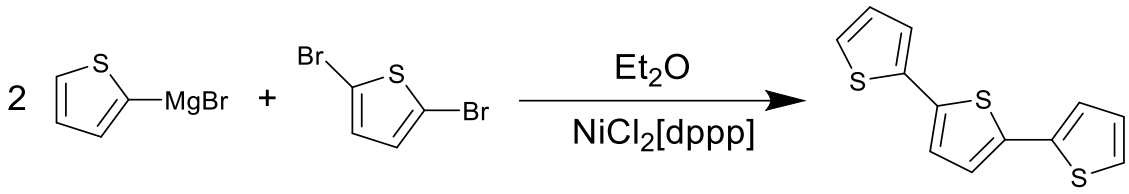

Scheme 6 Synthesis of 2,2':5',2'-terthiophene

Add 2-Bromothiophene (11.41 g, 6.8 ml) to a flask flushed with N_2 containing dry diethyl ether (Et_2O) (50 ml) and Magnesium turnings (1.3 equiv.) over ice.

Allow this to react for 1 hour and then warm to room temperature.

A second flask attached to a condenser containing 60 mg of $NiCl_2$[dppp] was flushed with N_2.

Et_2O (20 ml) and dibromothiophene (7.26 g, 3.6 ml) was added to this flask.

The prepared Grignard reagent was added dropwise lasting over 15 minutes while the solution was stirred.

The mixture was heated at reflux for 5 hours.

After the reaction was completed, the mixture was quenched with 0.1 M HCl and washed with water.

The product was extracted with toluene followed by separation.

The solvent was removed and product was redissolved in a minimum amount of toluene. The product was crashed out with cold methanol and then filtered afterwards.

The product of a yellow or orange solid was obtained.

2.1.5. Graphene (oxidation of graphite, reduction of graphene oxide)

Graphite oxide is synthesized based on the Hummers' method.[7]

Graphite (3.0 g) and KNO_3 (1.5 g) were added to a 250 ml flask at 0 °C. Concentrated H_2SO_4 (75 ml) was then added slowly with stirring at temperature below 5 °C.

The mixture was stirred for 30 mins and 0.5 g of $KMnO_4$ was added in small portions below 10 °C. The reaction mixture was stirred for an additional 30 mins.

Then 10 g of $KMnO_4$ was added to the mixture gradually over 1 hr below 20 °C.

After the temperature of the mixture warmed to 35 ± 3 °C and stirred for 2 hrs, 135 ml of water was slowly dripped into the paste, causing an increase in temperature to 70 °C and the diluted suspension was stirred at this temperature for another 15 mins.

Then, it was further treated with a mixture of H_2O_2 (30%, 10 ml) and water (85 ml).

The resulting suspension turned bright yellow, and the warm suspension (about 40 °C) was filtered, resulting in a yellow–brown filter cake.

The cake was washed for three times with a warm solution of 3% aqueous HCl (220 ml), followed by drying at 40 °C for 24 hrs. Graphene oxide was obtained by ultra-sonication of as-made graphite oxide in water for 1 hr.

Graphene is synthesized by reducing graphene oxide.[8]

Graphene oxide (0.1 g) was dispersed in water (100 ml) by sonicating graphite oxide for 1 hr. Hydrazine (32 mmol) was added into the dispersion. And the mixture was refluxed in 100 °C. The reduction product was filtered and washed with water and methanol for several times.

The filter cake was dried in oven under 50 °C. The material appears to be black powder.

2.1.6. Spark plasma sintering

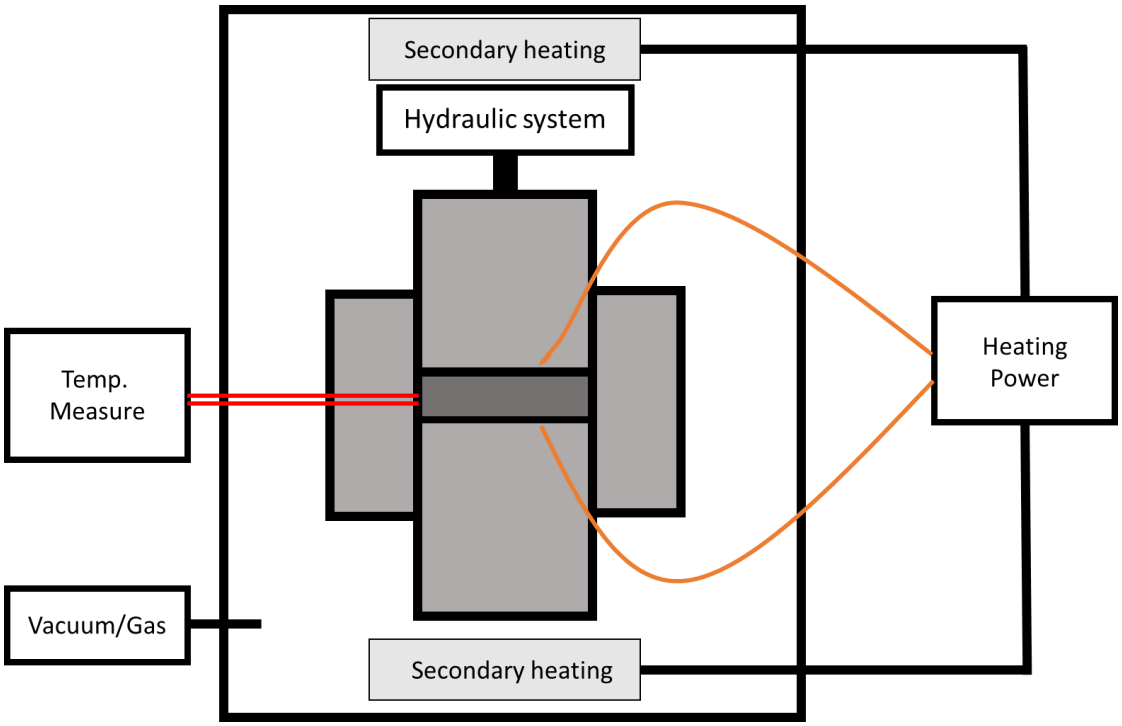

Figure 9 Spark plasma sintering process by FCT HP D 25

Spark plasma sintering (SPS), also known as Field Assisted Sintering Technology (FAST), is utilized to make sample pellets for thermoelectric measurements. This process is essentially a hot-pressing process where the mould is heated by running pulsed electric current through it. The method has a very rapid heating rate and is able to retain the original compositional state of the material. The system in use is a FCT HP D 25, which has a pressure of 25 tons. The composite sample was pre-treated by heated up to 600 °C

for 3 hrs in a tube furnace in order to get rid of all contents that would decompose in high temperature. Then the sample in powder form was put into a circular mould of 15 mm in diameter. The system is under vacuum with the 25 tons of pressure and 900 °C of heating being applied simultaneously.

Prior to SPS, the powder samples were preheated up to 600 °C for 3 hrs in a Carbolite tube furnace. Sample powder was contained in a hand-made rectangle steel box without air sealing. This procedure was hired to get rid of all volatiles, because the SPS system could not handle any material decomposing under high temperature.

2.2. Size characterisation

2.2.1. Scanning electron microscopy

Electron microscopy is a technique using electrons instead of light as a source of illumination. It uses electron beam to scan the specimen and collects backscattered electron signals to obtain information about the sample.

A scanning electron microscopy (SEM) holds several advantages over traditional microscopy. Firstly, the electron has a much shorter wavelength than light, which means a much higher resolution due to diffraction. Additionally, the scanning electron microscopy uses electromagnets instead of normal lenses; thus, the instrument has a better control over the magnification.

A scanning electron microscope has several parts in principle. The electron gun is the source of the electron beam. A concentrated beam of electrons is generated and then aimed into a column where the electromagnetic lenses control the beam to travel down towards the sample. When the electron beam hits the surface of the sample mounted on the stage inside a vacuum chamber, it induces a series of interactions. X-rays and several

different types of electrons are ejected from the sample. And then these signals are caught by the electron detectors located above the stage.

Due to the vacuum condition of the sample chamber, the samples are dried prior to the measurements. The pellet samples, with the surface lightly polished, are directly stuck on the pin stubs with carbon conductive tabs. The powder samples are evenly spread onto the tabs on top of the pin stubs. Materials with poor conductivity are sputter coated with a layer of gold in order to improve the resolution and detail of the image.

In this work, the instrument in use was a JEOL scanning electron microscope. And the Au coating was carried out in a Quorum Technologies gold coater CC7640.

2.2.2. Transmission electron microscopy

Unlike scanning electron microscope, a transmission electron microscope (TEM) puts the electron detectors on the other side of the sample so that it detects the electrons that are transmitted through the specimen. As a result, transmission electron microscopy gives information about the internal structure of a sample, such as crystallite size and structure.

A transmission electron microscope has a similar structure as a scanning electron microscope. The electron gun is the illumination source and electromagnets are employed to control and transfer the beam into the specimen. When hitting the sample, electrons pass through or are scattered by the specimen. The image shows brighter where the beam is unscattered. The dark parts are the regions where the electrons are stopped, deflected or otherwise interrupted. There are several shades of grey due to the levels of interactions between the electrons and the sample.

The sample in transmission electron microscopy needs to be prepared into a thin specimen in order to get a fine image. The way of preparing the nanoparticle sample is

by dropping a dispersion of the material onto a grid and letting the solvent dry out before use. The solvent chosen is DCM, due to its volatility as well as its good performance in dissolving the above nanoparticles.

The TEM in use is a JEOL JEM 2100 microscope with a LaB6 emitter at 200 kV. TEM samples were prepared by drop casting DCM solution of nanoparticles onto a 200mesh carbon-coated copper grid. The grid was then left for drying naturally before use.

2.2.3. Dynamic light scattering

Dynamic light scattering (DLS) is a popular method for particle size measurement. It focuses a monochromatic light beam into a particle solution. With diffusing particles in Brownian motion, the scattering of the light causes a change in the intensity of the light. With polarizer on both sides of the sample, the fluctuation is detected by a photomultiplier. After determining diffusion coefficient of particles, particle size distribution can be calculated using autocorrelation functions.

The accuracy of the size measurement is not as good as microscopy, but the specialization in size distribution as well as the short duration of experiment makes it a good choice as a routine check for the particle samples. This method is good when considering particle size in a solution as it gives the hydrodynamic radius. Includes influence of particles on surrounding solvent.

Measurements are done on Malvern Zetasizer Nano ZS.

The sample in use is a diluted and filtered nanoparticle solution and it was contained in a quartz cuvette. The low concentration is preferred to avoid temporary congregation of nanoparticles, hence gives a better reading of the measurement.

2.3. Optical properties

2.3.1. Ultraviolet-Visible spectroscopy

Ultraviolet-Visible (UV-Vis) spectroscopy is used to measure the optical absorbance of a substance, often in the range of 200-800 nm in wavelength. When one of the electronic excitation energy matches that of the wavelength of light, some of the light energy will be absorbed by the molecule. This phenomenon shows up in the spectrum present as absorbance against this wavelength. With absorbance related to the number of molecules in the light beam, a corrected property is required so that values obtained in different situations can be compared. Molar absorptivity, also known as extinction coefficient (ε) is involved for this reason:

$$A = \varepsilon c l \qquad (2.1)$$

where *A* is absorbance, *c* is the sample concentration in moles/litre and *l* is the length of light path through the sample in cm.

The instrument in use is Shimadzu UV-1800.

2.3.2. Photoluminescence spectroscopy

Photoluminescence (PL) describes a substance emitting phonon after a valence electron is excited by a light beam absorbed. In this thesis, the case in discussion is fluorescence where emission of a photon is from the singlet excited state to the singlet ground state or between any two energy levels with the same spin. Photoluminescence spectroscopy is a way of measuring emission wavelength and strength of a fluorophore.

The fluorescence spectrometer used is LS55 from PerkinElmer.

2.3.3. Quantum yield

Quantum yield measurement reveals the efficiency of the material as a fluorophore. Fluorescence quantum yield is the ratio of photons emitted to the photons absorbed in the photoluminescence process:

$$Q = \frac{photon_{em}}{photon_{abs}} \qquad (2.2)$$

The absolute quantum yield is difficult to measure and requires specific hardware. The relative quantum yield takes a simpler path by comparing the sample to a reference with a known quantum yield. There are two methods to choose from while measuring the relative quantum yield. The first one is single-point method, where only one solution of fluorophore is analysed along with the reference with same concentration. The quantum yield is calculated as such:

$$Q = Q_R \frac{I}{I_R}\frac{A_R}{A}(\frac{n}{n_R})^2 \qquad (2.3)$$

where *I* is integrated fluorescence intensity, *A* is absorption, *n* is refractive index of solvent and subscript *R* is referring to the reference used. This method requires less time and effort, but any inaccuracy during experiment would lead to an unreliable result. The other method is called the comparative method, which requires several sample and reference solutions with a series of concentrations. By plotting the integrated fluorescence intensities against the absorptions of fluorophore solutions, the slope of the fitted line is used to calculate the quantum yield using equation:

$$Q = Q_R \frac{m}{m_R}(\frac{n}{n_R})^2 \qquad (2.4)$$

where *m* is the slope, *n* is refractive index and subscript *R* is referring to the reference used. By keeping the measured absorption between 0.01 and 0.1, the plot is assured to be linear.

Rhodamine dyes are often used as reference fluorophore. Rhodamine 6G and rhodamine B are most frequently used as they require water as the solvent. Rhodamine 101 is another in the family, which possesses a quantum yield of 100% in ethanol solution.[9]

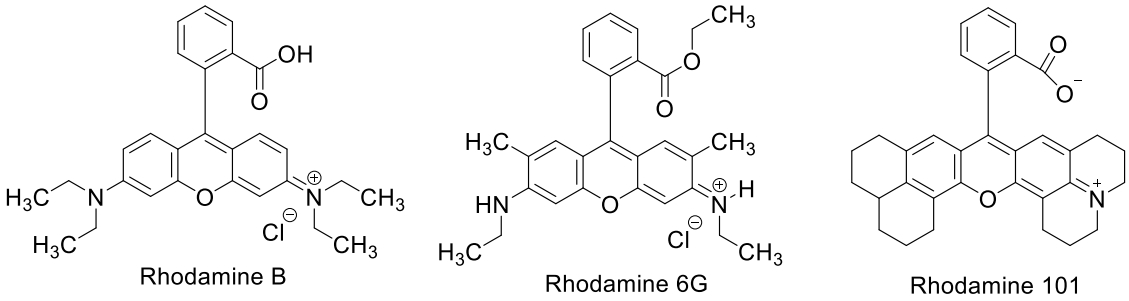

Scheme 7 Structure of Rhodamine dye family

The UV-Vis spectrophotometer and fluorescence spectrometer are utilized, along with a quartz cuvette.

2.4. Elemental analysis

2.4.1. X-ray photoelectron spectroscopy

X-ray photoelectron spectroscopy (XPS) utilizes photoelectric effect to analyse elemental composition of the surface of a sample.

The photon was applied by a fixed-energy X-ray beam onto the surface of the sample, and absorbed by a surface atom, inducing a photo-ionization of the atom and the emission of an inner shell electron. Afterwards, the kinetic energy distribution of the photoelectrons is measured by an analyser.

The experiment is carried out in an ultrahigh vacuum environment so that the emitted electrons can be received by the analyser without interacting with gas inside the chamber.

With each element having a unique binding energy related to their core orbitals, X-ray photoelectron spectroscopy is able to distinguish between elements. In practice, however, hydrogen and helium cannot be easily detected due to the X-ray source.

As a surface analysis technique, the sample could be press into a pellet or mounted on a substrate. The pellet sample needs a good electrical conductivity in order to keep a grounded connection. Whereas the substrate for mounted sample has to be made of different elements from the ones pending analysis.

The two different ways used for sample analysis on a substrate. The first preparation was by drop casting dispersion of nanoparticles onto a pure gold foil. With gold having a specific elemental trace unlike all other elements in the sample, and being a good conductor, this substrate helped get a spectrum without any interference. The second kind was by pressing the powder sample into an indium foil. With the powder being unable to stick on the surface of a gold substrate, indium is a soft metal was used to ensure the stability of a prepared sample ready for analysis.

The instrument of choice in this work is a K-Alpha XPS in NEXUS, Newcastle. The experiments were carried out in a UHV chamber with a pressure below 5×10^{-9} mbar. The X-ray source was Al Kα radiation at 1486.6 eV and a spot size of 400 microns.

2.4.2. Energy dispersive spectroscopy

With an X-ray detector and a pulse processor attach to an electron microscope, energy dispersive spectroscopy is able to identify elements of the sample and their relative proportions.

During the size measurement using an electron microscope, an electron beam is applied onto the sample. Besides all the scattering and ejecting of the electrons, an X-ray (photon) is excited from the sample in order to balance the energy. A detector converts X-rays/photons into voltage signals which pass into an analyser. Due to the unique energy levels and strengths of the X-ray generated from the elements, a distribution of the elements is created by computer.

As a semi-quantitative analysis and an add-in to the electron microscopy, energy dispersive spectroscopy is a convenient technique in the process of developing nanostructure materials. It acts as a quality check of the material in the aspect of the elemental composition.

EDX was performed using an Oxford INCA Energy-Wave System. The EDX sensor was attached to a JEOL SEM and a layer of gold was used as a reference. Each point of interest was chosen from a SEM image of the sample respectively. The actual points of interest were either dots or areas depending on the images. A point of interest would be chosen in a homogenous part of the specimen and it would give an average distribution of elements in the area.

2.5. Compositional and structural analysis

2.5.1. Thermal gravimetric analysis/Differential scanning calorimetry

Thermal gravimetric analysis is a method used to measure the mass changes of a sample following the change of temperature. With a pre-programed temperature change protocol and a certain atmosphere, the mass of the sample is accurately measured up to a tenth milligram scale. The kinetics of heterogeneous reactions and thermal degradation which give a weight loss or gain can be determined by analysing the data.

Differential scanning calorimetry measures the heat flow rate of a sample with change of temperature. When a phase transition or a chemical reaction is included, differential scanning calorimetry can be used to determine the enthalpy of the reaction. Additionally, using a temperature range where a material remains in a single phase, the heat capacity of this material could be computed with comparison to a reference.

By combining thermal gravimetric analysis and differential scanning calorimetry together, the instrument measures mass change and heat flow rate simultaneously. With the same experimental condition, two methods complement one another and help reconstruct what has happened to the sample during the process.

The instrument in use is a METTLER TGA/DSC 1. The heating processes were programmed and loaded with a desktop. A 70 μL platinum pan with lid was used so that it could stand the high temperature of 1100 °C during experiments. Nitrogen or air were used as the atmosphere for the experiment and nitrogen was also used as a protective gas for the instrument. The empty pan was run using the experimental method prior to the sample in order to form a background. Each reading of the initial weight would be conducted after a 30 mins settling of the balance under starting temperature.

2.5.2. Nuclear magnetic resonance spectroscopy

Nuclear magnetic resonance spectroscopy uses magnetic properties of certain atomic nuclei to determine the properties of the molecules within the material. The technique utilizes nuclear magnetic resonance phenomenon. This involves a nucleus with a ½ nuclear spin and an external magnetic field. In the field, this nucleus could stay in either a lower energy state where its magnetic field is along the direction of the external one, or a higher energy state where two fields are in opposite directions. When applying an

electromagnetic radio wave, the nucleus in the lower energy state can absorb it and is excited. This is followed by relaxation which emits a radio wave.

The effective external magnetic field of a nucleus is not only the field applied but also the magnetic effect of nearby nuclei and electrons. This makes the wave absorbed by the nucleus unique from others in different chemical environments. The difference from the zero point of the absorption is referred as chemical shift.

Due to widespread usage in organic and biochemistry, the most popular isotopes used in nuclear magnetic resonance spectroscopy are ^{1}H and ^{13}C. With a detailed database of materials and developed algorism of structure prediction, this method is useful in both determining the structure of an unknown molecule and proving the successfully synthesis of an existing compound.

The instrument in use is a BRUKER 500 MHz NMR spectrometer along with Topspin as the data-processing software. The prediction was done with the support of ACD/I-Lab.

2.5.3. Fourier transform infrared spectroscopy

Infrared region could be divided into near-infrared region, mid-infrared region and far-infrared region. Among which, mid-infrared spectroscopy is used to identify functional groups in a molecule. With different molecular vibrations, a sample molecule absorbs specific wavelengths of infrared radiation. The wavelength of the absorption peak is related to the vibrational energy gap.

Due to the long preparation time and poor spectral reproducibility of solid sample in traditional infrared spectroscopy, the attenuated total reflectance is used. This instrument measures a totally internally reflected infrared beam. With sample on top of the ATR crystal, the absorbance occurs on the contact surface and only several microns into the

sample. With solid material used for this measurement, the only requirement for the sample is to be able to pressed down to give direct contact with the crystal.

Nanoparticle and powder samples were measured by spreading dried material directly onto the crystal window.

The measurement of the specimen was made of 64 scans and a background scan was performed beforehand.

The instrument in use is a PerkinElmer Spectrum Two with UATR module.

2.5.4. Raman spectroscopy

Raman spectroscopy is a complementary technique of infrared spectroscopy based on the Raman effect.

By using a laser light to excite the sample, the energy level of the ground state electronics rises into a virtual state and then instantaneously relaxes back to ground state along with the light scattering. Most of scattered radiation keeps the same wavelength as the incoming one. This is known as Rayleigh scattering, where excited electrons go back to their initial state. However, a small amount of the excited electrons falls into different state levels, causing what is called a Stokes Raman shift. Additionally, if the process initiates from an excited state and ends in the ground level, the shift makes the signal energy higher than Rayleigh scattering instead of lower, like the Stokes Raman shift, causing an anti-Stokes Raman shift. Both shifts are unique to the sample, which provides important information about molecular structure after detecting signals and converting to a spectrum.

As another vibrational spectroscopy, Raman spectroscopy focuses on non-polar group vibrations which only gives weak infrared signals. However, those typical vibrations in an infrared spectrum involving strong dipolar moments are weak in a Raman spectrum.

The instrument in use is a FRA 106 Raman module attaching to a BRUKER IFS 66 FT-spectrophotometer along with a germanium detector cooled by liquid nitrogen. A KLASTECH-karpushko Nd-TAG laser at 1064 nm is equipped as the exciting source.

Pellet samples were measured by hitting them with laser beam directly. Powder samples were either contained in a small vessel just like a NMR tube or pressed into a porous steel pellet. Powder-form sulphur is used as a reference while adjusting the focus of the detector to get stronger signals. 1000 spectral scans with 2 cm^{-1} resolutions were accumulated to improve the signal-to-noise ratio.

2.6. Thermoelectric measurements

The efficiency of a thermoelectric material is defined by its figure of merit(ZT), which is a dimensionless figure depending on Seebeck coefficient(S), thermal conductivity(λ), electrical conductivity(σ) and temperature(T) by the formula:[10]

$$ZT = \frac{\sigma S^2 T}{\lambda} \qquad (2.5)$$

Seebeck coefficient is measured using Seebeck effect. When one end of the material is heated up, electrons are excited and free to move towards the cold side. The movement of the electrons induces a voltage between the two ends. Computation of Seebeck coefficient is written as:

$$S = \frac{\Delta V}{\Delta T} \qquad (2.6)$$

Due to the existence of wires attaching to each end during the measurement, the actual calculated result is from the combination of two materials. In order to find the absolute Seebeck coefficient, a reference is measured in the same condition as well, resulting an altered equation:

$$S_{sample} = \frac{\Delta V_{sample} - \Delta V_{reference}}{\Delta T} + S_{reference} \quad (2.7)$$

Thermal conductivity is given by the ratio of heat flux to the thermal gradient.

$$K = \frac{Q/A}{\Delta T/\Delta L} \quad (2.8)$$

Where Q is the quantity of heat flow, A is the area crossing the thermal gradient ΔT is the temperature difference and ΔL is the length of material over which the temperature difference being measured.

While the area, length and temperature difference of the material could easily be measured, but there is not a simple way of directly measuring heat flux. One way is to use a reference on both side of sample in the direction of the heat flux. When having the reference material which is the same length as the sample, the thermal conductivity of the sample can be calculated by the equation:

$$K_s = K_r \frac{\frac{\Delta T_{r2} + \Delta T_{r1}}{2}}{\Delta T_s} \quad (2.9)$$

The other way of calculating thermal conductivity is by measuring thermal diffusivity, heat capacity and density of the material instead. This is the chosen method for this work.

The thermal diffusivity was measured by NETZSCH LFA 457 using a laser flash method. In which, a pulsed laser is utilized as a source to heat up the front surface of the specimen and the temperature change of back surface was logged using an infrared sensor.

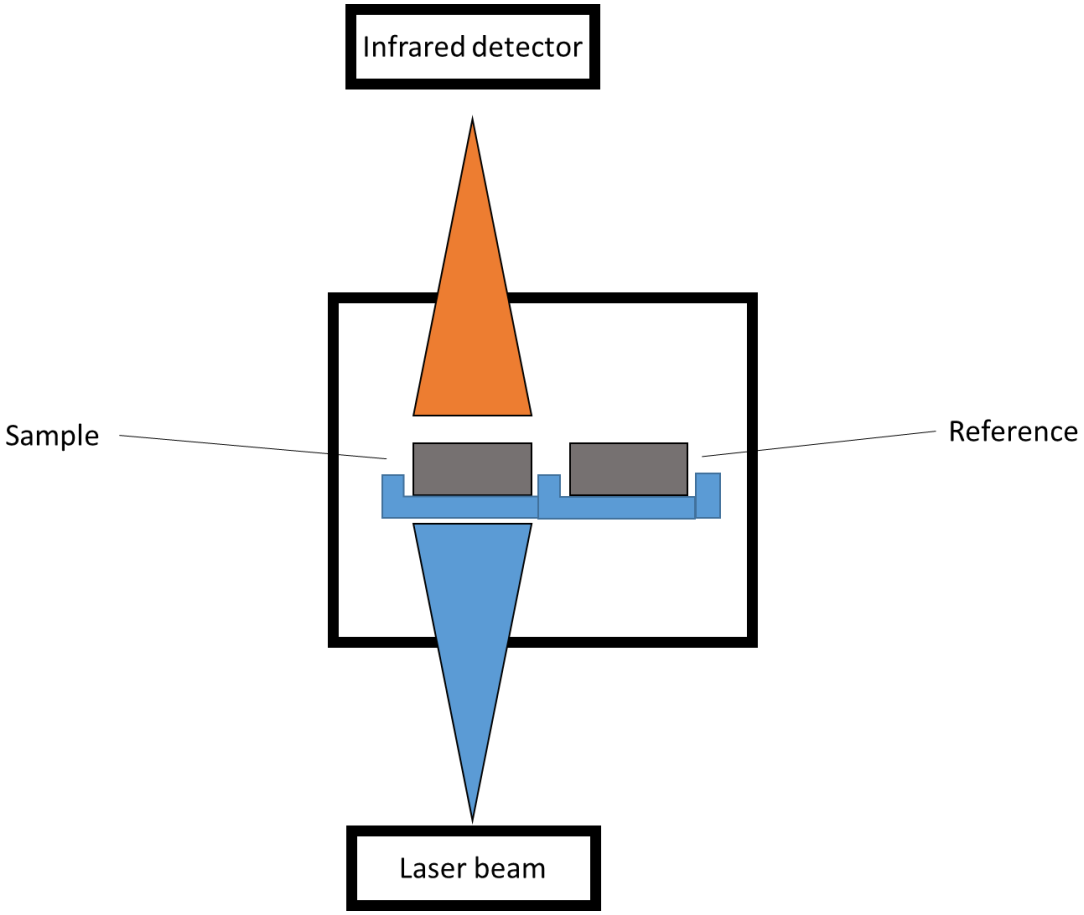

Figure 10 Measuring thermal diffusivity by LFA 457

A LSR-3 Linseis was employed to measure the Seebeck coefficient and electric resistivity. The instrument had the sample mounted between two electrodes with constant current running through. With a heater in the lower electrode, the vertically positioned sample was heated to create a set of temperature gradients. Two temperature gradients were measured by contact thermocouples.

2.7. Muon spin spectroscopy

The μSR technique is employed to investigate the electron transfer of the conductive polymer capped SiNPs material. Avoided Level Crossing Muon Spin Resonance (ALC-μSR) and Transverse Field Muon Spin Rotation (TF- μSR) are used in these experiments.

With an external magnetic field of parallel direction to the travelling muon, ALC- μSR monitors the integration of polarization of the particles.[11] It is known to study the dynamic and local environment of the muoniated radicals. In a high magnetic field, the eigenstates of radicals are considered as pure Zeeman states. However, when the field applied reaches a specific value, the mixing between states with muon, electron or nuclear spins causes a loss in time-integrated asymmetry and gives a sharp peak when polarization is plotted against external magnetic field.

Since the peak position is related to the hyperfine coupling of muon and proton in the radicals, the variation of hyperfine coupling constant could be used to determine the position of the muonium and the dynamics. The computer simulation is a good way of predicting the polarization of muon spin and the interaction between muons, electrons and nuclei.

TF-μSR is conducted with external field applied transverse (90°) to the muon beam direction. With chosen field at 1000 Gauss, the hyperfine coupling occurring on phenylacetylene ligand is explored directly. In this spectrum, a pair of frequencies are observed which only related to applied field and isotopic hyperfine constant. Based on this, a correlation function is utilized and the radical signal is revealed.

Gaussian, the computer simulation software package is used to imitate the polarization of muon spin in the muoniated model molecule, tetrakis (2-phenylethynyl) silane. Due to the similar molecular environment of the ligands between molecule and capped nanoparticle, the simulation gives a good idea of where the signal will be. In turn, helped choose the field range of the experiments and determine the muoniating site for the experiments.[12]

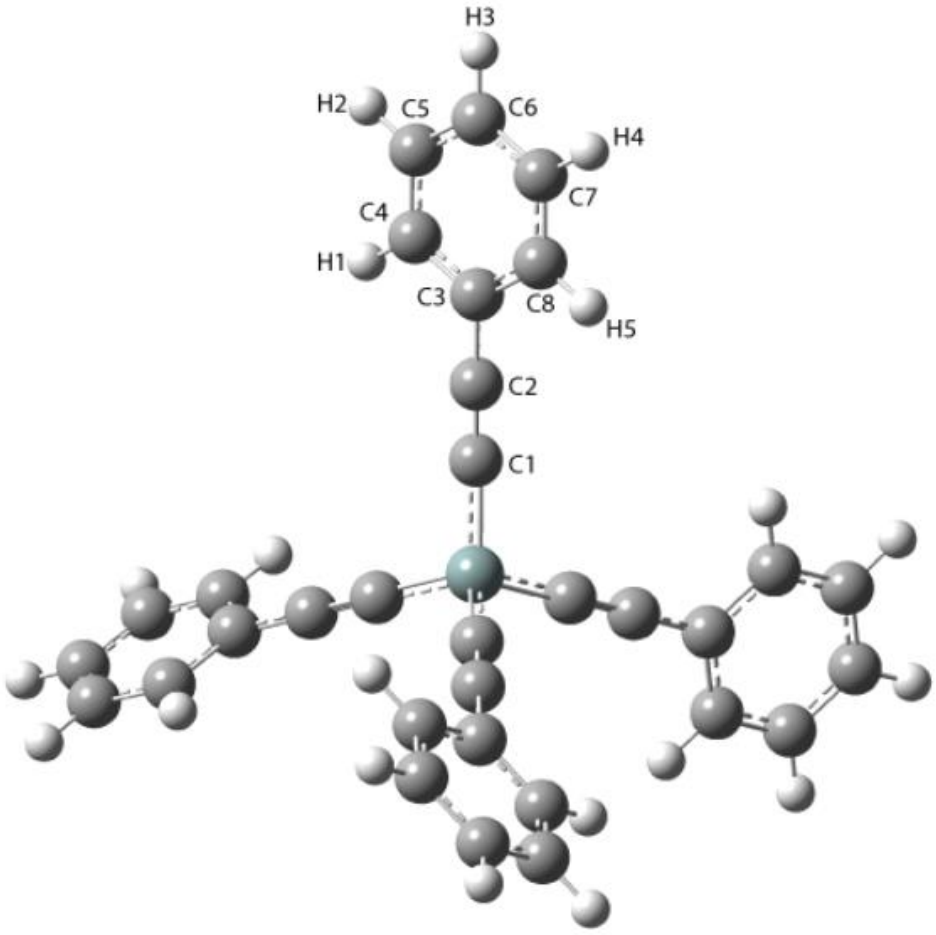

Figure 11 Gaussian generated 3D model of tetrakis (2-phenylethynyl) silane

HIFI, the instrument in use during this experiment, is the one specially equipped with high longitudinal magnetic field up to 5 T, hence the name. With the simulation signal in range, the high field is the reason for choosing it.

The muon was produced by a decay of pion, which was, in turn, produced by hitting a graphite target using a proton beam with energy of 800 MeV. The muon contains an energy level of around 4 MeV, it would penetrate into the sample and travel for a very short distance before it stops and interacts with the surroundings. With a mean lifetime of 2.2 μs, muon also decay and positrons were emitted. The detectors in the instrument

was used to keep track on these positrons. HIFI contains 64 detector elements divided into forward and backward banks.

Closed Cycle Refrigerator (CCR) is a major part of the instrument in use. It is essential a sample holder with the ability of controlling its temperature from base temperature (3 K) up to 700 K (Figure 12). It works with a liquid helium compressor to obtain the low temperature and a heating system for higher. A thermometer is attached directly to the sample holder to measure, monitor and control the temperature of the sample. With the balance of heating and cooling, the programmed temperature will be obtained accurately.

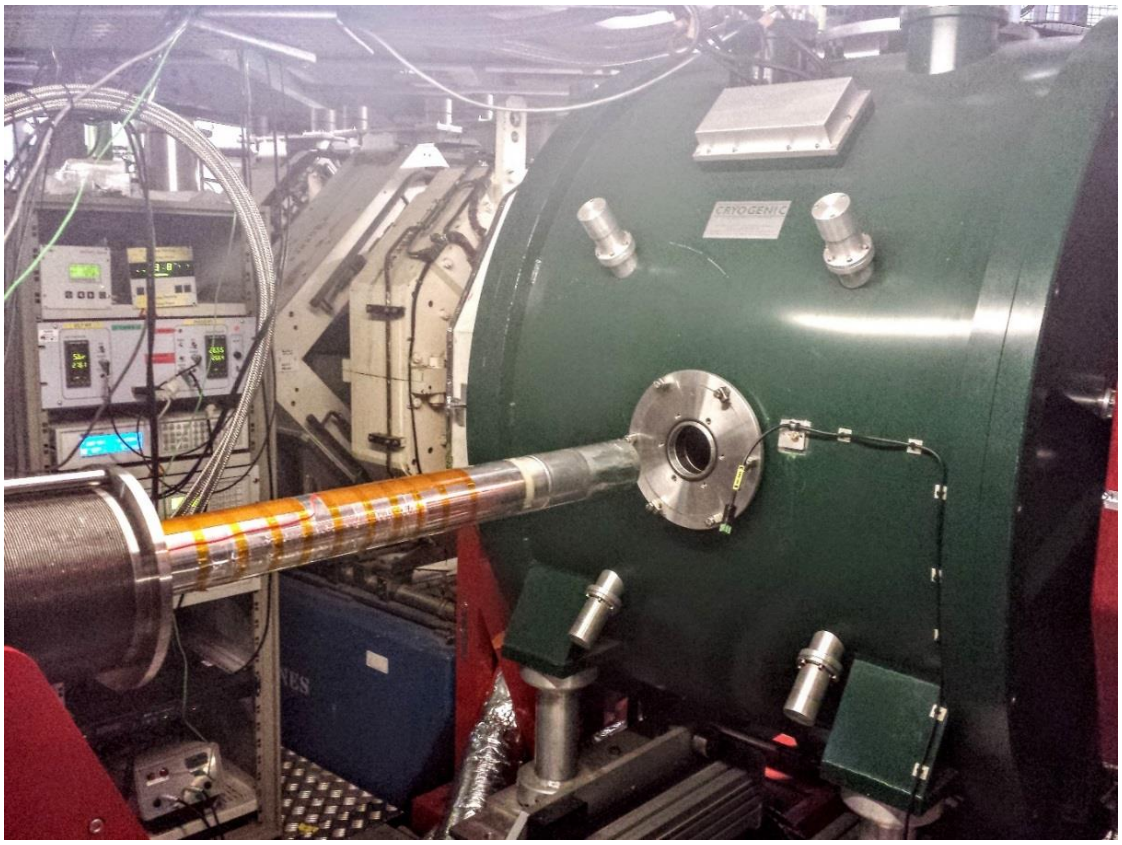

Figure 12 HIFI equipped with CCR at ISIS

The samples were mounted onto CCR and then the CCR was slided into the side port of the instrument, with the sample window facing the incoming muon beam.

After mounting the sample into the instrument, the ground was cleared and experiments were controlled by scripting in the ISIS Sample Environment Control Interface (SECI).

By controlling experiment temperature range not to go above decomposing point, solid samples were easy to prepare. After mounting into a holder and covering with a Kapton foil, the vacuum inside HIFI will get rid of oxygen which would react with muon and resulting in no spectrum from the experiment.

Liquid samples are prepared in a different way. The solution needs to go through several rounds of freeze-pump-thaw process in order to remove oxygen from the system. Samples were dissolved in degassed THF. A 15 ml of this solution was transferred into a custom-made 250 ml flask called a bulb. The bulb was connected to the freeze pump thaw and the solution was frozen using liquid nitrogen. After slowly opening of the valve on the bulb, then with the help of a roughing pump and a turbo pump, the pressure of the system would get down to 10^{-6} mbar. By this point, most of oxygen inside the bulb would be removed. However, some will still be trapped inside the frozen solution, especially when comparing to the existing high vacuum state. With the valve sealed, the solution was heated by a heat gun to let the gas out from the solution. With several rounds of freezing, pumping and warming up, the solution sample was degassed and oxygen-free. Afterwards, the solution was transferred into a HIFI sample holder inside a glovebox. The sample holder was totally filled up and sealed before mounting onto the instrument for experiments.

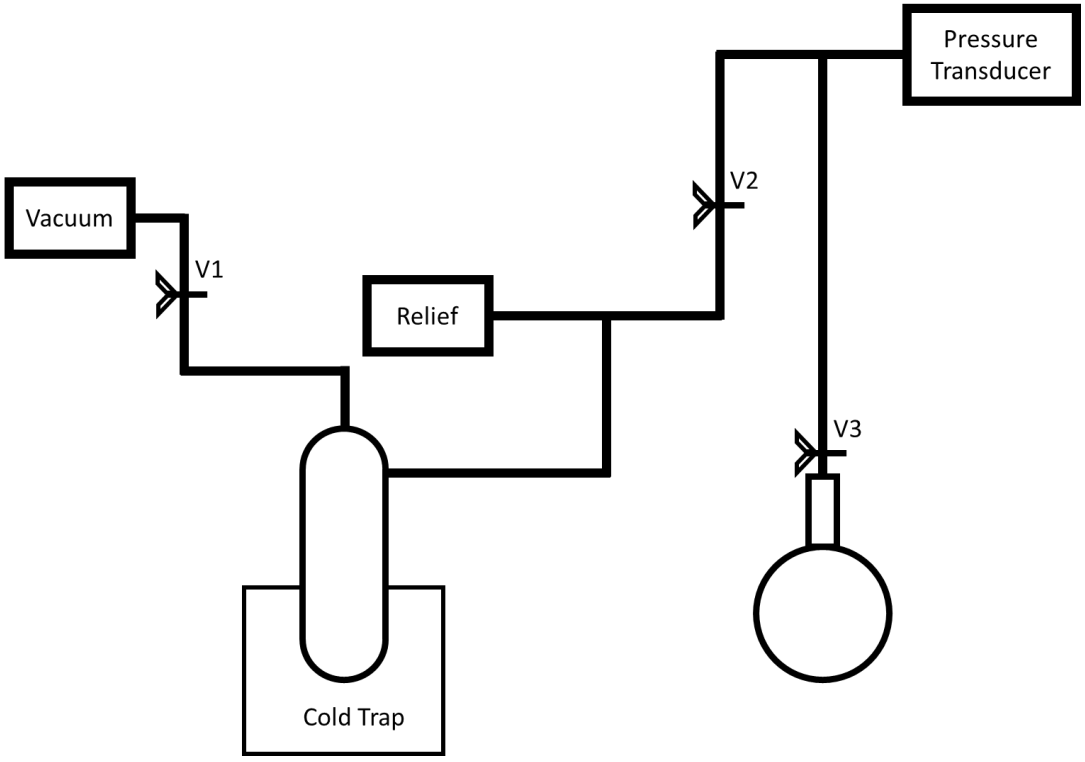

Figure 13 Freeze pump thaw system for handling liquid sample in muon experiments

GPD is one of the muon instruments located at μE1 area in PSI. With the assistance of the new chemistry cryostat, TF-μSR experiment is conducted with solution samples within the temperature range of 250 to 325 K. WiMDA is used to process the collected data. This software is developed by the muon community with a goal that raw data from different facilities could be processed in Windows OS laptop without the necessity of using remote control over Linux computer, which is the OS of choice to directly connect to the instrument.[13]

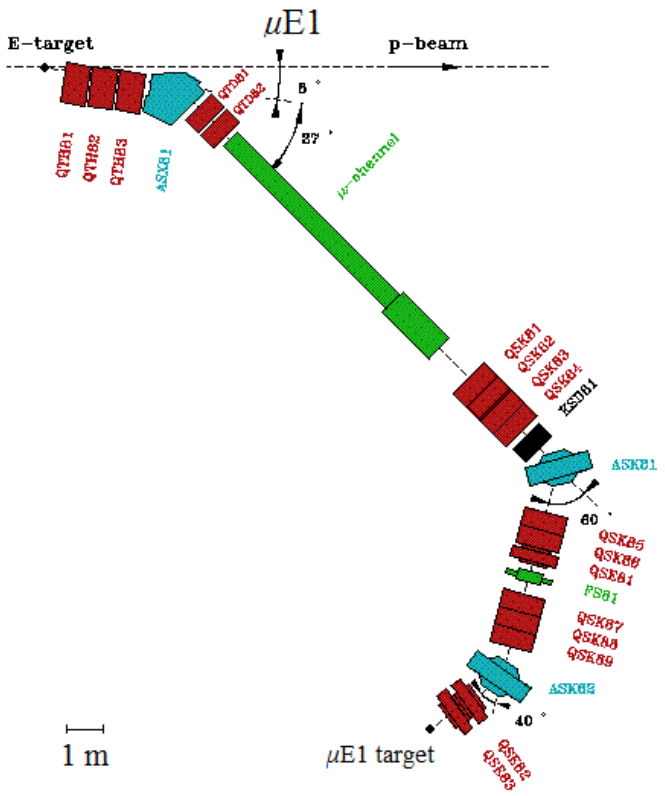

Figure 14 Layout of μE1 target area at PSI

New chemistry cryostat holds a continuous flow of N_2 gas through the sample chamber to control the sample temperature. The sample holder used is a small round bottom flask with sealed long neck to keep sample in without further contamination. This also saves the effort of pumping down the sample chamber comparing to HIFI.

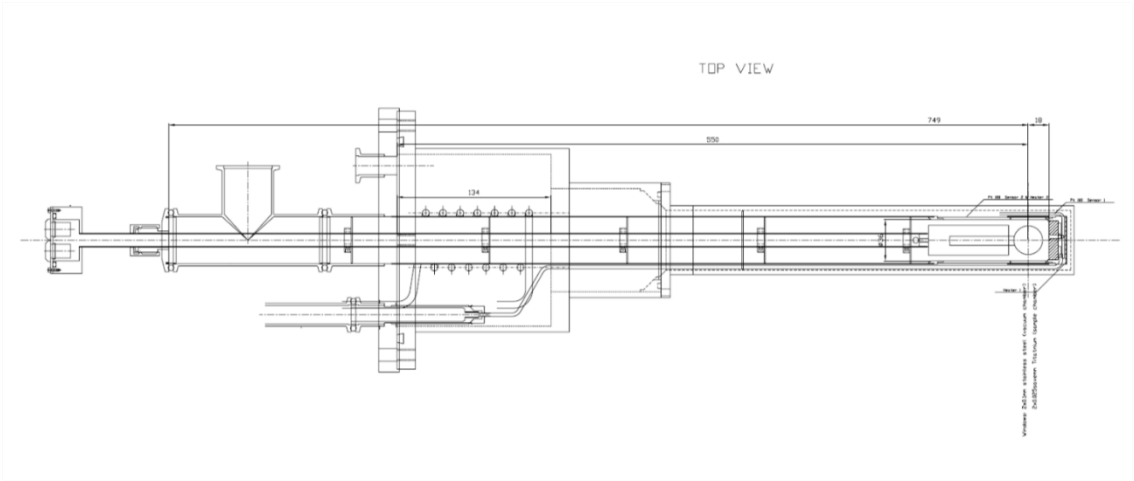

Figure 15 Sketch of new chemistry cryostat sample mounting system

Reference

1. F. M. Dickinson, T. A. Alsop, N. Al-Sharif, C. E. Berger, H. K. Datta, L. Siller, Y. Chao, E. M. Tuite, A. Houlton, and B. R. Horrocks, *The Analyst* 133, 1573 (2008).

2. M. Rosso-Vasic, E. Spruijt, B. van Lagen, L. De Cola, and H. Zuilhof, *Small* 4, 1835 (2008).

3. S. P. Ashby, J. García-Cañadas, G. Min, and Y. Chao, *Journal of Electronic Materials* 42, 1495 (2012).

4. M. Chahma, *Synthetic Metals* 155, 474 (2005).

5. C. Kim, and M. Kim, *Journal of organometallic chemistry* 563, 43 (1998).

6. B. J. J. Smeets, R. H. Meijer, J. Meuldijk, J. A. J. M. Vekemans, and L. A. Hulshof, *Organic Process Research and Development* 7, 10 (2003).

7. S. William, J. Hummers, and R. E. Offeman, *Journal of the American Chemical Society* 80, 1339 (1958).

8. V. C. Tung, M. J. Allen, Y. Yang, and R. B. Kaner, *Nature nanotechnology* 4, 25 (2009).

9. D. Magde, G. E. Rojas, and P. G. Seybold, *Photochem. Photobiol.* 70, 737 (1999).

10. A. I. Boukai, Y. Bunimovich, J. Tahir-Kheli, J. K. Yu, W. A. Goddard, 3rd, and J. R. Heath, *Nature* 451, 168 (2008).

11. I. McKenzie, and E. Roduner, *Naturwissenschaften* 96, 873 (2009).

12. J. Lord, *Physica B: Condensed Matter* 374, 472 (2006).

13. F. L. Pratt, *Physica B: Condensed Matter* 289-290, 710 (2000).

Chapter 3 Thiophene and Terthiophene capped SiNPs

Thiophene capped silicon nanoparticles are synthesized by a solution reduction reaction. This is the precursor for other products and the first step of manufacturing the thermoelectric material in discussion. Terthiophene capped silicon nanoparticles are fabricated in a similar fashion with the attempt of producing a thermoelectric material which can be used at room temperature.

Contents

Silicon nanoparticles show potential in a number of different fields of research. Their synthesis and modification raises challenges and ideas of what could be achieved. Polythiophene is one of the basic conductive polymers and a proven choice as thermoelectric material. With thiophene rings overlapped with each other and the thiophene attached as ligand on surface of nanoparticles. The would behave as a bridge to increase the electrical conductivity between particles so that a better SiNPs based thermoelectric material can be developed.[1-2] Thiophene monomer and terthiophene oligomer are the molecules used to functionalise the surface of nanoparticles in this chapter.[3]

Thiophene capped SiNPs are an ideal test subject for exploring the manufacturing of SiNPs and the bonding to organic molecules of this nature. With the help of TEM, FTIR, NMR, PL, UV and XPS, both the SiNPs and the ligands are analysed. The unified size and well-covered surface of nanoparticles are achieved, making way for further modification. Potential in thermoelectric application of the material is explored with terthiophene capped SiNPs. A doping process and cold pressing procedure are utilized to fabricate and study the properties of the bulk material. The influence of ligand extending is monitored as well to gather more information on this type of composite.

3.1. Thiophene capped SiNPs

As the first step, thiophene monomer is attached to the silicon nanoparticles.

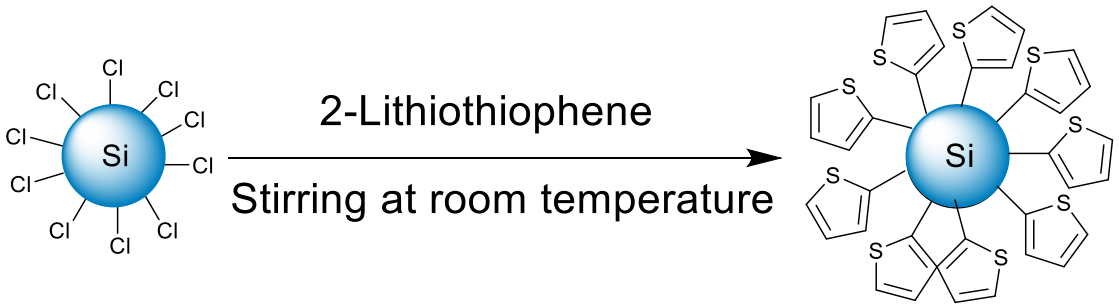

Scheme 8 Lithiation in synthesizing thiophene capped SiNPs

As described in Chapter 2, the product was synthesized by solution based lithiation (Scheme 8).

3.1.1. Characterization of sample

The product was a dark brown waxy solid. When dissolved in organic solvent with high concentration, the transparent solution presents a yellow to light brown colour.

3.1.1.1. Size measurements

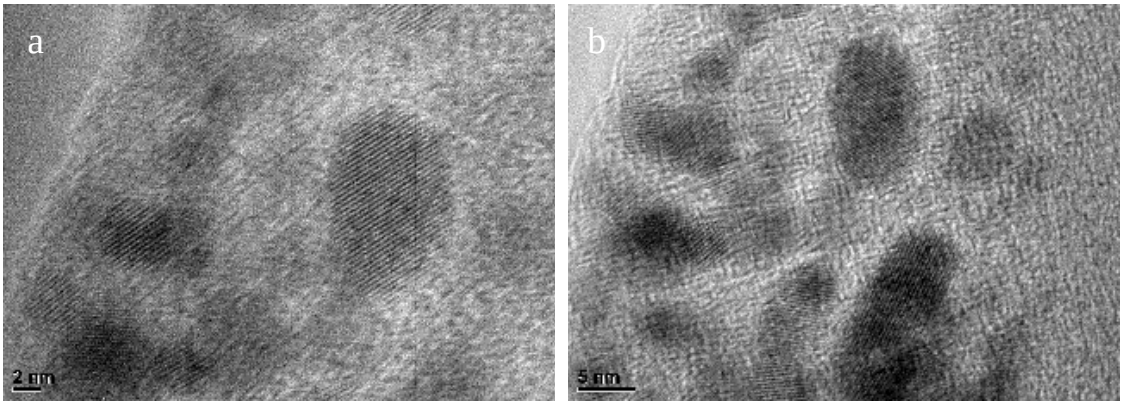

Figure 16 TEM of thiophene capped SiNPs

Using a transmission electron microscope, the nanoparticles can be seen clearly in the images (Figure 16**Error! Reference source not found.**). The crystalline structure of the nanoparticles is observable in these images, and diameters of the particles measured are around 5 nm.[4] The measurement is supported by DLS results in Figure 17.

In corroboration of the TEM measurement, dynamic light scattering (DLS) also shows a uniformed particle size distribution. The diameter of the nanoparticles is within 4 to 10 nm with the large majority in the range of 5 to 6 nm.

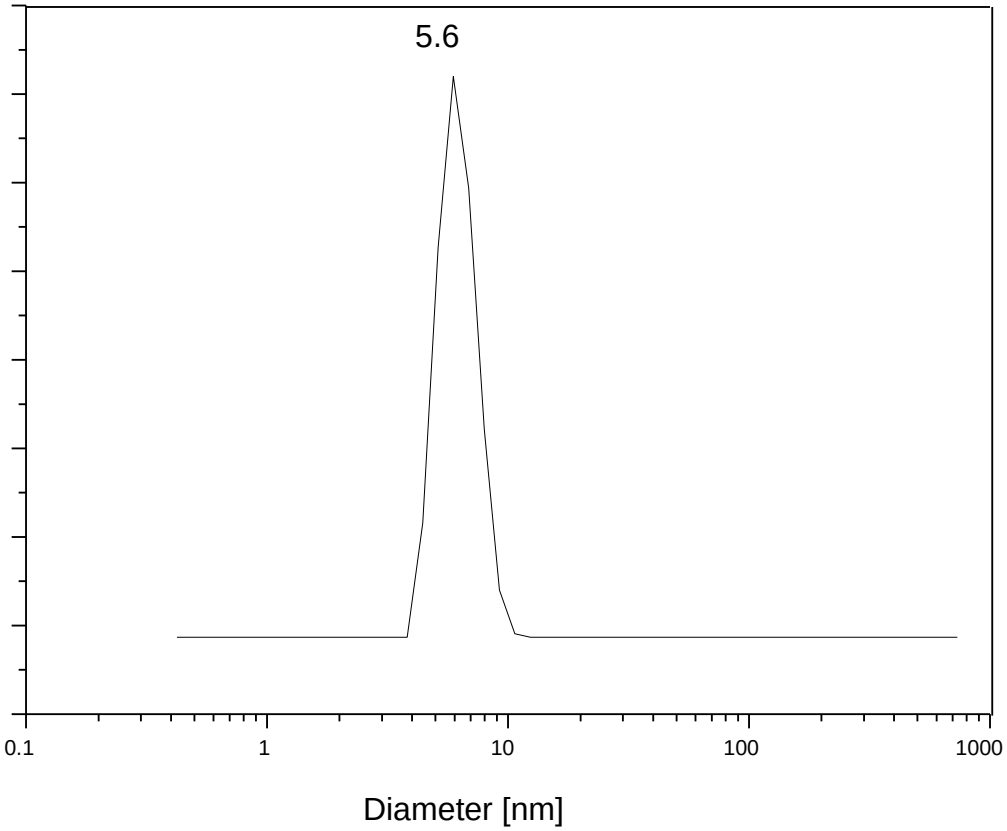

Figure 17 DLS of thiophene capped SiNPs

3.1.1.2. Elemental and structural analysis

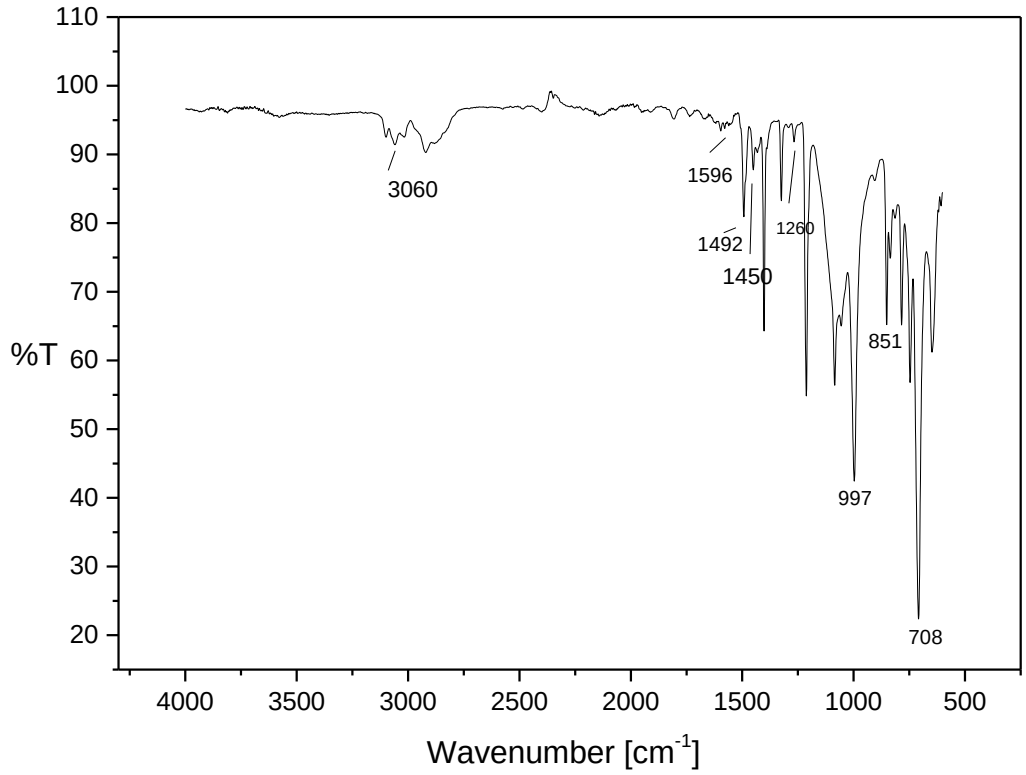

Figure 18 FTIR of thiophene capped SiNPs

FTIR spectrum in Figure 18 shows evidence of thiophene capping on SiNPs surface. The peaks at 1260 cm^{-1} and 1450 cm^{-1} are indication for the silicon-carbon bond. The 3060 cm^{-1} peak point to the aromatic C-H bond. Peaks at 1596 cm^{-1} and 1492 cm^{-1} are both representative of aromatic C-C bond. Vibrations at 997, 851 and 708 cm^{-1} are attributed to the C–S bond in the thiophene ring.[5]

H-1 and C-13 NMR spectra of thiophene capped SiNPs dissolved in chloroform are shown in Figure 19. The image in the left is proton NMR, with peaks at 7.76, 7.52 and 7.27 ppm. They are corresponding to hydrogen attaching to #5, #3 and #4 carbon, respectively. The Carbon NMR is on the right-hand side, where four peaks are shown

with positions at 138.5, 133.4, 133.2, 128.5 ppm, respectively. These results indicate the thiophene was substituted at one carbon position and only at α position (#2 carbon).

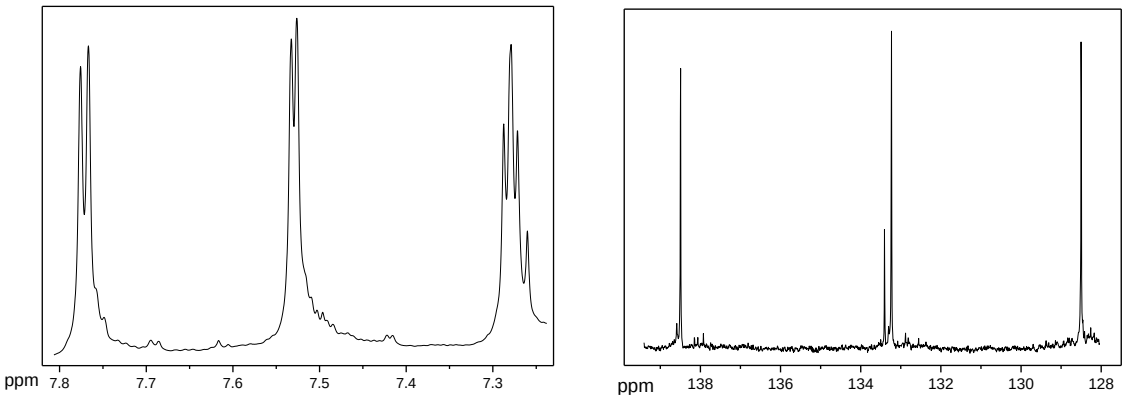

Figure 19 NMR of thiophene capped SiNPs

The appearance of shoulders around 280 nm in UV-Vis spectrum of thiophene capped SiNPs gives a proof of the existence of quantum dots (Figure 20). A blue shift is occurred to the Γ- Γ band gap transition comparing to the bulk material due to the quantum confinement.[6]

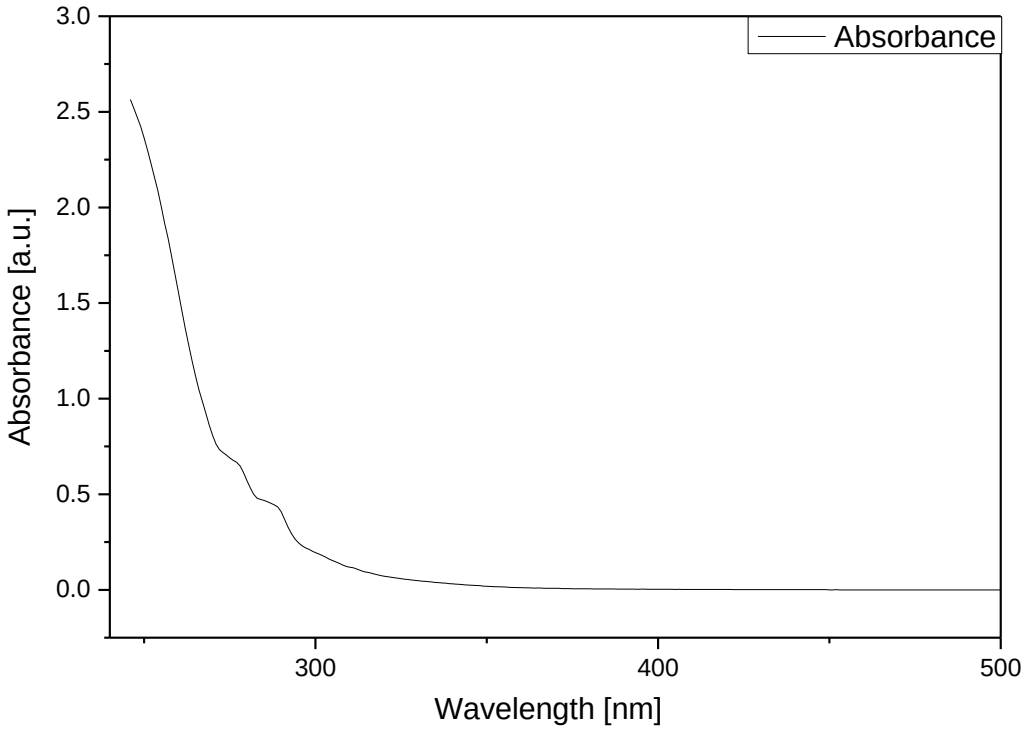

Figure 20 UV-Vis spectrum of thiophene capped SiNPs

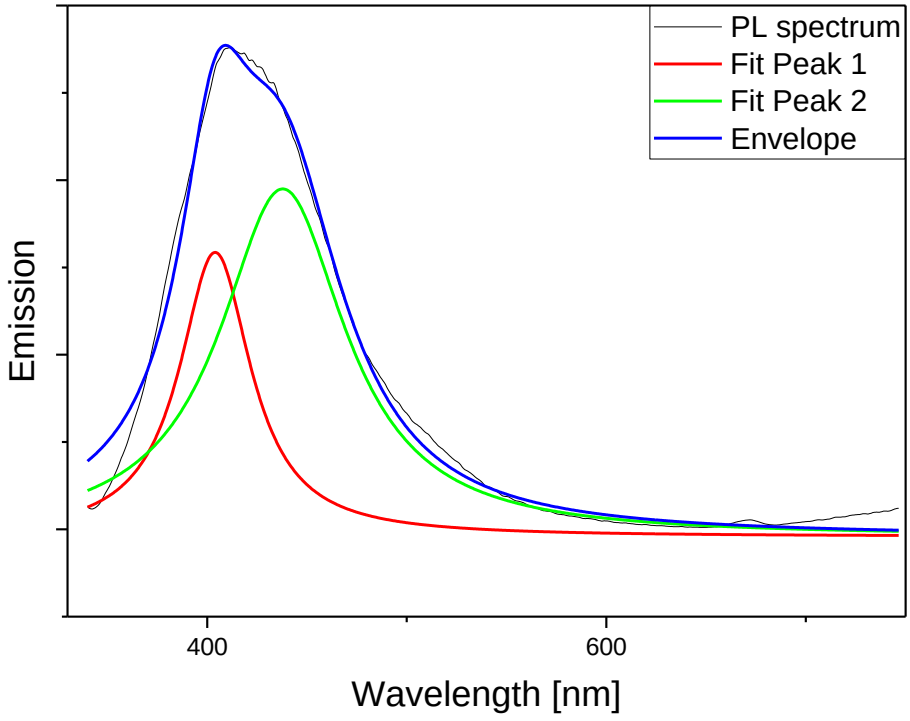

Figure 21 Photoluminescence of thiophene capped SiNPs

Photoluminescence analysis is good for exploring the structure of the inorganic part without the interaction of the surface. Shown in Figure 21, there are two symmetric peaks in the PL image, which is consistent with the existence of a nanoparticle core and the conjugated outer layer. The optimum excitation wavelength appears at 330 nm.

XPS survey spectrum shows the existence of carbon, silicon, oxygen and sulphur in Figure 22.

These elements are labelled with their corresponding orbitals. Each of these elements were scanned at higher resolution.

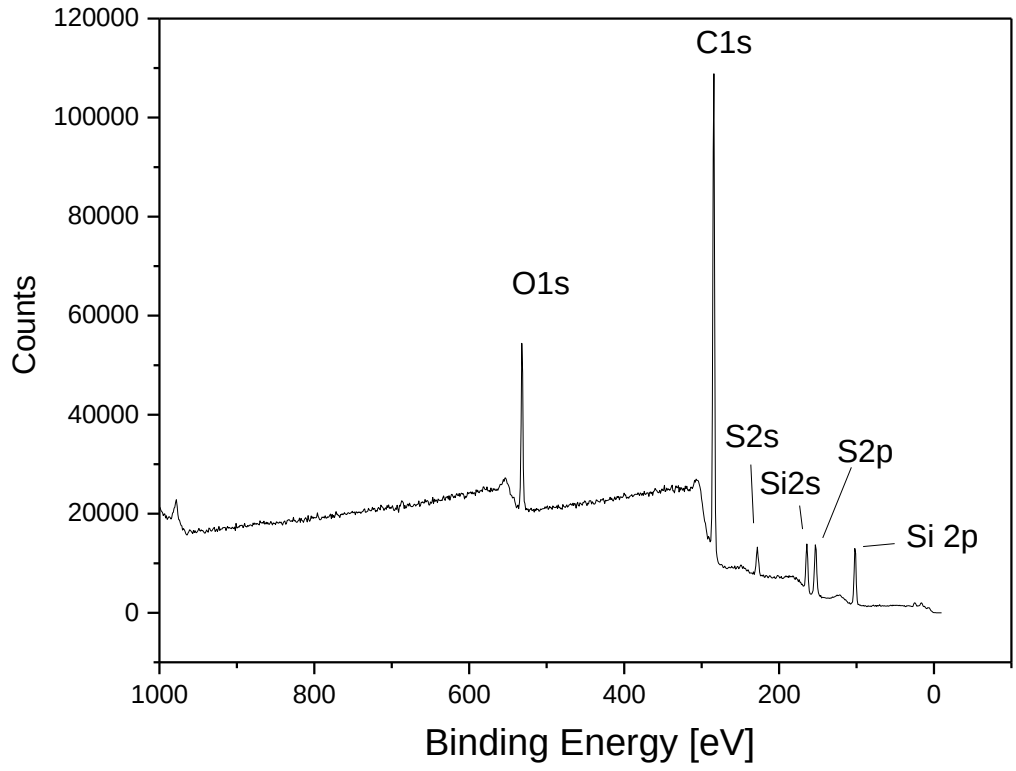

Figure 22 XPS survey spectrum of thiophene capped SiNPs

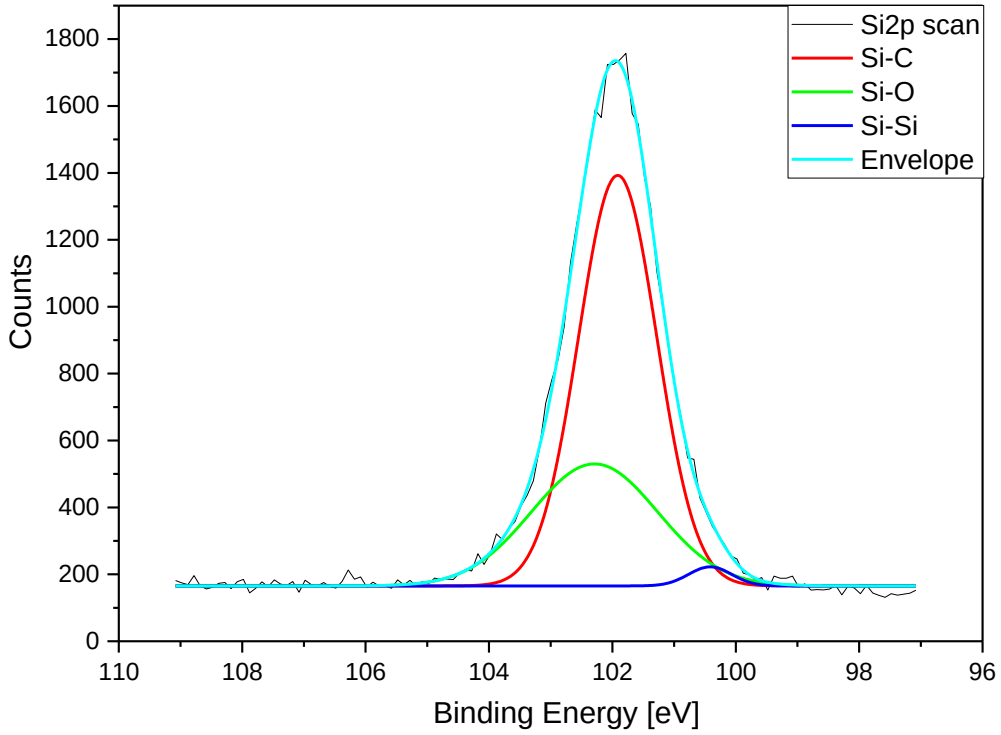

Figure 23 XPS spectrum of thiophene capped SiNPs showing Si2p region

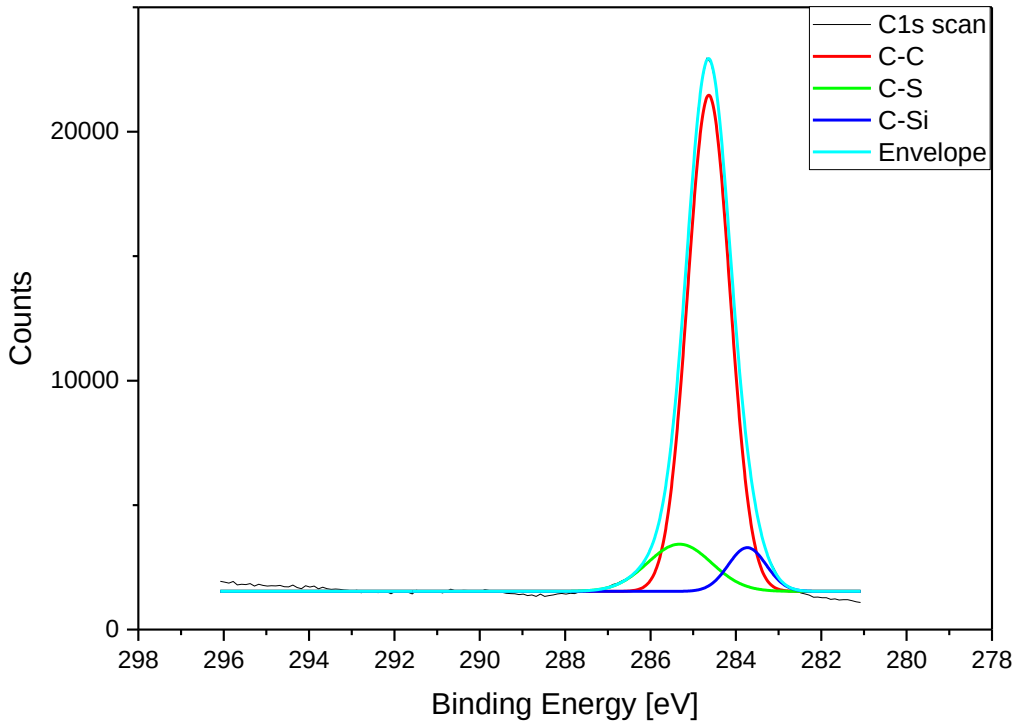

Figure 24 XPS spectrum of thiophene capped SiNPs showing C1s region

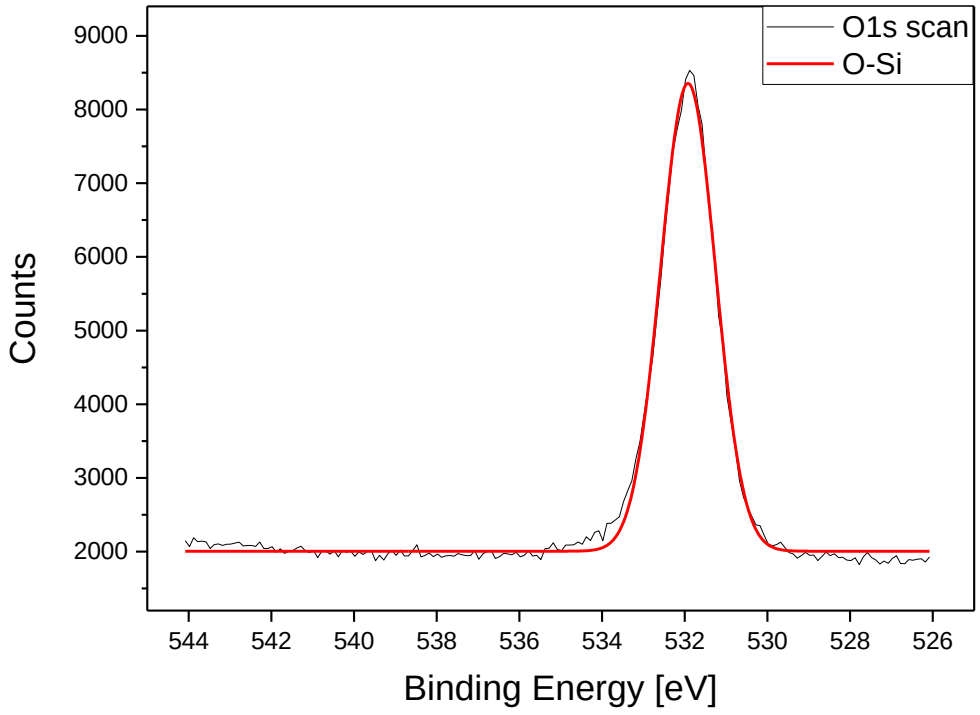

Figure 25 XPS spectrum of thiophene capped SiNPs showing O1s region

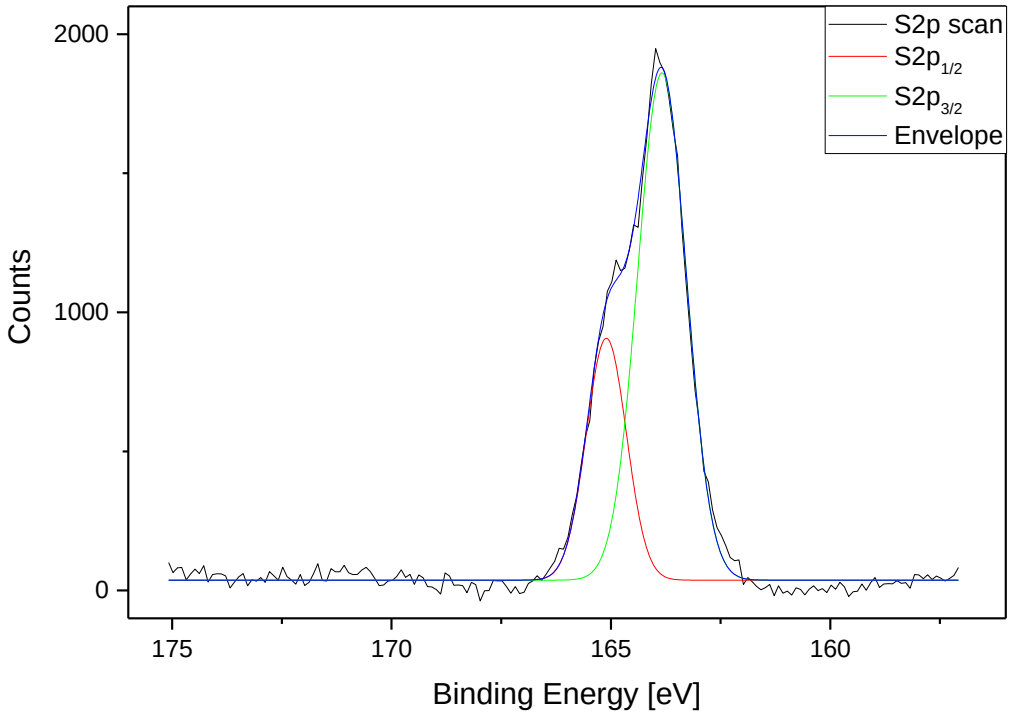

Figure 26 XPS spectrum of thiophene capped SiNPs showing S2p region

Si2p spectrum (Figure 23) is fitted with three components at 100.4 eV, 101.9 eV and 102.3 eV representing Si-Si bond, Si-C bond and Si-O bond respectively. In which, 66.4% of the total spectrum area is contributed by Si-C bond and only 1.7% by Si-Si bond within the selected energy window. It indicates 67.5% of the available nanoparticles surface capped with thiophene ligands.

C1s spectrum (Figure 24) is fitted into three components at 283.7 eV, 284.6 eV and 285.3 eV respectively. The peak at 284.6 eV representing carbon-carbon bonds within the sample takes up 81.8% of the total spectrum area, along with 11.7% by C-S bond at 285.3 eV, and 6.5% by C-Si bond at 283.7 eV. The area ratio of spectrum represented by C-Si and C-S bonds is 1.83, which is close to the expected ratio of silicon and sulphur in functionalised SiNPs (1:2). The ratio of C-C bond is higher than expected, possibly due to residual naphthalene mixed in the batch.

The significant peak of oxygen is the result of an X-ray induced oxidation. The only component fitted is the representative of Si-O bond (Figure 25).

S2p peak is clearly shown as a $2p_{3/2}/2p_{1/2}$ doublet (Figure 26) resulted from the spin-orbit splitting of p-type orbitals.[7]

3.1.2.3. Thermal stability

TGA/DSC is employed mainly to analyse the status of the ligands on the surface.

With the only drop in mass of the sample appears between 200 °C and 600 °C but two peaks shown in derivative, the breakdown of the ligand molecules follows two steps (Figure 27**Error! Reference source not found.**).

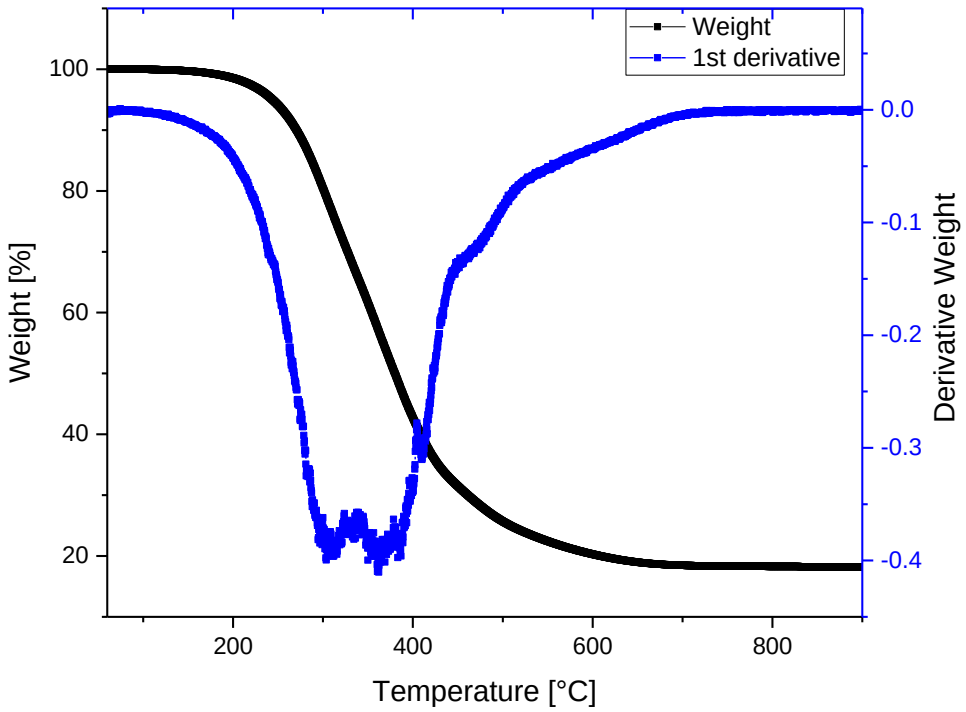

Figure 27 TGA analysis of thiophene capped SiNPs

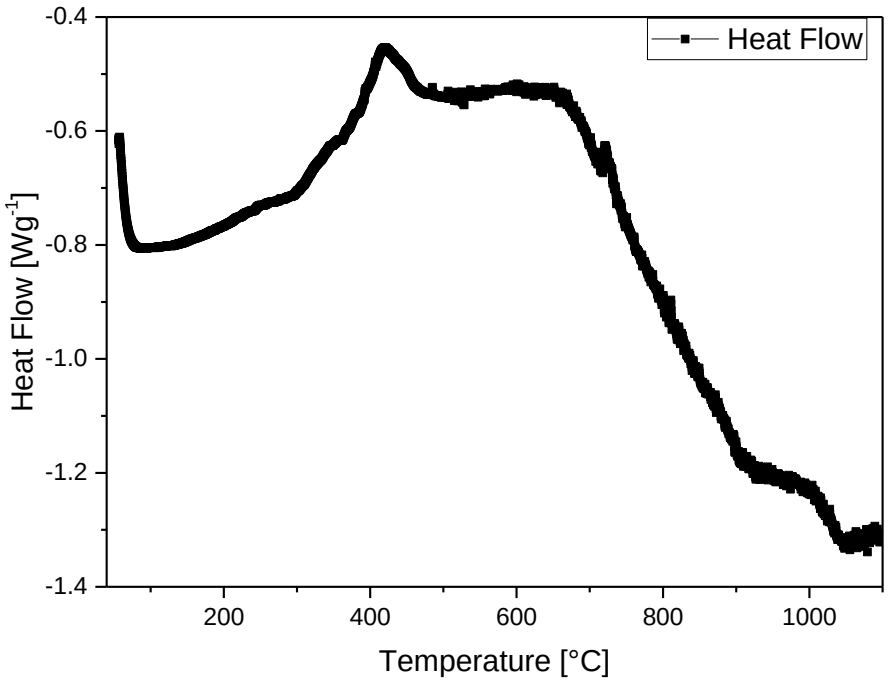

Figure 28 DSC analysis of thiophene capped SiNPs

Firstly, small gaseous molecules breakout from the thiophene in 300 °C. Then with the heating process continuing, decomposition of the organic parts attaching directly to the silicon surface occurs, resulting in a further weight loss until the remaining mass to be 20% of the original. Positive peaks in 400 °C and 600 °C from DSC curve corroborates this idea (Figure 28**Error! Reference source not found.**). DSC in high temperature (above 600 °C) are the results of heating up the bare silicon particles with a slight turbulence at 1000 °C which is due to the decay of defected amorphous silicon on the surface.

3.2. Terthiophene capped SiNPs

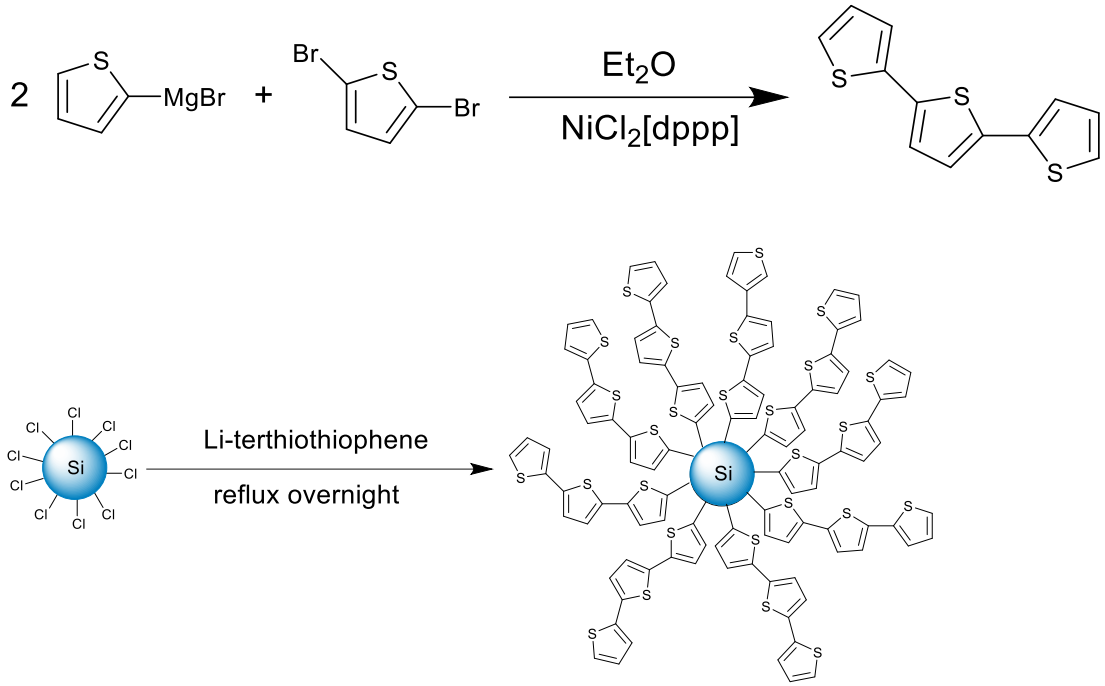

Scheme 9 Synthesis of terthiophene capped SiNPs

2,2':5',2"-terthiophene is an oligomer of thiophene. With the intension of extending the length of ligands on surface, terthiophene is produced independently and then attached onto silicon nanoparticles (Scheme 8). [3, 8]

3.2.1. Characterisation of terthiophene capped SiNPs

Terthiophene capped SiNPs are a yellow solid. Sample possesses a low solubility, especially after recrystallization in toluene. This fact is related to its lower surface coverage comparing to thiophene capped SiNPs, which also gives the purified sample a crystalline appearance.

3.2.1.1. Size and elemental analysis

FTIR is an efficient way of proving the capping of terthiophene onto the silicon surface (Figure 29). The signal at 1212 cm^{-1} is the representative of Si-C bond.[9] 1490 cm^{-1} and

1422 cm^{-1} peaks are observed as the evidence of aromatic C=C stretching, as well as 3060 cm^{-1} signal representing aromatic C-H stretching. More evidence of the existence of terthiophene comes from the three peaks lower that 900 cm^{-1}. The intense peak at 793 $cm^{-1}$is an indication of 2,5-substituted thiophene. Broad peak at 1059 cm^{-1} shows the present of Si-O in the sample.[10]

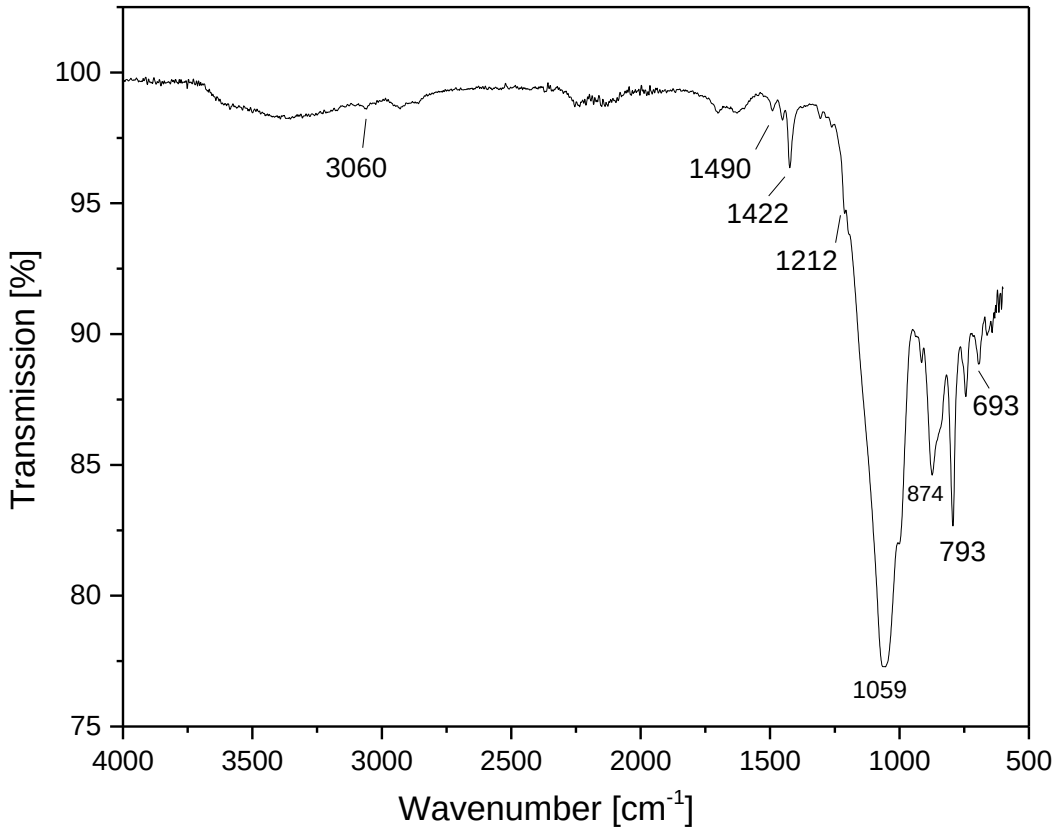

Figure 29 FTIR of terthiophene capped SiNPs

TEM image shows a fine dispersion of nanoparticles with diameter of 5.6 nm in average. Although nanoparticles are not in perfect circular shape, the crystalline structure of the nanoparticle is clearly shown in the images, especially in Figure 30(a).

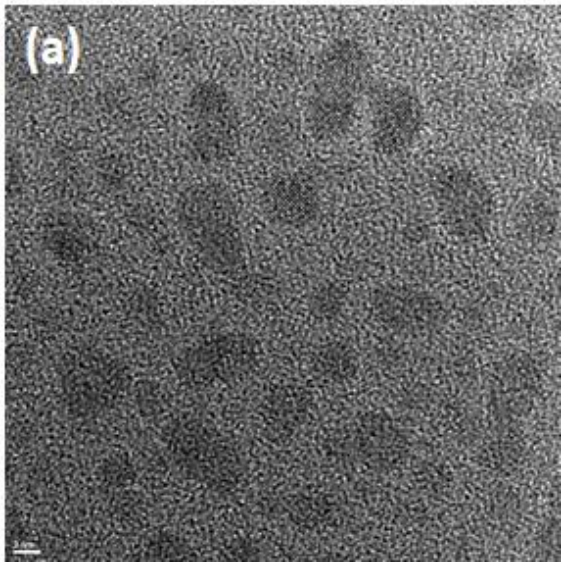
(a)

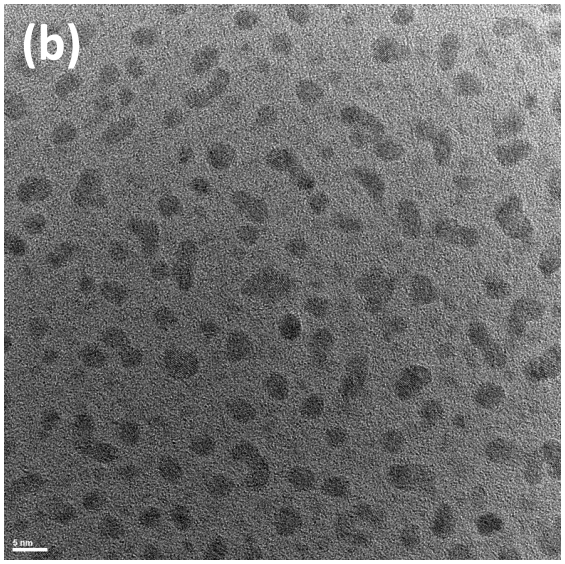
(b)

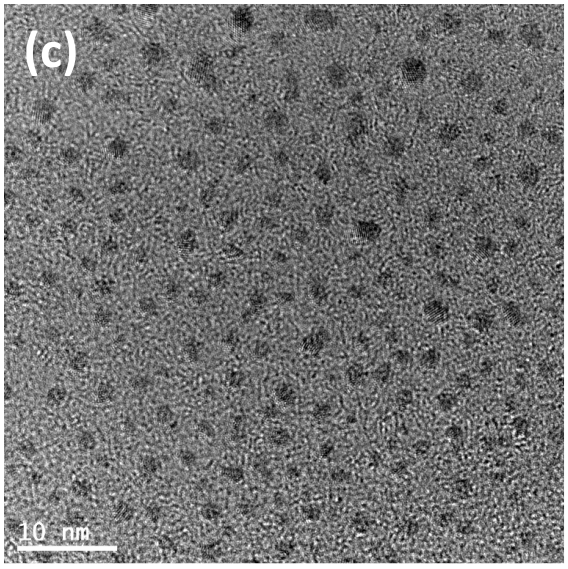
(c)
10 nm

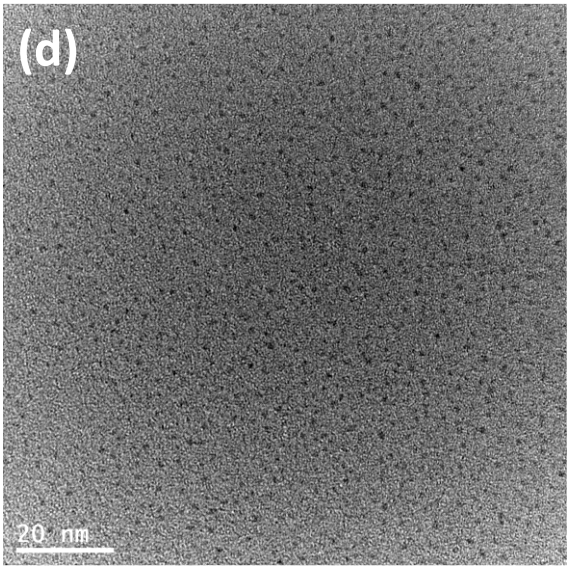
(d)
20 nm

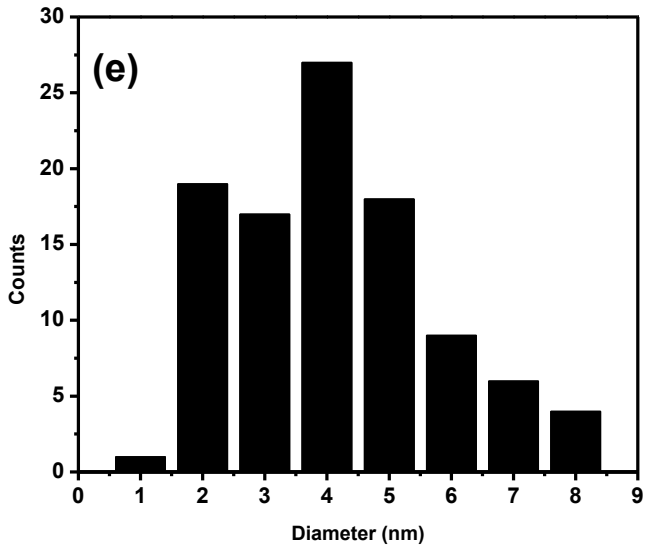
(e)
Counts
Diameter (nm)
0
5
10
15
20
25
30
0
1
2
3
4
5
6
7
8
9

Figure 30 TEM images of terthiophene capped SiNPs with scale bars show 2 nm in (a), 5 nm in (b), 10 nm in (c), and 20 nm in (d) with a corresponding histogram of nanoparticle size distribution in (e).

EDX scan in Figure 31 shows the preliminary elemental analysis of the material. Among which, silicon, carbon, sulphur and oxygen are the dominating elements. This result indicates a significant level of oxidation on the surface of the nanoparticles, which is agreed by XPS results.

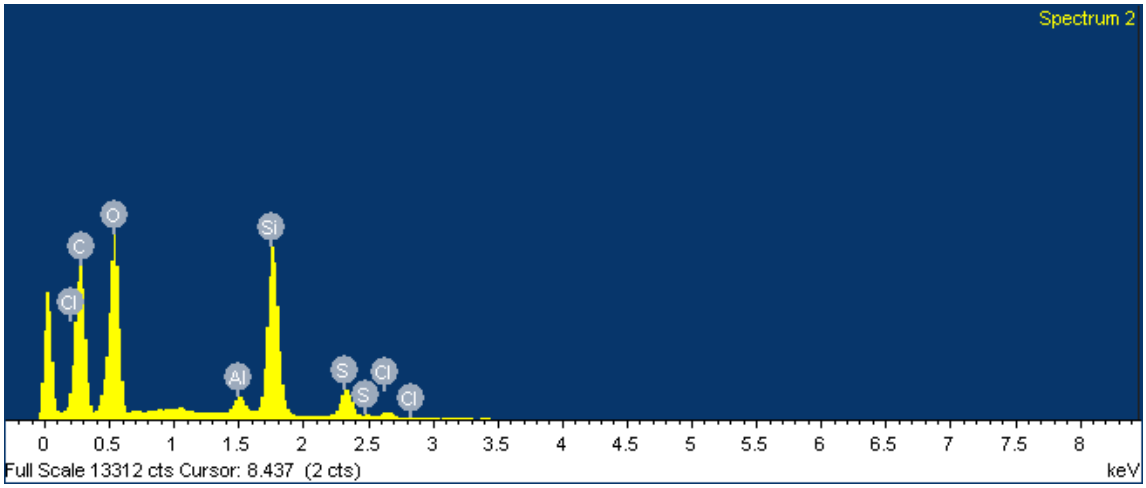

Figure 31 EDX spectrum of undoped terthiophene capped SiNPs

The XPS spectrum shows a detailed analysis of the components of the sample. Same elements appear in the scan as EDX. C1s, O1s, S2s, S2p, Si2s and Si2p signals are picked by survey scan (Figure 32).

In the Si2p spectrum, it appears to be the Si-O bonds which makes up a large proportion of the total spectrum area (Figure 33). 18.7% of the spectrum area is occupied by Si-C bond and 22.1% is by Si-Si bond. The calculated coverage of ligands capped surface would be 23.5% and the rest is oxidised. The coverage is much lower than thiophene capped SiNPs. This is mainly due to the steric effects between these extended ligand molecules during capping reaction.

Displayed in Figure 34 is C1s scan of the sample. Proportions of C-S and C-Si bond are 32.9% and 5.8%, respectively. The ratio between three types of bonds is 1:5.7:10.7 in the order of C-Si, C-S and C-C, which is close to the theoretical ratio of 1:6:11.

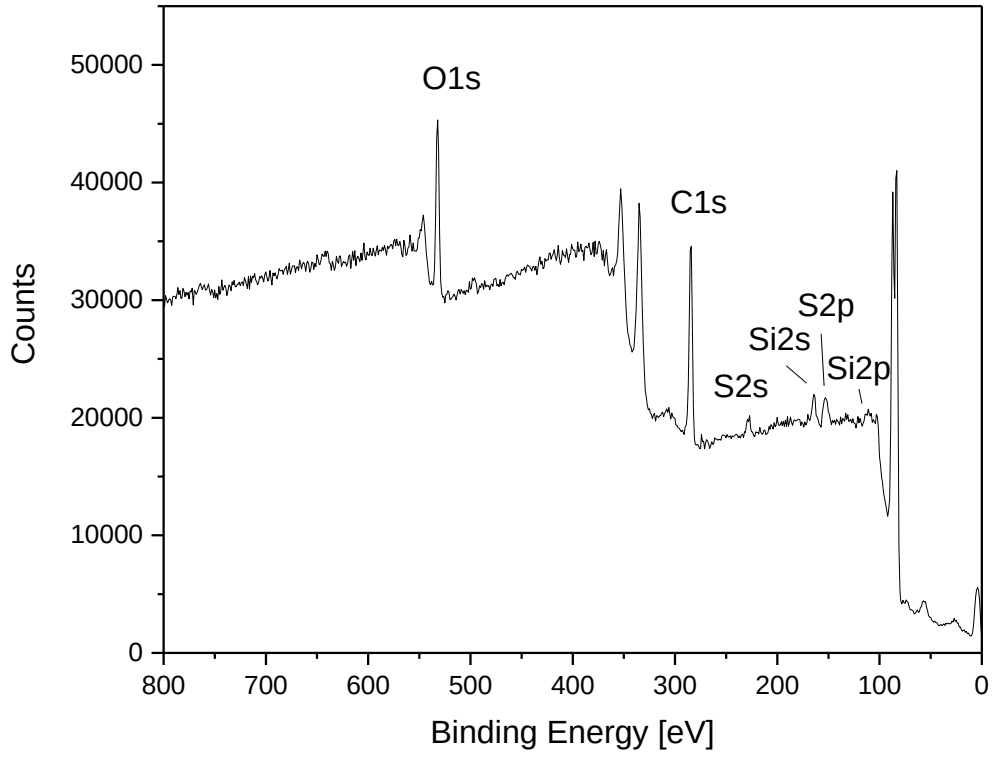

Figure 32 XPS survey spectrum of undoped terthiophene capped SiNPs

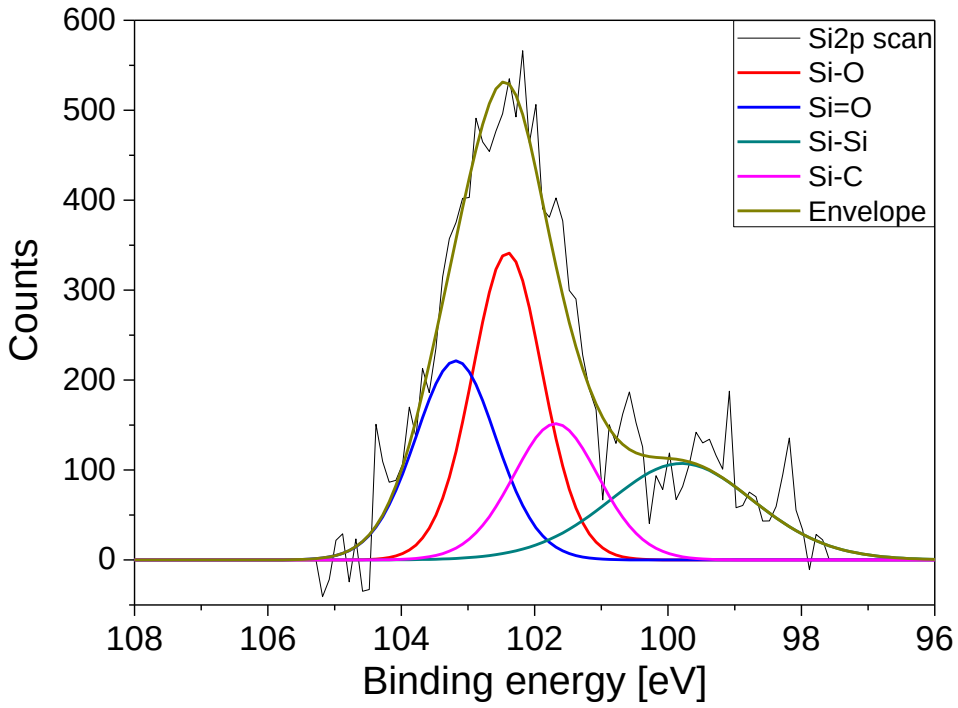

Figure 33 Si2p spectrum of undoped terthiophene capped SiNPs

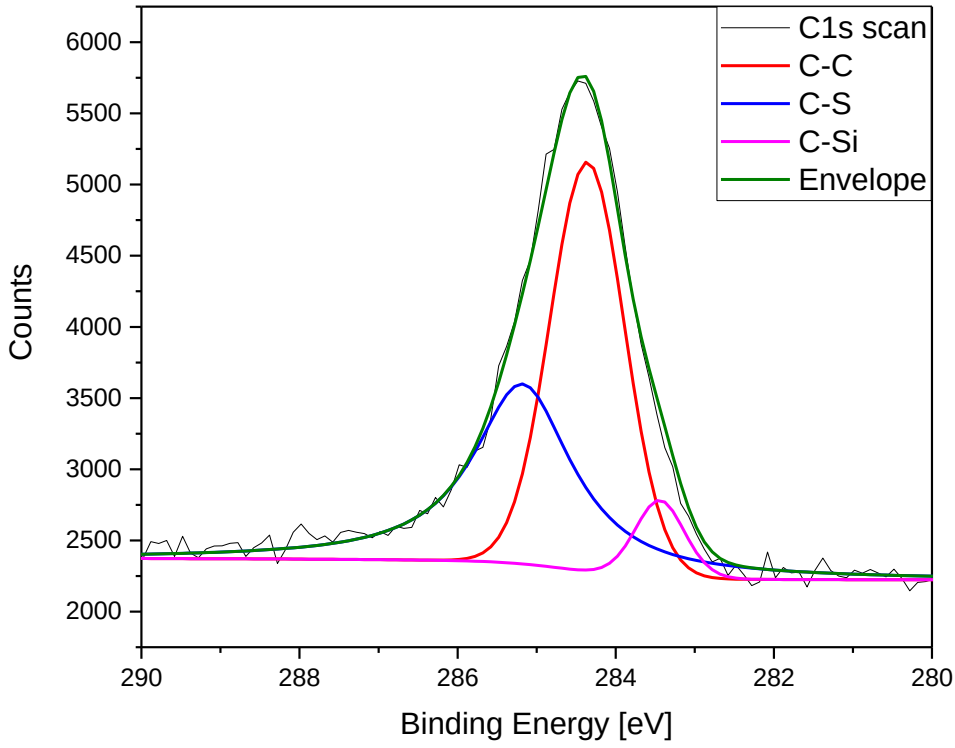

Figure 34 C1s scan spectrum of undoped terthiophene capped SiNPs

Doping of terthiophene is done by adding $NOBF_4$ into sample solution. By oxidising the chains (removing electron) and introducing a BF_4^- counterion to stabilise this, the oligomers on particle surface become more conductive. The material holds the appearance of a fine black powder which can be cold pressed into pellets for further analysis and testing.

EDX data confirmed the presence of the BF4- counter by the presence of a fluorine signal (Figure 35).

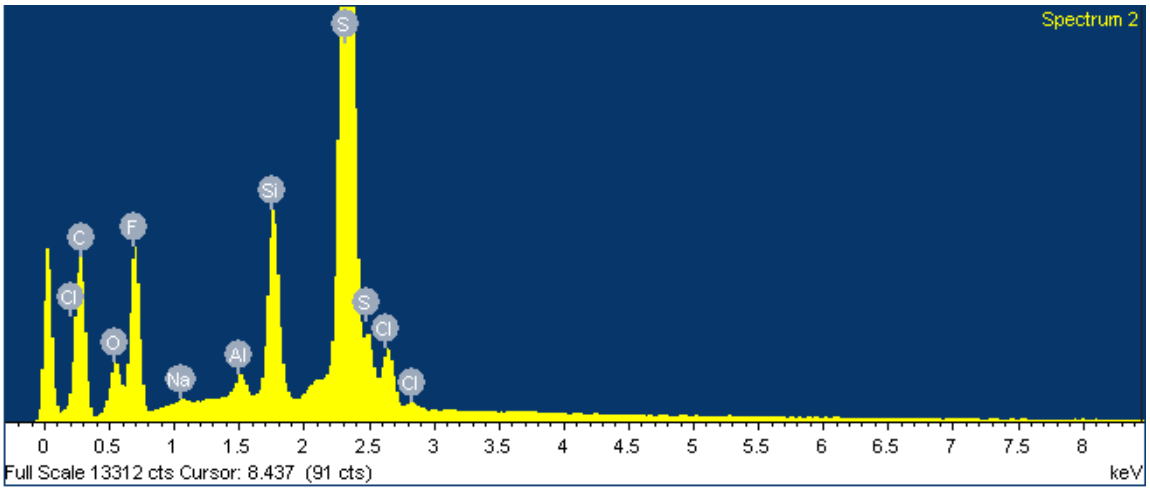

Figure 35 EDX spectrum of doped terthiophene capped SiNPs with $NOBF_4$

XPS spectrum is in concordance with EDX results with a peak of F1s being shown in the survey spectrum. It also gives an increase in O1s signal since the doping process is oxidative.

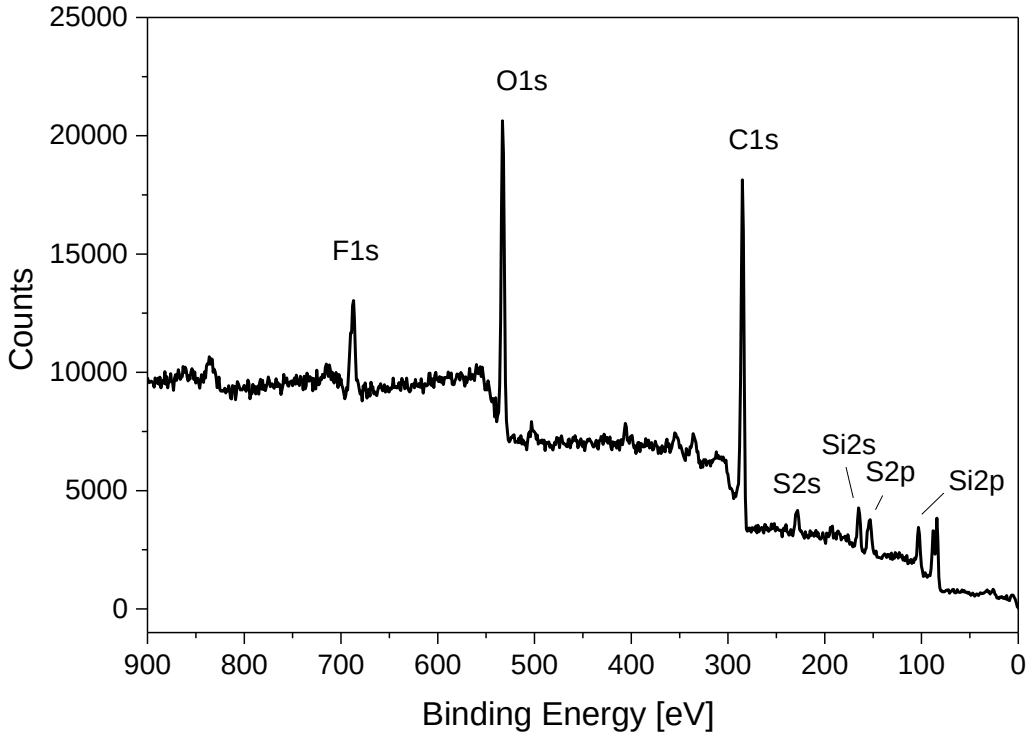

Figure 36 XPS survey spectrum of doped terthiophene capped SiNPs

3.2.1.2 Thermal stability

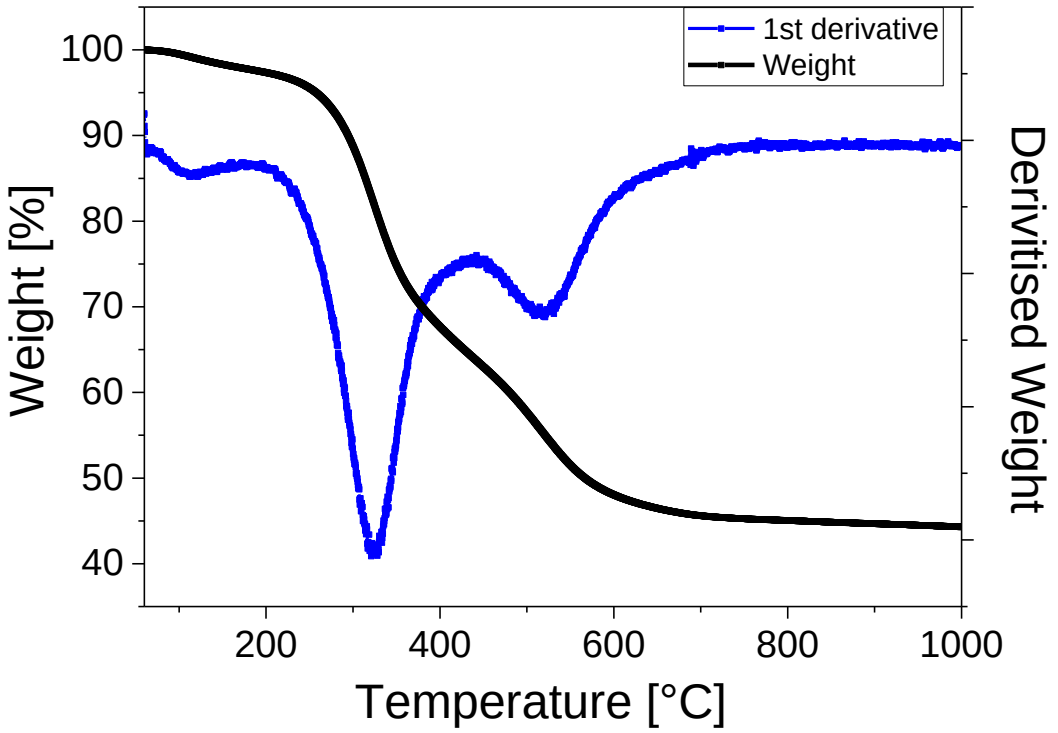

Figure 37 TGA analysis of terthiophene capped SiNPs

TGA shows a weight decrease of over 50% while the temperature is heated up to 1000 °C (Figure 37). The initial weight loss lower than 200 °C is due to the residual naphthalene. After that, two steps of mass drops indicated by the first derivative show a similar process as seen in thiophene capped sample with a larger difference between two types of decomposition. The longer chain of the molecules causes a more dramatic weight drop in the first stage of decomposition. The lower surface coverage provides less Si-C bond to be breakdown during the second stage. DSC result agrees with the two-phase decomposition theory as the two figures shown in Figure 38.

With 55% of the sample mass being terthiophene ligand and 45% being silicon atoms, it could be estimated that the ratio of ligand molecule to silicon atom is 1 to 7. However,

due to XPS data is significant oxidation on the surface of nanoparticle as well, so a more accurate ratio would be higher.

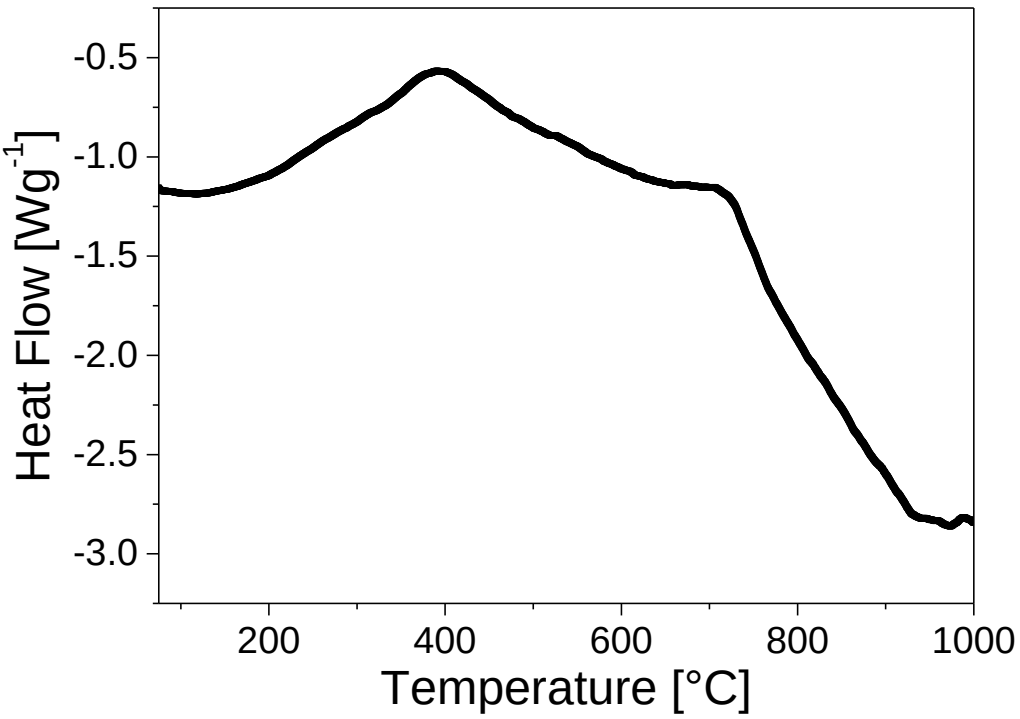

Figure 38 DSC results of terthiophene capped SiNPs

3.2.2. Thermoelectric measurements of terthiophene capped SiNPs

To Produce a more functional thermoelectric material, terthiophene capped SiNPs are doped using $NOBF_4$ and then cold pressed into a pellet for analysis.[11] Electrical conductivity is one essential property which needs to be optimised and doping achieves this by increase charge carrier concentration and mobility.[12-13] In the meantime, high levels of doping could compromise the conductivity as it introduces impurity without any contribution in reducing resistivity.[14-15] As shown in Figure 39, electrical conductivity of the material peaks at doping ratio of 0.4 and then decreases with higher doping level until a certain stage that doping no longer holds an effect on the property.

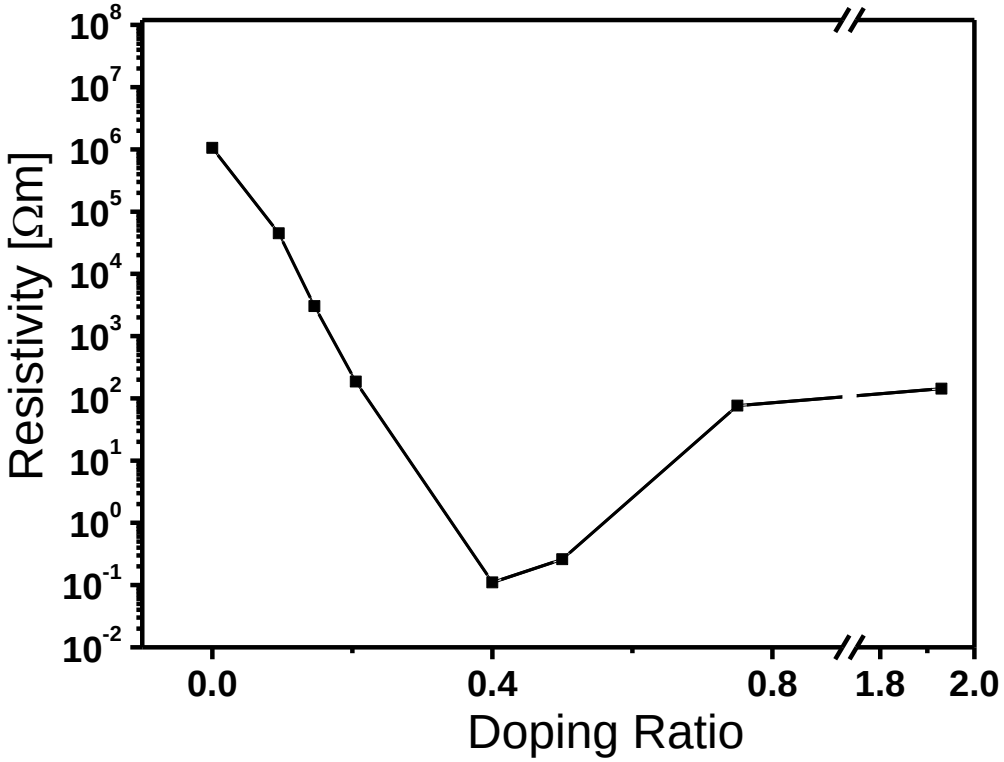

Figure 39 Electrical resistivity of doped terthiophene capped SiNPs

With the optimised doping level discovered based on its electrical conductivity, which is the main challenge for organic semiconductors. Seebeck coefficient is measured based on these chosen samples with ratio from 0.2 to 0.5 to maximize the power factor. As can be seen in Figure 40, Seebeck coefficient of the material has reach a level comparable to insulators rather than common TE materials. This is not a surprise as the optimised conductivity is still not ideal even as a semiconductor and the result stands by the reason we chose silicon as base of the material. As expected, the absolute value of Seebeck coefficient changes in the same way as the resistivity depending on doping ratio. Highest power factor is acquired at doping ratio of 0.5.[16]

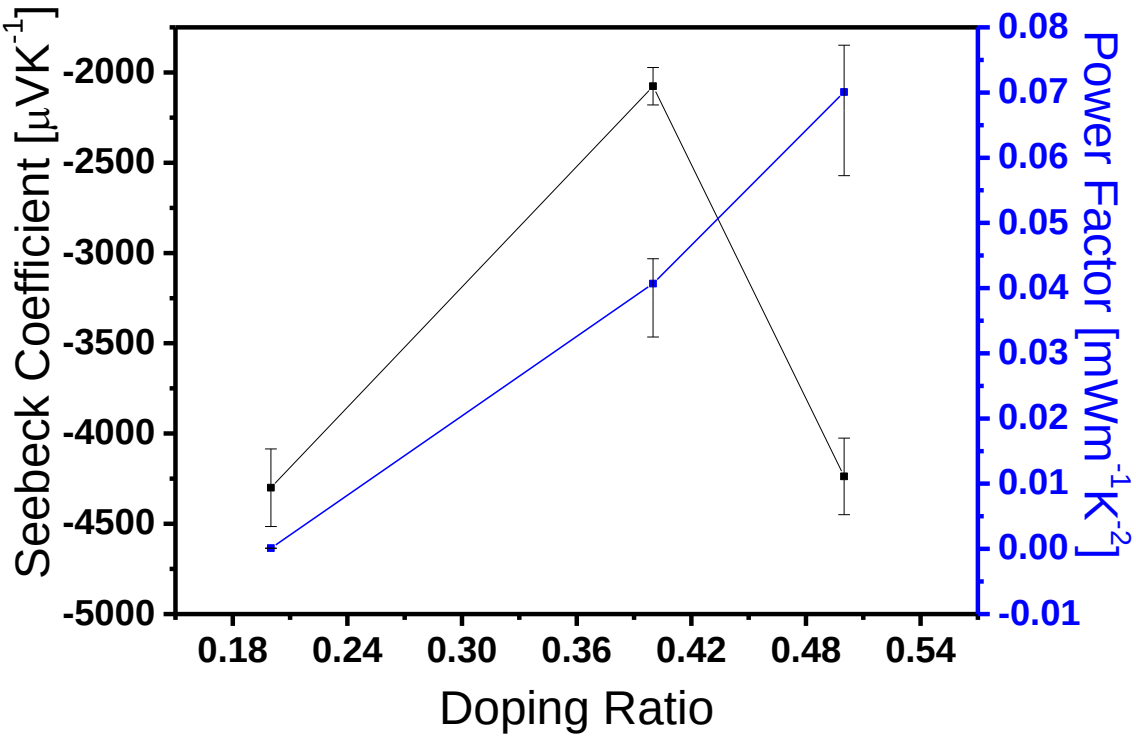

Figure 40 Seebeck coefficient and power factor of doped terthiophene capped SiNPs

Organic polymers have a low thermal conductivity comparing to inorganic materials and this is the reason why terthiophene is chosen as the capping of nanoparticles. As shown in Figure 41, the sample with 0.5 doping ratio is tested for thermal properties and then thermal conductivity is calculated (Figure 42). Terthiophene capped SiNPs possesses a much lower thermal conductivity than common inorganic TE materials as half of the component is conductive polymer and its density is less than half that of bulk silicon.

A higher pressure and slight heating in the pressing process would most likely increase the electrical conductivity as well as the material density.

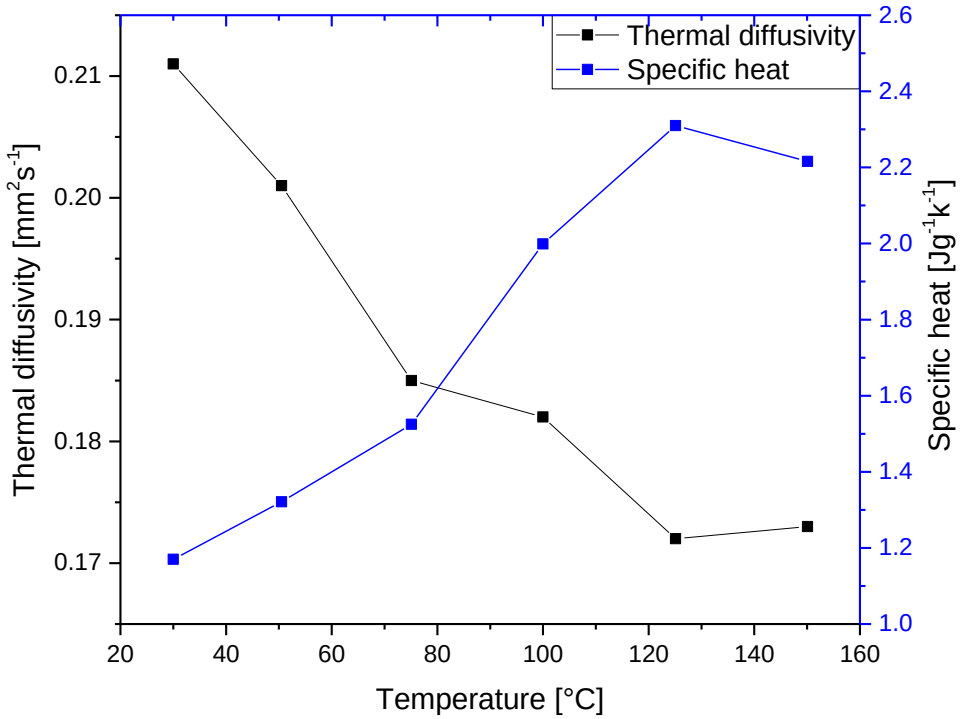

Figure 41 Thermal diffusivity and specific heat capacity of doped terthiophene capped SiNPs

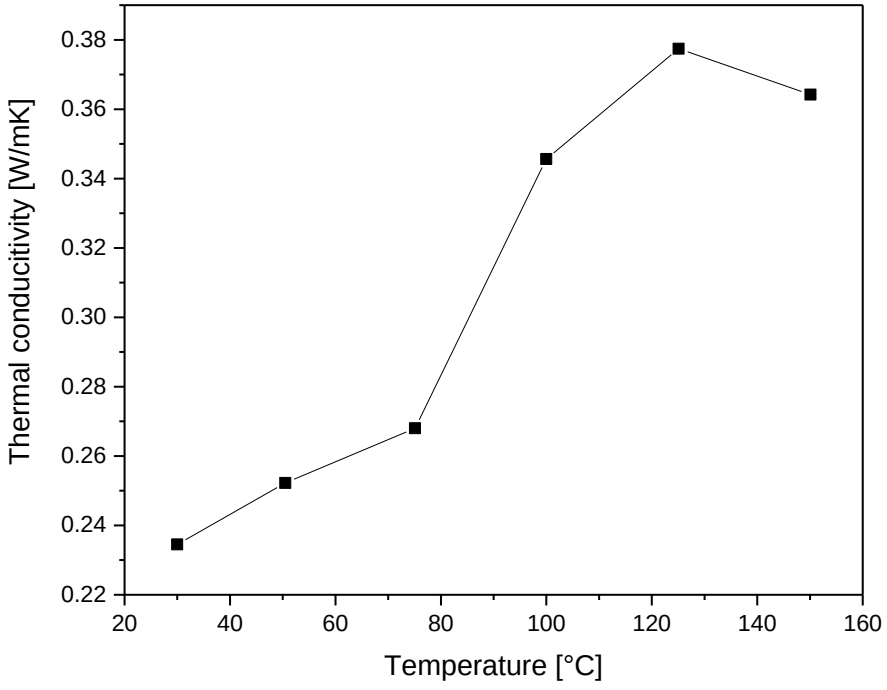

Figure 42 Thermal conductivity of doped terthiophene capped SiNPs

Figure of merit (ZT) of the material against doping level follows the trend of power factor as expected, with a growth against the increasing ratio from 0.2 to 0.5 (Figure 43).

The efficiency as a thermoelectric material is not even close to commercial application. But as a combination of silicon nanoparticle and conductive polymeric material, the material holds a low thermal conductivity and a high absolute value of Seebeck coefficient. And the doping process is proven practical with the subject being inorganic-polymer composite. However, its high electrical resistivity is a major downfall as it also results in the low power factor.

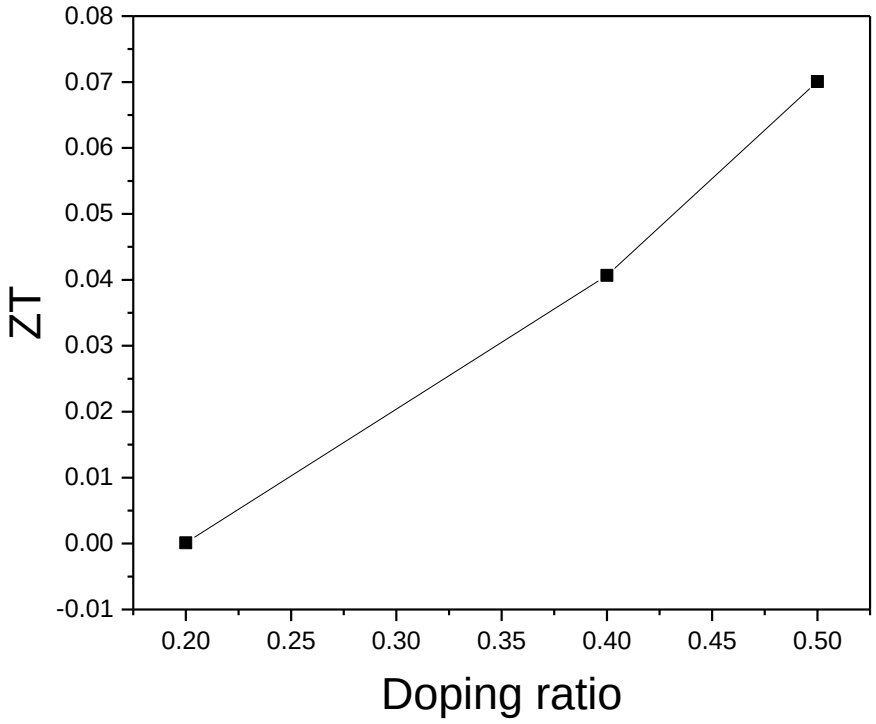

Figure 43 Figure of merit (ZT) of doped terthiophene capped SiNPs

3.3. Discussions

Thiophene capped SiNPs are not an ideal material for use in thermoelectric applications but only the precursor of other materials. It is the first step of employing silicon

nanoparticles into the application as a robust bulk material. With a fine coverage of the nanoparticle surface, the thiophene ligands prevent the oxidation of silicon as well as provide roots for further modification of the organic molecules and structure.

Regarding the state of the nanoparticles, it appears to be dark brown waxy solid, with reasonably high solubility in common organic solvents. These makes the further step of the synthesis of the target materials to be more convenient and with extra options in methods.

Terthiophene capped SiNPs extends the potential of ligand capped nanoparticles as a TE material with an extended oligomer instead of monomer.[4] It also introduces doping process as an essential step when conductive polymer is involved.[14, 17] The addition of organic material provides a much lower thermal conductivity, which is rather essential in the field of inorganic thermoelectric materials.[18]

One of the drawback in synthesis is the decrease in surface coverage, which affect the oxidation level of nanoparticle and more. The still short chain and cold press process is likely to be the reason why it possesses a high resistivity and others as the results of that.[19-20] With power factor related to resistivity in a basic level, the way to decrease resistivity would be a priority for the development in this line of material.

Reference

1. J. Bartuš, *Journal of Macromolecular Science—Chemistry* 28, 917 (1991).

2. P. Chicart, R. J. P. Corriu, J. J. E. Moreau, F. Garnier, and A. Yassar, *Chemistry of Materials* 3, 8 (1991).

3. S. P. Ashby, T. Bian, G. Guélou, A. V. Powell, and Y. Chao, *Journal of Electronic Materials* 45, 1260 (2015).

4. L. Mangolini, E. Thimsen, and U. Kortshagen, *Nano Letters* 5, 655 (2005).

5. R. Pang, X. Hu, S. Zhou, C. Sun, J. Yan, X. Sun, S. Xiao, and P. Chen, *Chem Commun (Camb)* 50, 12493 (2014).

6. K. A. Pettigrew, Q. Liu, P. P. Power, and S. M. Kauzlarich, *Chemistry of Materials* 15, 4005 (2003).

7. G. M. Paterno, V. Robbiano, K. J. Fraser, C. Frost, V. Garcia Sakai, and F. Cacialli, *Sci Rep* 7, 41013 (2017).

8. H. Kawashima, and H. Goto, *Materials* 4, 1013 (2011).

9. Q. Liu, and S. M. Kauzlarich, *Materials Science and Engineering: B* 96, 72 (2002).

10. D. Neiner, H. W. Chiu, and S. M. Kauzlarich, *Journal of the American Chemical Society* 128, 11016 (2006).

11. D. M. Rowe, *CRC handbook of thermoelectrics*. CRC press: 1995.

12. K. Nishiguchi, and S. Oda, *58th DRC. Device Research Conference. Conference Digest (Cat. No.00TH8526)* 5, 79

13. G. H. Kim, L. Shao, K. Zhang, and K. P. Pipe, *Nat Mater* 12, 719 (2013).

14. V. Peulon, G. Barbey, and J. J. Malandain, *Synthetic Metals* 82, 111 (1996).

15. G. Zotti, *Synthetic Metals* 97, 267 (1998).

16. S. L. Ali Shakouri, (1999).

17. C. Yi, A. Wilhite, L. Zhang, R. Hu, S. S. Chuang, J. Zheng, and X. Gong, *ACS Appl Mater Interfaces* 7, 8984 (2015).

18. Y. Du, S. Z. Shen, K. Cai, and P. S. Casey, *Progress in Polymer Science* 37, 820 (2012).

19. M. He, F. Qiu, and Z. Lin, *Energy & Environmental Science* 6, 1352 (2013).

20. J. Wang, K. Cai, and S. Shen, *Organic Electronics* 15, 3087 (2014).

Chapter 4 Polythiophene capped silicon nanoparticles and graphene composite

Polythiophene capping is considered a step forward from oligomer on surface of nanoparticles. Additionally, forming a graphene composite is a universal way of improving electrical conductivity without compromising thermal conductivity in the development of thermoelectric materials.

Contents

The polymerisation of thiophene with the thiophene monomer capped silicon nanoparticles presents a different approach from terthiophene capped SiNPs in the previous chapter, with aiming the same goal in mind: Extending the length of the conductive ligand in order to gain a higher electrical conductivity due to a higher level of overlapping between chains. Meanwhile, this method obtains the much higher surface coverage and the possibility of direct linkage between particles. As mentioned before, polymer provides a low thermal conductivity and sufficient doping would solve the problem of low electrical conductivity during the synthesis. Another advantage from the synthesis is total control of morphology and TE property over the material due to the two-step method.[1] The ratio between polymer, nanoparticles and doping reagent could be easily altered during the synthesis for better performance materials which are more suited to thermoelectric applications.[2]

As for manufacturing a thermoelectric device, polythiophene capped SiNPs still keep the advantages of polymeric materials; being both lightweight and flexibile.[3-5] With the assistance of a substrate,[6] it could fit into all sorts of shapes and thickness.[7] It is suitable for spin coating or inkjet printing as it is dispersible in organic solvent, which is often necessary for the application in room-temperature TE devices.[8]

When exploring the potential of the material and for a comparison with previous materials, cold pressed pellets are also used for analysis of thermoelectric properties. It gives uniformed properties and an indication of how the material performs, as well as eliminating all effects from possible substrate.[2]

Graphene provides a whole new approach in developing thermoelectric materials.[9-10] Its 2-D sheet structure would behave as a template alongside which polythiophene and SiNPs could conjugate.[11-12] Due to it flat structure, the electrical and thermal properties

are anisotropic.[13] Its high electrical conductivity would directly boost the performance of the material as a whole,[14] and more so if the direction is aligned in the plane of the aromatic system.[15] Its high thermal conductivity could be an issue, but with the right amount and type of doping, the thermal conductivity of the material could be reduced by scattering phonon more efficiently.

4.1. Polythiophene capped SiNPs

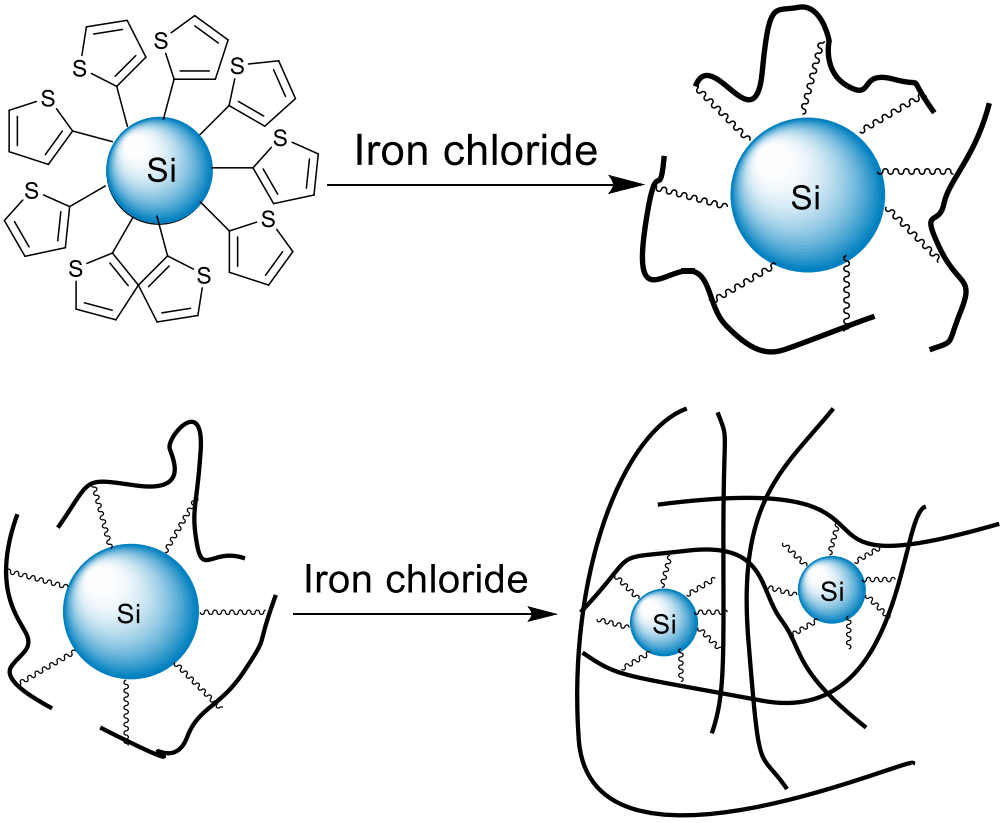

Scheme 10 Synthesis of polythiophene capped SiNPs

The scheme above (Scheme 10) shows the ideal process of the polymerisation of thiophene and thiophene capped SiNPs. Although not two steps in practice, this synthetic method uses polymer to wrap up the nanoparticles with polythiophene chains including by both the thiophene monomers and the thiophene ligands attached to SiNPs. This is confirmed by TEM images in Figure 46.

4.1.1. Size characterisation and elemental analysis

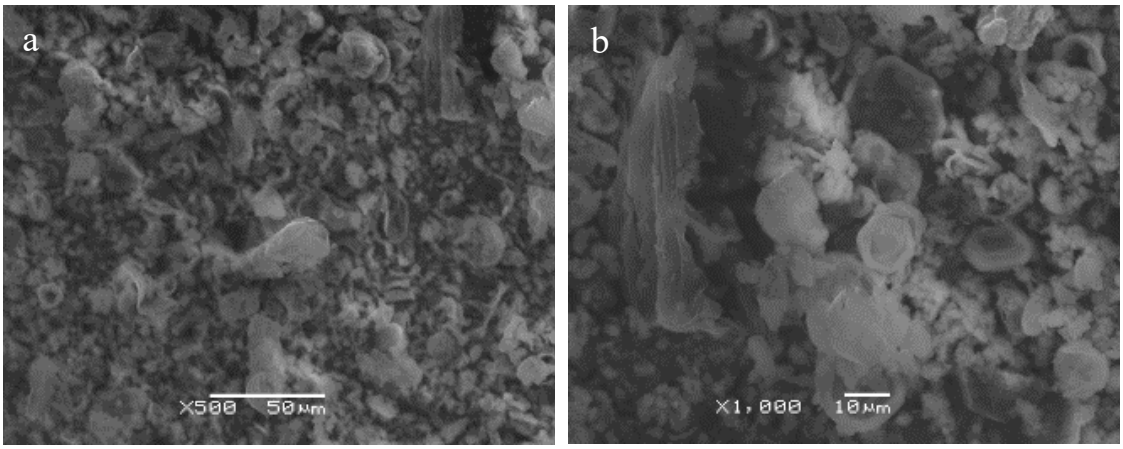

Figure 44 SEM of polythiophene capped SiNPs

SEM images show the layered structure of the polymeric material (Figure 44). The polythiophene localises around a centre to form a round structure. This film-like structure of polythiophene constructs the surrounding and surface layer of the material. There are also liner-shaped films shown in these images, which could be extra polymer formed without the influence of nanoparticles.

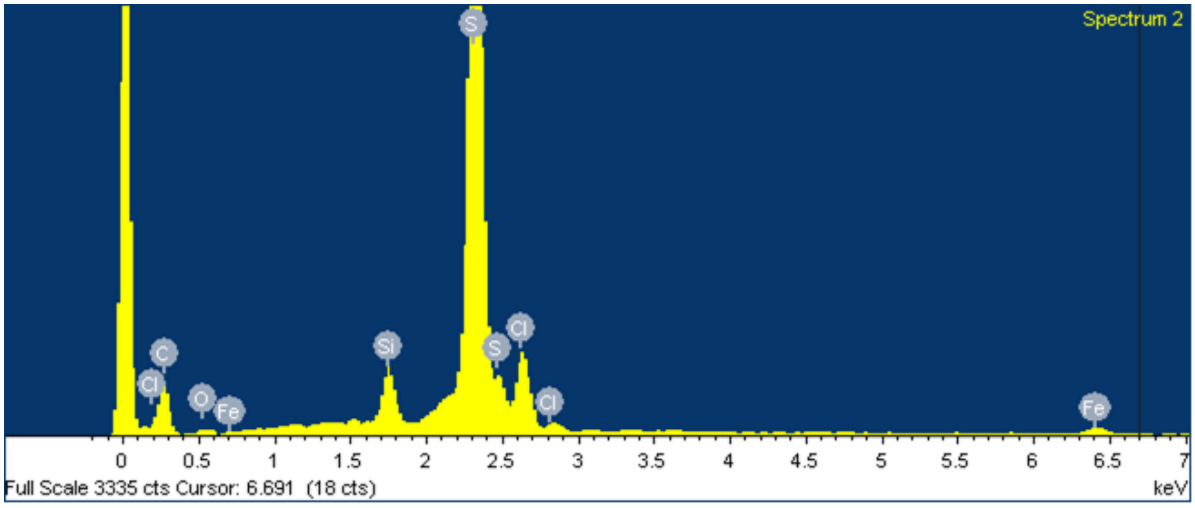

Figure 45 SEM-EDX of polythiophene capped SiNPs

EDX analysis in Figure 45 shows the elemental composition of the product. Carbon, sulphur and silicon are expected to make up most of the sample. Additionally, there are chlorine, which is behaving as counterion and some iron.

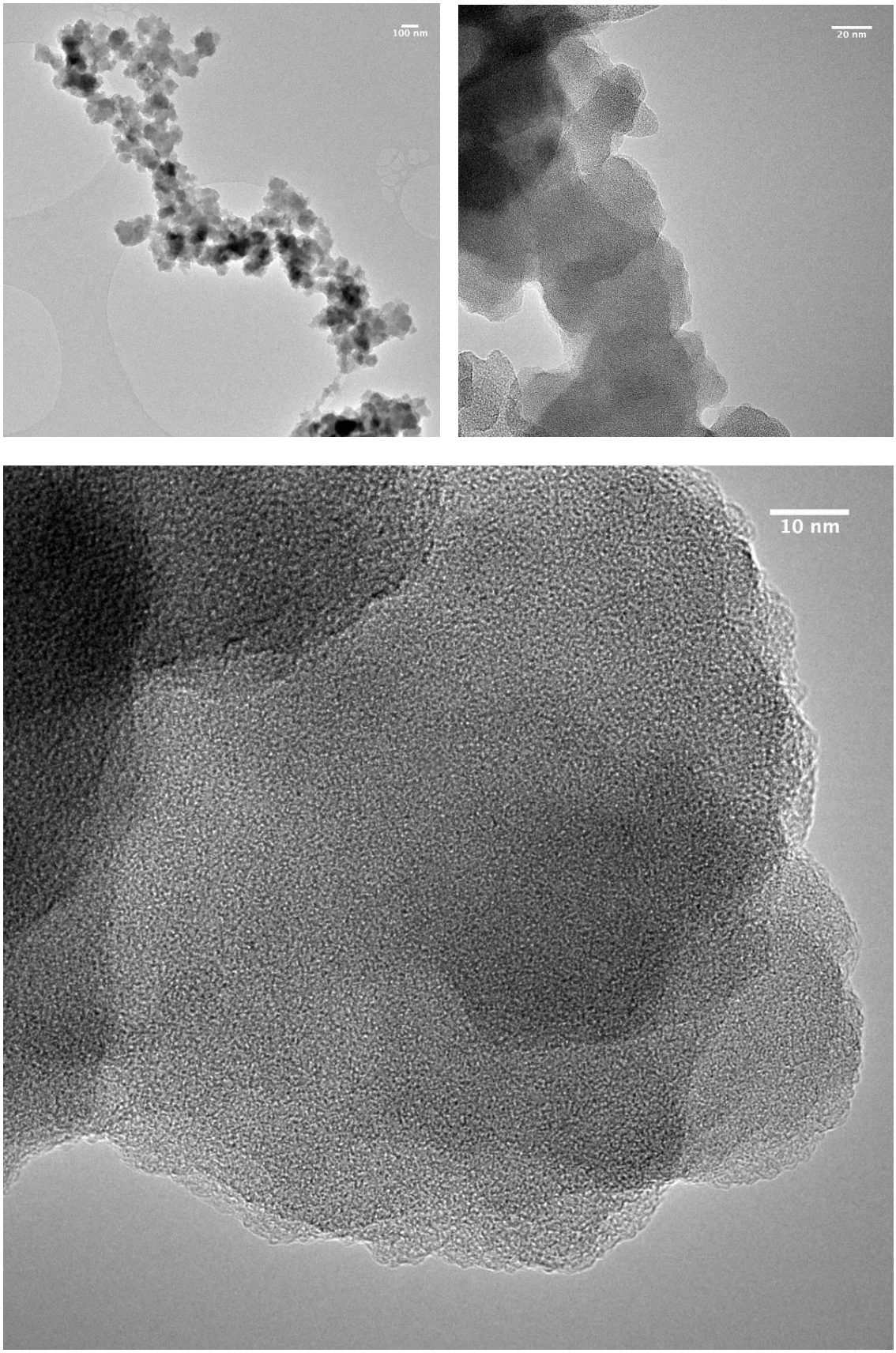

Figure 46 TEM of polythiophene capped SiNPs

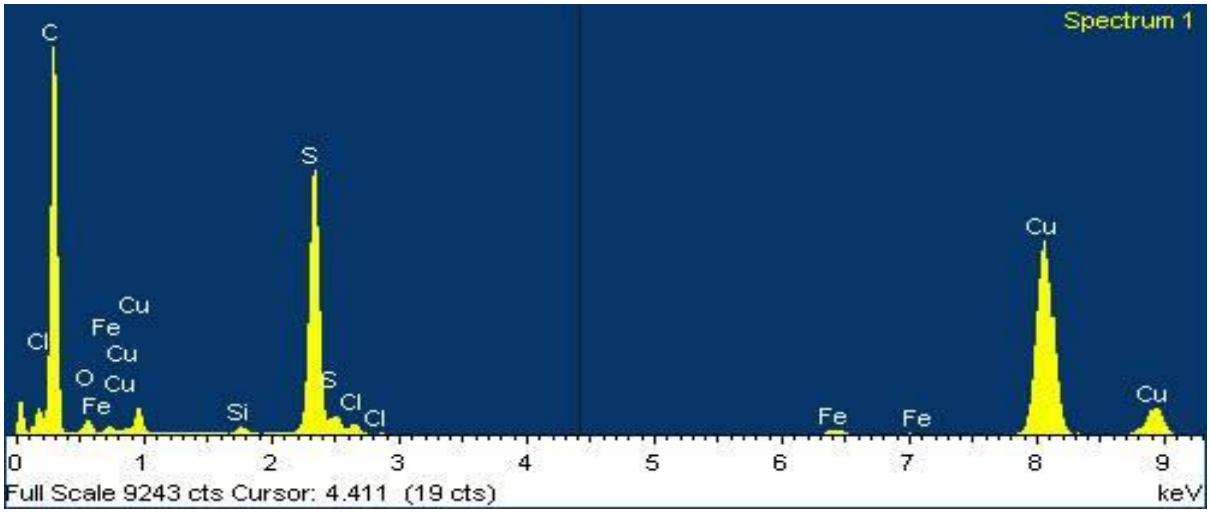

Figure 47 TEM-EDX of polythiophene capped SiNPs

From TEM image shown in Figure 46, particles are seen buried inside the polythiophene and the connections between each other are tight. They form into large clusters and this is proof of the existence of polymer network. EDX in Figure 47 confirms that there is sufficient amount of silicon inside the material even in this scattered state.

4.1.2. Thermoelectric results

Doping level	0.5	0.6	0.8
Seebeck coefficient [μV/K]	-229677.86378	-170197.01803	-175813.07711
Thermal conductivity [W/(mK)]	0.09412	0.16872	0.08676
Electrical conductivity [S/m]	1.6111×10^{-5}	1.1904×10^{-4}	1.3445×10^{-5}
Power factor [μW/(mK2)]	0.84992	3.44846	0.4156
Figure of merit ZT	0.00274	0.00619	0.00145

Table 1 Thermoelectric measurement changes of $NOBF_4$ Doped Polythiophene capped SiNPs depending on the doping ratio

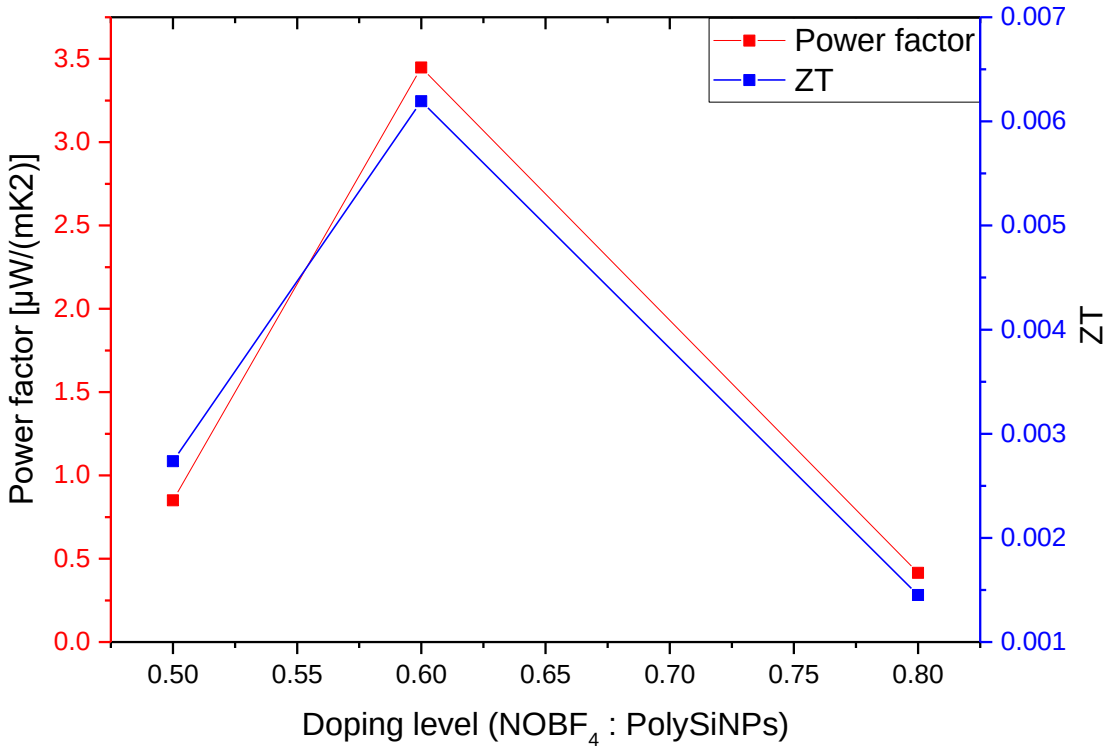

Figure 48 Thermoelectric performance change of $NOBF_4$ Doped Polythiophene capped SiNPs depending on the doping ratio

The thermoelectric performance peaked when the doping level is at 0.6, which is similar to terthiophene capped SiNPs in last chapter. However, the overall performance is not as good. The polythiophene capped sample holds a poor charge carrier concentration, which leads to a low electrical conductivity and high Seebeck coefficient. As a result, the calculated power factor is low comparing to terthiophene capped materials. This could be due to the polymer in the sample not being a uniformed as terthiophene. These intertwined polymer chains may act as an obstacle against $NOBF_4$ doping and electron transport. Thermal conductivity of the material is lower than terthiophene capped SiNPs which can be explained by the better surface coverage and the multi-layer wrapping of the polythiophene around the SiNPs nanoparticles.

4.2. Polythiophene capped SiNPs - graphene composite

Polythiophene capped SiNPs show some potential as a thermoelectric material. However, its low electrical conductivity holds the thermoelectric performance down. Therefore, a new approach is introduced. With the proven SPS technique, PT capped SiNPs are mixed with graphene and then pressed into dense pellets.[16]

4.2.1. Structural and elemental analysis

Pellets were break down into pieces so that one could look into the inner structure rather than the smooth surface, in order to get a more accurate analysis of the microstructure and composition.

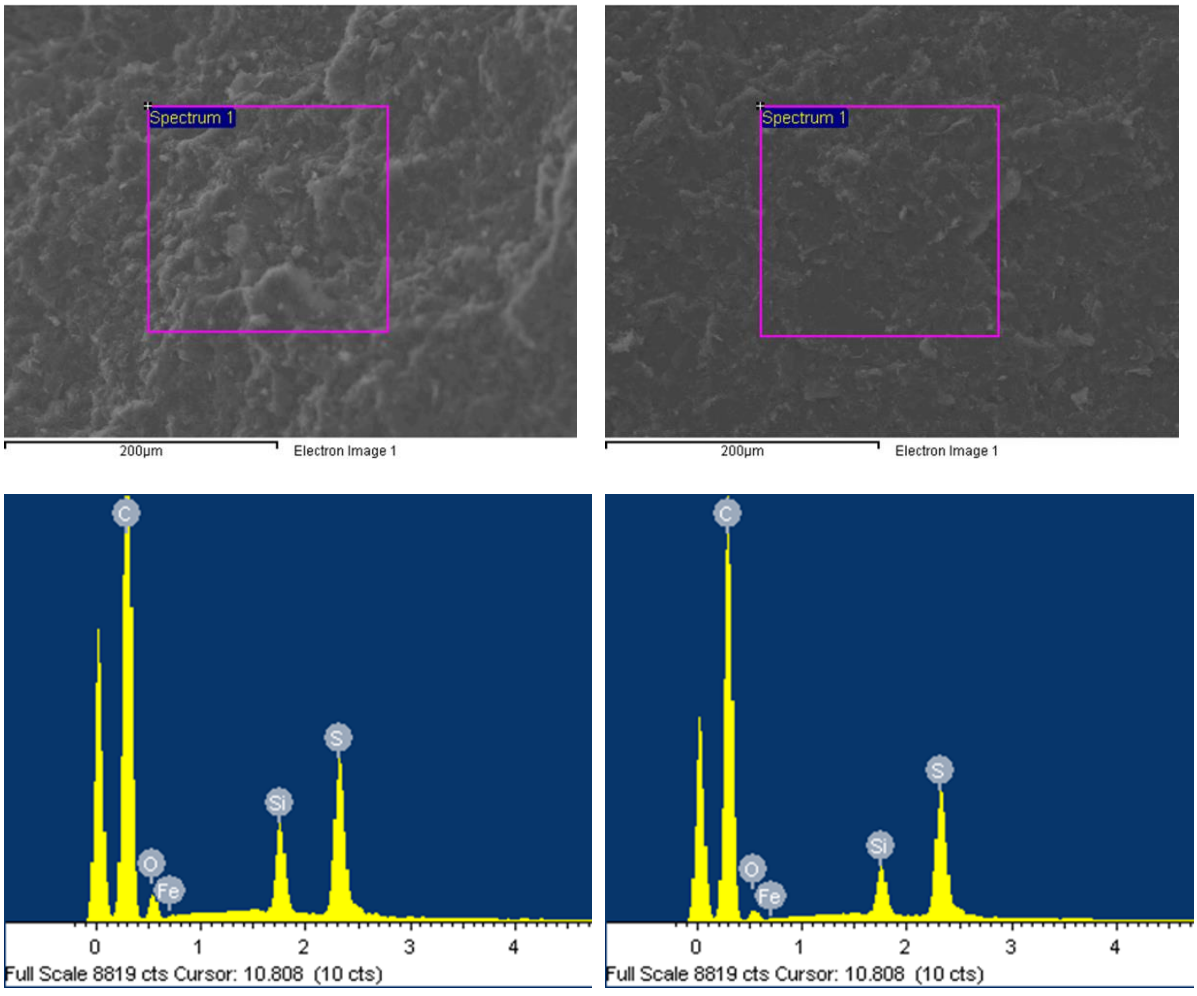

Figure 49 SEM-EDX of SiNPs-Graphene composite

The composite still obtains a layered structure as the polythiophene capped SiNPs. However, the graphene template has a strong influence in the construction of the layers. Unlike the circles in the sample before, this composite sample shows a much finer structure without any clear shape in the images obtained. The SPS process contributes highly in the resulting structure as well, with its high pressure.

4.2.2. Compositional and structural analysis

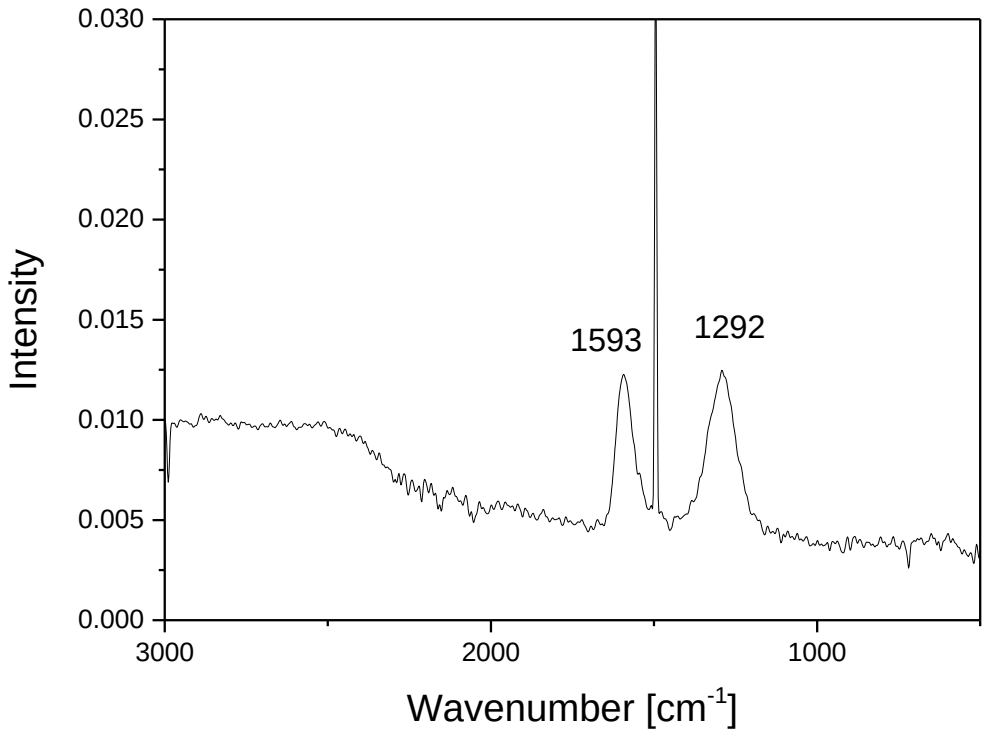

Figure 50 Raman spectrum of synthesized graphene

In Figure 50, two peaks are seen clearly at 1593 and 1292 cm^{-1} representing G-band and D-band respectively. With D-band signal stronger than G-band, it is proven that reduced graphene oxide as in graphene is manufactured via the chosen method.[17] Single sharp peak in 1500 cm^{-1} is due to the instrument and has nothing to do with the sample.

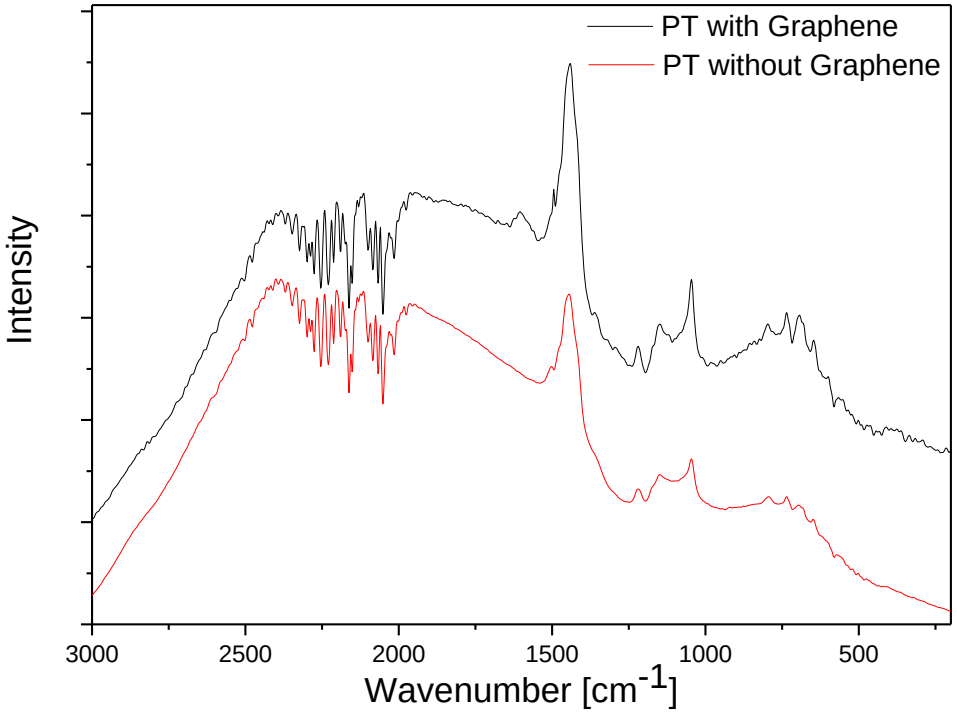

Figure 51 Raman spectra comparing sample before and after the doping of graphene

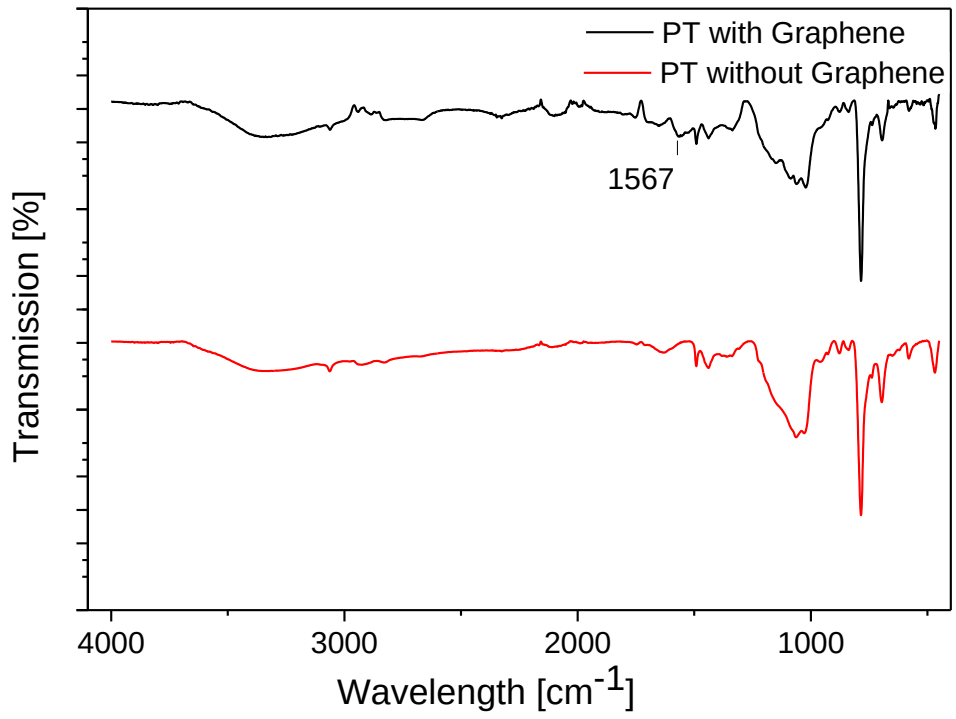

Figure 52 FTIR spectra comparing sample before and after doping with graphene

Raman and FTIR spectra give a comparison of the sample before and after mixing in graphene. In Raman spectrum, the signal of G-band at 1600 cm^{-1} can be observed only when graphene is added. Other than that, all peaks are identical including signature peaks of polythiophene at 1440, 1220 and 1045 cm^{-1}.[18]

In FTIR spectra, the signal in 1567 cm^{-1} shows a significate change relates to the aromatic carbon double bond, indicating the existence of graphene (top). The peak located in 3060 cm^{-1} is related to aromatic C-H bond, and it stays the same after the mixing of graphene as the reduction of graphene oxide is completed without noticeable defects. Other peaks are almost identical with no other ingredients in difference. Both silicon-carbon bond and sulphur-carbon bond are kept intact with signals at 1439 cm^{-1} and 786 cm^{-1}, respectively.

4.2.3. Thermoelectric measurements

Doping level	0	0.2	0.4	0.6	0.8
Seebeck coefficient [μV/K]	13.86	-9.84	-12.8	-14.53	-16.05
Thermal conductivity [W/(mK)]	0.0511	0.1787	0.2009	0.0642	0.1245
Electrical conductivity [S/m]	8.138×10^{-4}	3.915×10^{-3}	5.665×10^{-3}	8.169×10^{-3}	1.028×10^{-2}
Power factor [μW/(mK2)]	0.156	0.379	0.928	1.725	2.648
Figure of merit ZT	0.0024	0.0016	0.0036	0.022	0.016

Table 2 Thermoelectric measurement changes of Polythiophene capped SiNPs - Graphene composite depending on the mixing ratio

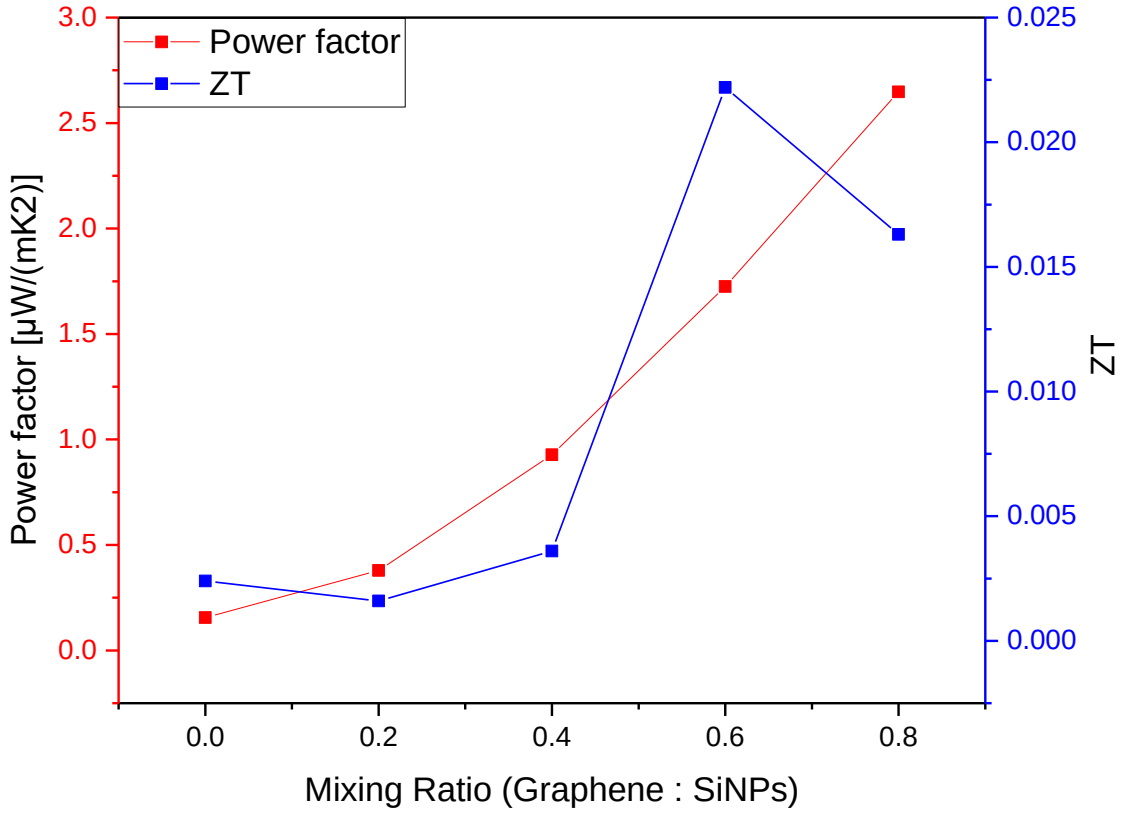

Figure 53 Thermoelectric performance change of Polythiophene capped SiNPs - Graphene composite depending on the mixing ratio

Table 2 and Figure 53 show the change in thermoelectric properties of the composite material with the increasing ratio of graphene.

Thermal conductivity is affected by graphene but not significantly even with the dopant possessing one of the highest thermal conductivity. As discussed in Chapter one, graphene is not behaving as the phonon transporter. On the contrary, the dopant scatters phonons from crystalline structure boundaries to stop the transfer between nanoscale structures within the material.

Seebeck coefficient shows a unique trend as it changes from positive to negative with absolute value increasing alongside the growing ratio of graphene. This is easily explained as graphene brings in considerable number of free electrons into the system.

Electrical conductivity is largely increased by the level graphene dopant as it not only introduces more charge carriers but also increase in matter that carry charges. As a result, power factor of the material shows a continuous increase with the climbing ratio of graphene in the mixture.

The highest figure of merit value comes at 0.6 ratio of graphene as a consequence of the fluctuating thermal conductivity.

4.3. Discussion and future work

Polythiophene capped SiNPs shows the potential of a higher Seebeck coefficient in polymeric materials with the help of mixing silicon nanoparticles. However, the cold pressed pellet procedure shows limitations in providing sufficient contact between polymer chains for the charge carriers to mobilize. The doping by oxidation is proven functional in the field of synthesizing polymer based thermoelectric material.

When it comes to a graphene composite with polythiophene capped SiNPs, the situation is reversed. With a relatively high electrical conductivity and very low thermal conductivity compared to inorganic material, the only downside being its low Seebeck coefficient Seebeck coefficient, which in turn results in a low power factor. The value is in a way comparable to that of metals. The reason comes from the way the carrier concentration is modified. With the goal of increasing electrical conductivity without compromising thermal conductivity, graphene is added into the composite, which is a metal like material. However, the lack of doping in the entire material fabrication possibly results in opposing Seebeck effects induced by both positive and negative charge carriers. This in turn leads to a decrease in Seebeck coefficient. The next step of modifying this material would be via controlling the doping so that only one type of charge carriers will be able to move freely.

Reference

1. S. H. Lee, Y. S. Kim, and J. H. Kim, *Journal of Electronic Materials* 43, 3276 (2014).

2. O. Bubnova, and X. Crispin, *Energy & Environmental Science* 5, 9345 (2012).

3. N. Dubey, and M. Leclerc, *Journal of Polymer Science Part B: Polymer Physics* 49, 467 (2011).

4. M. He, F. Qiu, and Z. Lin, *Energy & Environmental Science* 6, 1352 (2013).

5. M. A. Kamarudin, S. R. Sahamir, R. S. Datta, B. D. Long, M. F. Mohd Sabri, and S. Mohd Said, *TheScientificWorldJournal* 2013, 713640 (2013).

6. S. J. Kim, J. H. We, and B. J. Cho, *Energy & Environmental Science* 7, 1959 (2014).

7. K.-C. Chang, M.-S. Jeng, C.-C. Yang, Y.-W. Chou, S.-K. Wu, M. A. Thomas, and Y.-C. Peng, *Journal of Electronic Materials* 38, 1182 (2009).

8. O. Bubnova, Z. U. Khan, A. Malti, S. Braun, M. Fahlman, M. Berggren, and X. Crispin, *Nature materials* 10, 429 (2011).

9. O. Bubnova, Z. U. Khan, H. Wang, S. Braun, D. R. Evans, M. Fabretto, P. Hojati-Talemi, D. Dagnelund, J. B. Arlin, Y. H. Geerts, S. Desbief, D. W. Breiby, J. W. Andreasen, R. Lazzaroni, W. M. Chen, I. Zozoulenko, M. Fahlman, P. J. Murphy, M. Berggren, and X. Crispin, *Nat Mater* 13, 190 (2014).

10. R. Lundgren, P. Laurell, and G. A. Fiete, *Physical Review B* 90, 165115 (2014).

11. L. Wang, Q. Yao, H. Bi, F. Huang, Q. Wang, and L. Chen, *Journal of Materials Chemistry A* 2, 11107 (2014).

12. K. Xu, G. Chen, and D. Qiu, *Journal of Materials Chemistry A* 1, 12395 (2013).

13. Y. Xu, Z. Li, and W. Duan, *Small* 10, 2182 (2014).

14. D. Yoo, J. Kim, S. H. Lee, W. Cho, H. H. Choi, F. S. Kim, and J. H. Kim, *J. Mater. Chem. A* 3, 6526 (2015).

15. M. O. Ansari, M. M. Khan, S. A. Ansari, I. Amal, J. Lee, and M. H. Cho, *Chemical Engineering Journal* 242, 155 (2014).

16. S. P. Ashby, T. Bian, H. Ning, M. J. Reece, and Y. Chao, *Journal of Electronic Materials* 44, 1931 (2015).

17. S. Perumbilavil, P. Sankar, T. Priya Rose, and R. Philip, *Applied Physics Letters* 107, 051104 (2015).

18. G. Shi, J. Xu, and M. Fu, *Journal of Physical Chemistry B* 106, 288 (2002).

Chapter 5 Exploring microscopic conductivity of capped SiNPs via Muon spin spectroscopy

Avoided level crossing muon spin resonance (ALC-μSR) spectroscopy and Transverse field muon spin rotation (TF- μSR) spectroscopy are powerful methods to investigate the microscopic electrical conductivity of phenylacetylene capped silicon nanoparticles (SiNPs). A model molecule called tetrakis (2-phenylethynyl) silane containing four phenylacetylene ligands attaching to a single silicon atom was synthesised to imitate the surface of nanoparticle both in experiment and computational simulation.

Contents

5.1. Introduction

ALC-μSR spectroscopy explores hyperfine coupling constant (hfcc) of nuclei other than muon.[1] The Δ_0 resonance, in specific, is caused by the interaction between muon and nuclear states when spinning in opposite directions. These resonances are seen in muoniated radicals within samples of all types of states.[2]

The Δ_0 resonance is fitted to a Lorentzian formula, in which the relaxation rate can be computed from the full width at half maximum. In turn, the reaction rate of a muoniated radical can be determined.[3]

TF-μSR spectroscopy gives a direct measurement of the hyperfine coupling with the correlation of signals in a given external magnetic field. Since the observed frequencies are related to applied field and hyperfine constant, the correlation function would extract the radical signals from the spectrum.[4-6]

5.2. Characterization of samples

As described in previous chapters in details, both samples were synthesized by solution based lithiation.

5.2.1. Model molecule [tetrakis(phenylethynyl)silane]

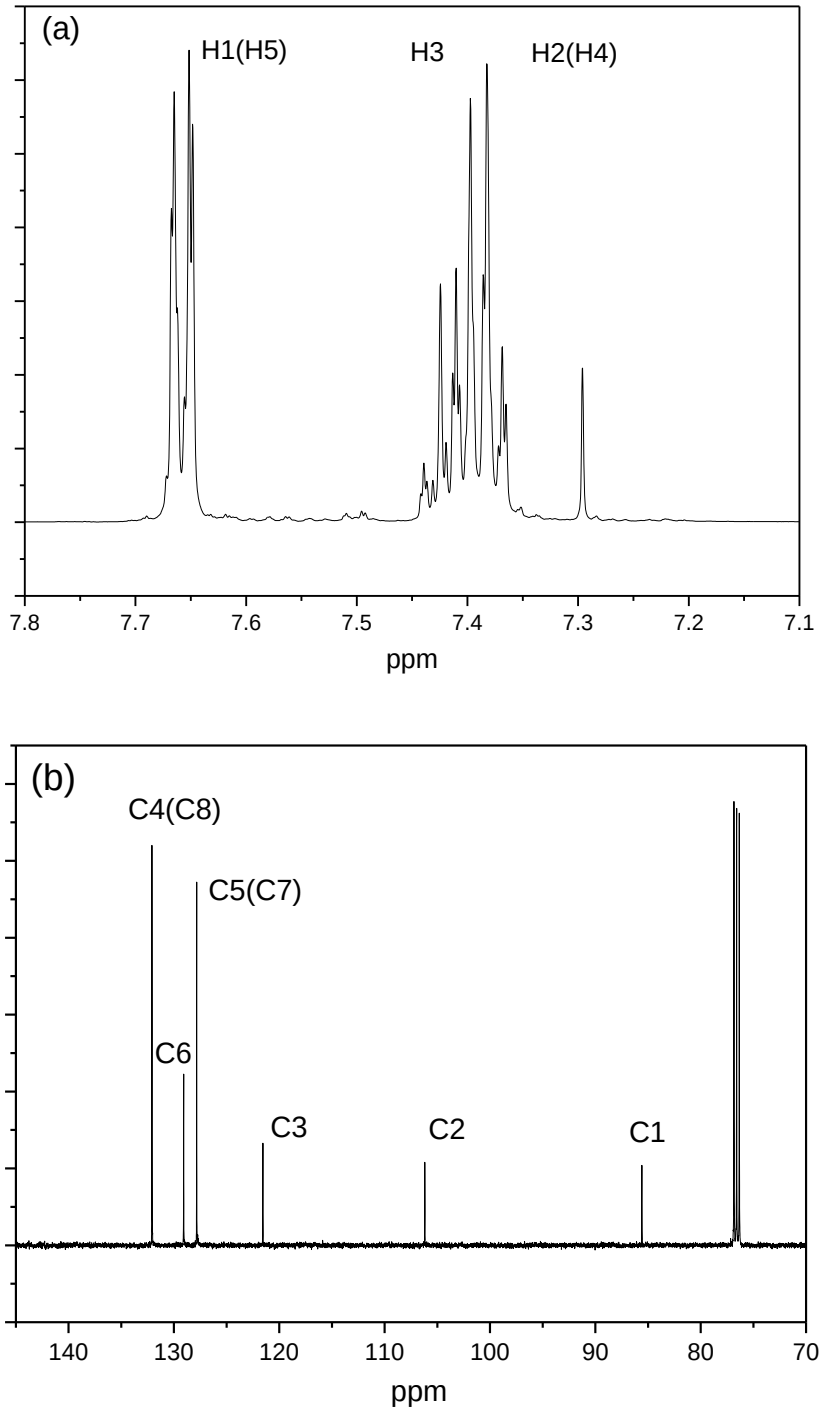

Figure 54 NMR results of tetrakis (2-phenylethynyl) silane

NMR spectra of tetrakis (2-phenylethynyl) silane molecule (Figure 1) show expected results. Three multiplet peaks can be observed in ^{1}H-NMR at 7.66, 7.41 and 7.39 ppm,

respectively, indicating three hydrogen atoms with different environments. Individual atoms are labelled in Figure 54 (a). Six peaks are found in the ^{13}C-NMR at 132.08, 129.07, 127.84, 121.55, 106.18, and 85.59 ppm, respectively, as shown in Figure 54 (b), which are consistent with six different carbon atoms within the molecule.

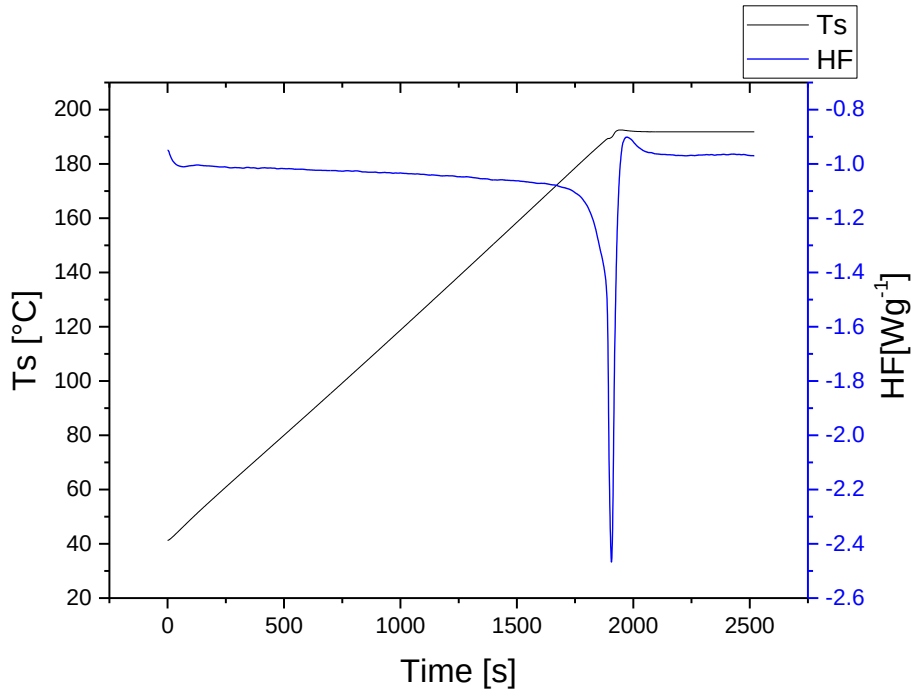

Figure 55 DSC results of tetrakis (2-phenylethynyl) silane

DSC result of the model molecule shows a sharp peak at 1900 s, indicating a melting point of 190 °C. The sharpness of the peak is also an indication of the sample purity.

5.2.2. Phenylacetylene capped silicon nanoparticle

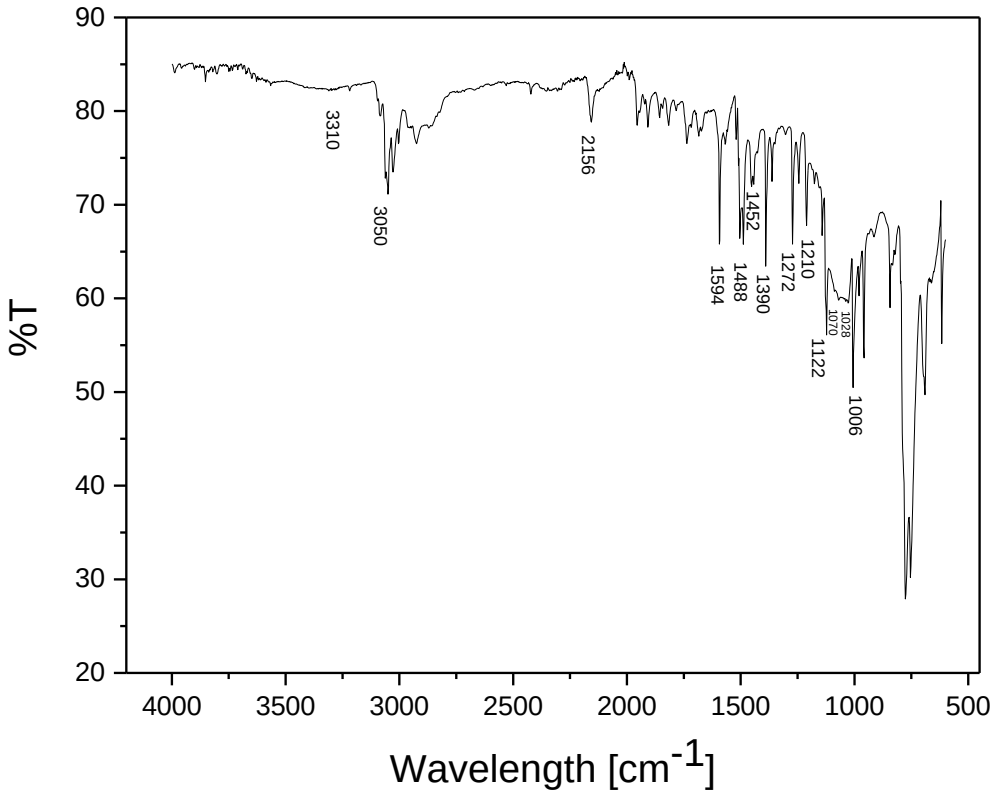

Figure 56 FTIR of Phenylacetylene capped SiNPs

Figure 56 shows the FTIR spectrum of phenylacetylene capped SiNPs. The peak at 2156 cm^{-1} along with the absence of peak in 3310 cm^{-1} indicates the carbon triple bond attaching directly to silicon atom. The existence Si-C bond is also proven by peaks at 1452 cm^{-1} and 1210 cm^{-1}. The 3050 cm^{-1} peak is an indication for aromatic C-H bond. Peaks at 1594 cm^{-1} and 1488 cm^{-1} are both representative of aromatic C-C bond.

5.3. Computational simulation

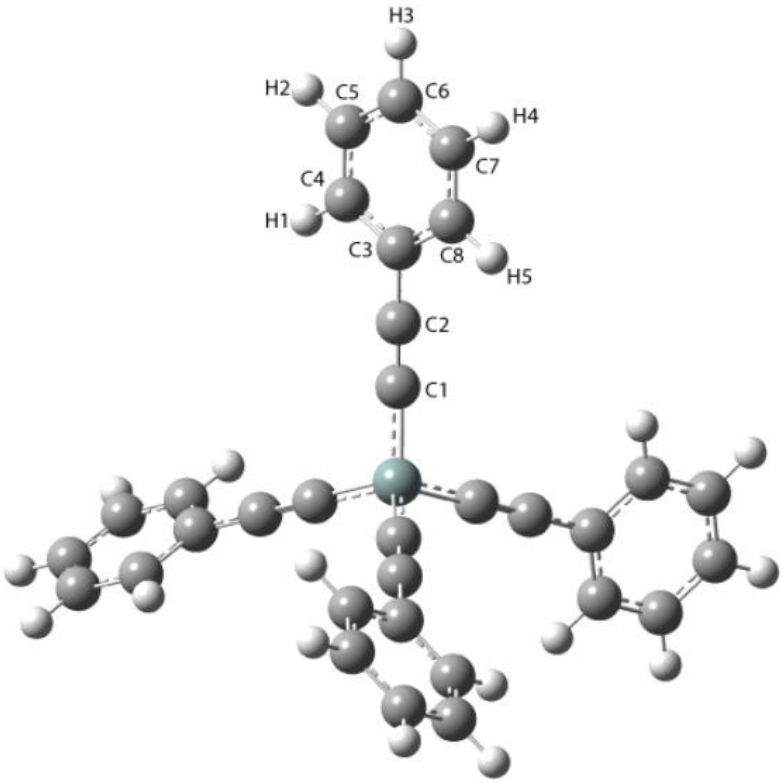

Radical	$A_{e\mu}$(MHz)	$\Delta_1 B_{res}$ (T)	$\Delta_0 H_1$ (T)	$\Delta_0 H_2$ (T)	$\Delta_0 H_3$ (T)	$\Delta_0 H_4$ (T)	$\Delta_0 H_5$ (T)
C_1–Mu	335.71	1.2643	1.7844	2.0118	1.7976	1.9720	1.2598
C_2–Mu	404.38	1.4495	2.3117	2.0583	2.2720	1.4433	2.2695
C_3–Mu	347.07	1.1615	1.6486	1.8172	1.1605	1.8172	1.6486
C_4–Mu	327.30	1.4565	2.2799	1.4557	2.2819	2.0685	2.3219
C_5–Mu	396.63	1.2019	1.1975	1.9202	1.6787	1.9603	1.6628
C_6–Mu	316.30	1.2745	2.0143	1.8026	2.0552	1.8026	2.0143
C_7–Mu	394.73	1.4850	2.1643	2.1665	2.1614	2.1662	2.1602
C_8–Mu	344.28	1.2328	1.8829	1.7638	1.8914	1.7639	1.8829

Table 3 Computational simulation and DFT calculation results

Computational simulation is operated with the model molecule as the subject. Due to the target area explored was the surface of the nanoparticles, this molecule can be used to mimics the reaction that happens there without involving too many atoms in the simulation.

Table 2 shows results from the *ab initio* density functional theory (DFT) simulations of the hyperfine parameters.[7] This computational work is done by Jamie Peck and published with myself as first author.[8]

This set of results gives all possibilities when a muon attaches to a carbon atom and then having a spin interaction with a hydrogen atom in the same phenylacetylene molecule. It gives both Δ_1 and Δ_0 positions from the reaction and Δ_0 is what we are focusing on during the experiments.[9-10]

The simulation gives a certain range of external magnetic field that should be investigated during the experiments and an estimated position assignment for each site. This estimation gives an idea of which atom the muon is attaching to and in turns helps deduce how the electron cloud is distributed.

There are certain similarities in the simulating results when two hydrogen atoms share the same chemical environment.

5.4. Spectroscopy

5.4.1. Solid state spectroscopy

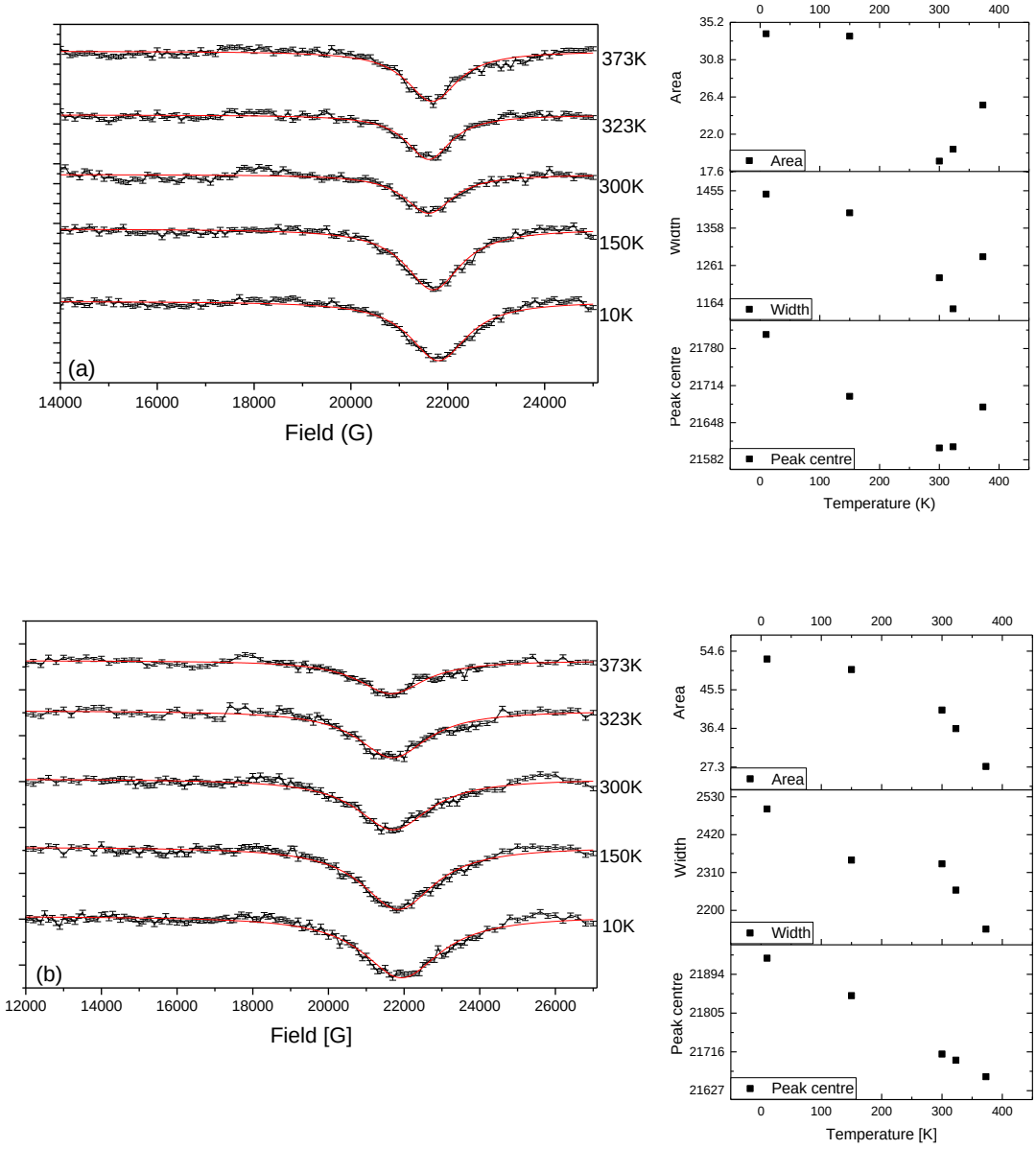

Figure 57 Solid state ALC spectra (a. molecule, b. SiNPs)

Shown in Figure 57 are ALC spectra of solid state model molecule (a) and nanoparticles (b). On the right side, a summary of the spectrum specified the figures depending on temperature change.

Both samples were scanned in five different temperatures below melting point of molecule.

Both molecule and nanoparticle sample give ALC resonance at around 2.2 T. With the temperature decreasing, the peak is getting higher and broader. Both area and width of the peak are decreasing with rising temperature, as well as the main peak is shifting to the lower position.

In the meantime, nanoparticle sample gives higher and broader peaks than molecule.

Molecule sample in high temperature gives a different trend with the peak getting higher when temperature increases. In the meantime, the peak at 373 K shows a special asymmetry towards higher field.

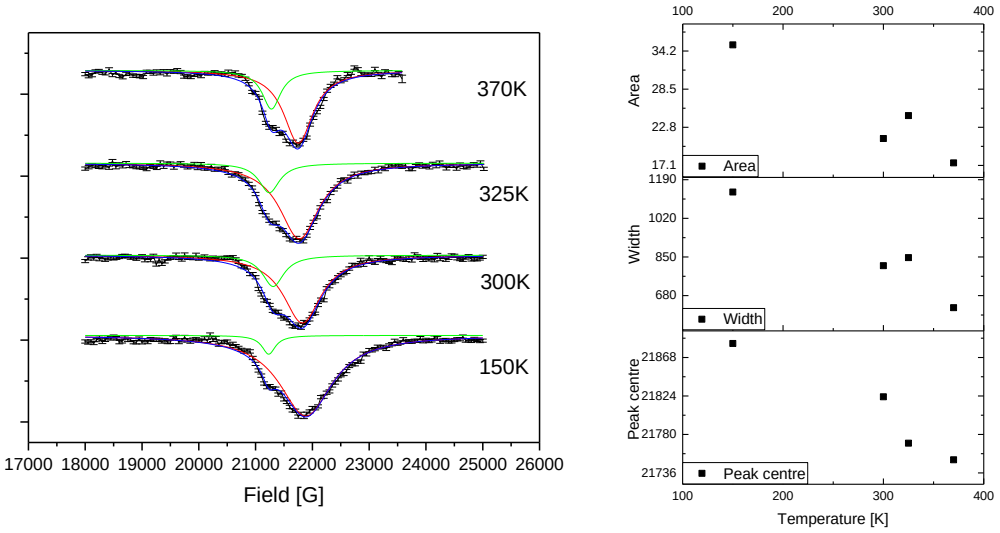

Figure 58 Solid state ALC spectra of tetrakis (2-phenylethynyl) silane molecule

A new set of scans was run with a new batch of purer model molecule (Figure 58). Peak changes with temperature the same way as before. It also corrects the exceptional behaviour in high temperature (Figure 57.a), which might be caused by melting or extraction of the impurity. Meanwhile, the higher resolution of the scan and the higher

purity of the sample give a clear separation of two signals. One at 2.1 T and another around 2.2 T.

5.4.2. Solution state spectroscopy

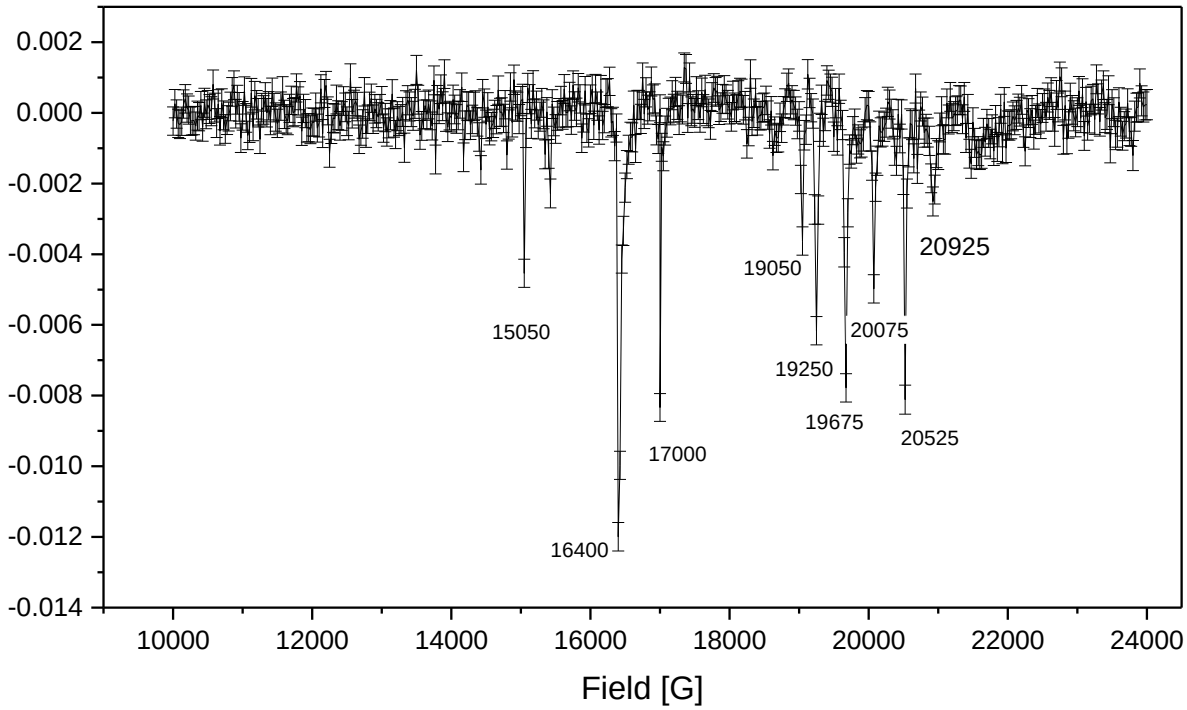

Figure 59 Solution state ALC of tetrakis (2-phenylethynyl) silane molecule

Solution prepared by dissolving molecule sample in THF was scanned within the same range as the solid-state samples but in a much higher resolution (Figure 59). Resulting peaks fall into two clusters. One centred in 1.6 T was hardly shown in solid state spectrum even within the possible shifting range. The one conjugated around 2 T shows a resemblance to the figures seen in solid state scans.

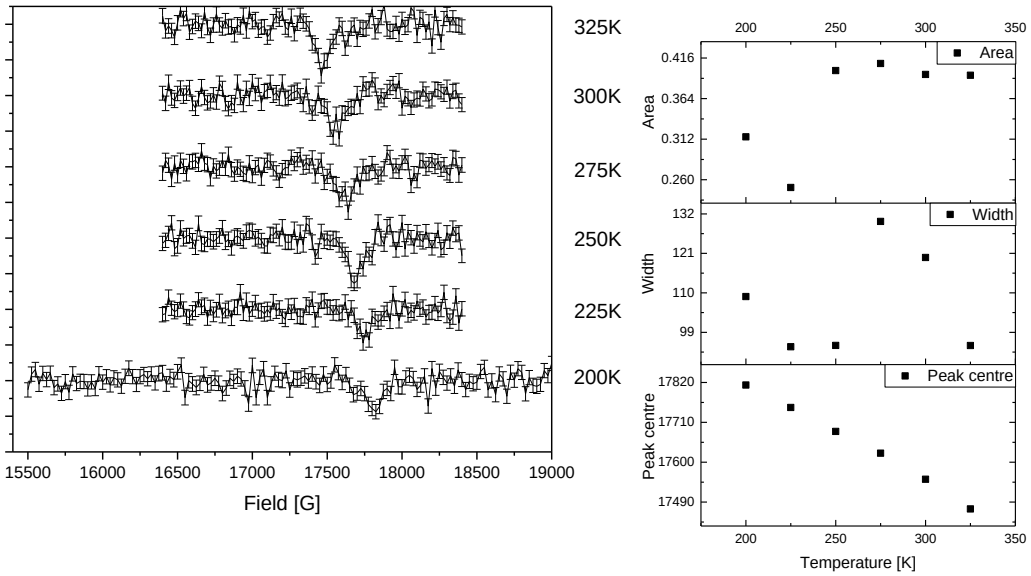

Figure 60 Solution state ALC spectra of SiNPs

Nanoparticle solution results show a clear temperature-dependent shift of peak position (Figure 60). The scan range only covers the first cluster seen in model molecule spectrum (Figure 59). The peaks and the cluster share the same asymmetry, which is due to the hyperfine anisotropy.[11]

5.4.3. TF-μSR spectroscopy

Transverse field μSR (TF- μSR) has been done in GPD at PSI. Two attempts regarding magnetic field are conducted at 2000 G and then 1000 G to get the optimum condition as well as testing how many events are needed to get a sufficient signal to noise ratio.

As seen in Figure 61, with different external fields at 1000 and 2000 G, the Fourier transform TF-μSR spectra (Figure 61) presents a pair of peaks in slightly shifted positions. Green spectra are related to results at 2000 G and the FT spectrum gives peaks at 145 and 210 MHz. Red spectra are obtained with a 1000 G external field and FT spectrum shows signals at 153 and 202 MHz. While the signals in FT spectra shifted, the correlation peak position stays the same at 356 MHz as other conditions are not altered.[7] This correlation

peak is related to the one prime location where the muonium addition happens.[12] The correlation function in use is from WiMDA software developed specifically for muon spectroscopy, as well as the background subtraction and Fourier transform.[13]

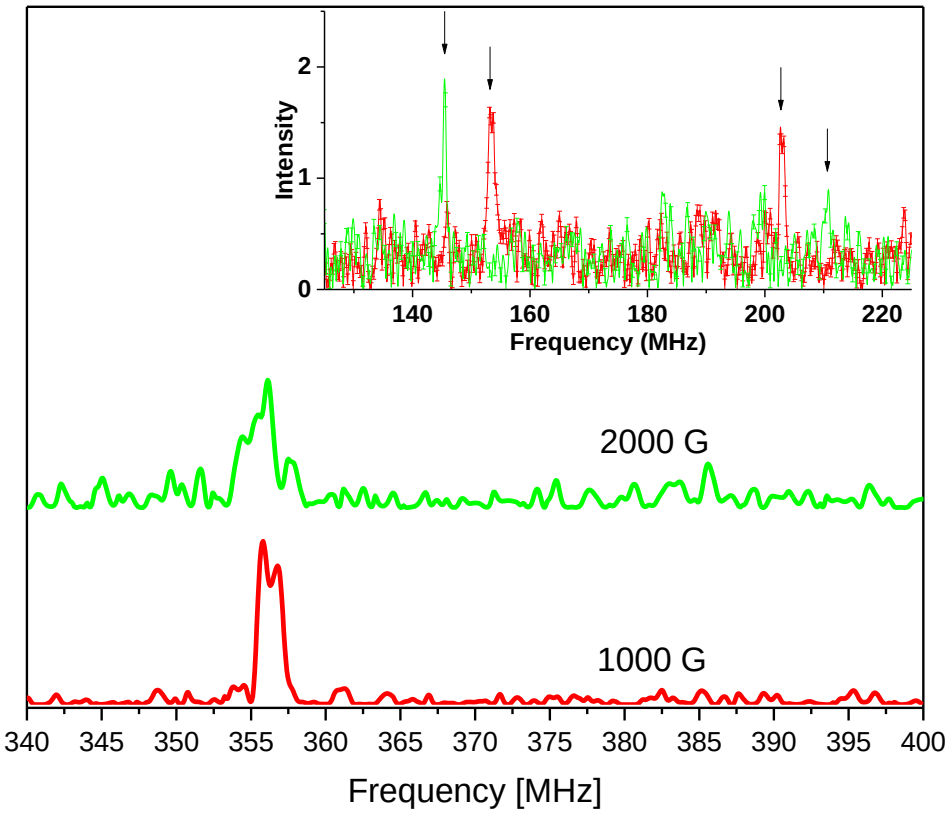

Figure 61 TF-μSR Fourier-transform spectra (up-right corner) and correlation spectra of SiNPs solution in different fields

With the correlation function proven to be working as expected, temperature effects of the SiNPs solution analysed. Three different temperatures are chosen for this analysis due to limitation of solvent boiling point, sample solubility and beamtime. At 325 K, the signal is strong and narrow due to the efficient dynamical orientational averaging of the hyperfine anisotropy.[4] With the temperature dropping from 325 K to 300 K and finally

to 250 K, the correlation peak position shifts to higher position from 353 to 360 MHz but the peak width decreases slightly(Figure 62).[14] Similar trend is found in ALC experiment.

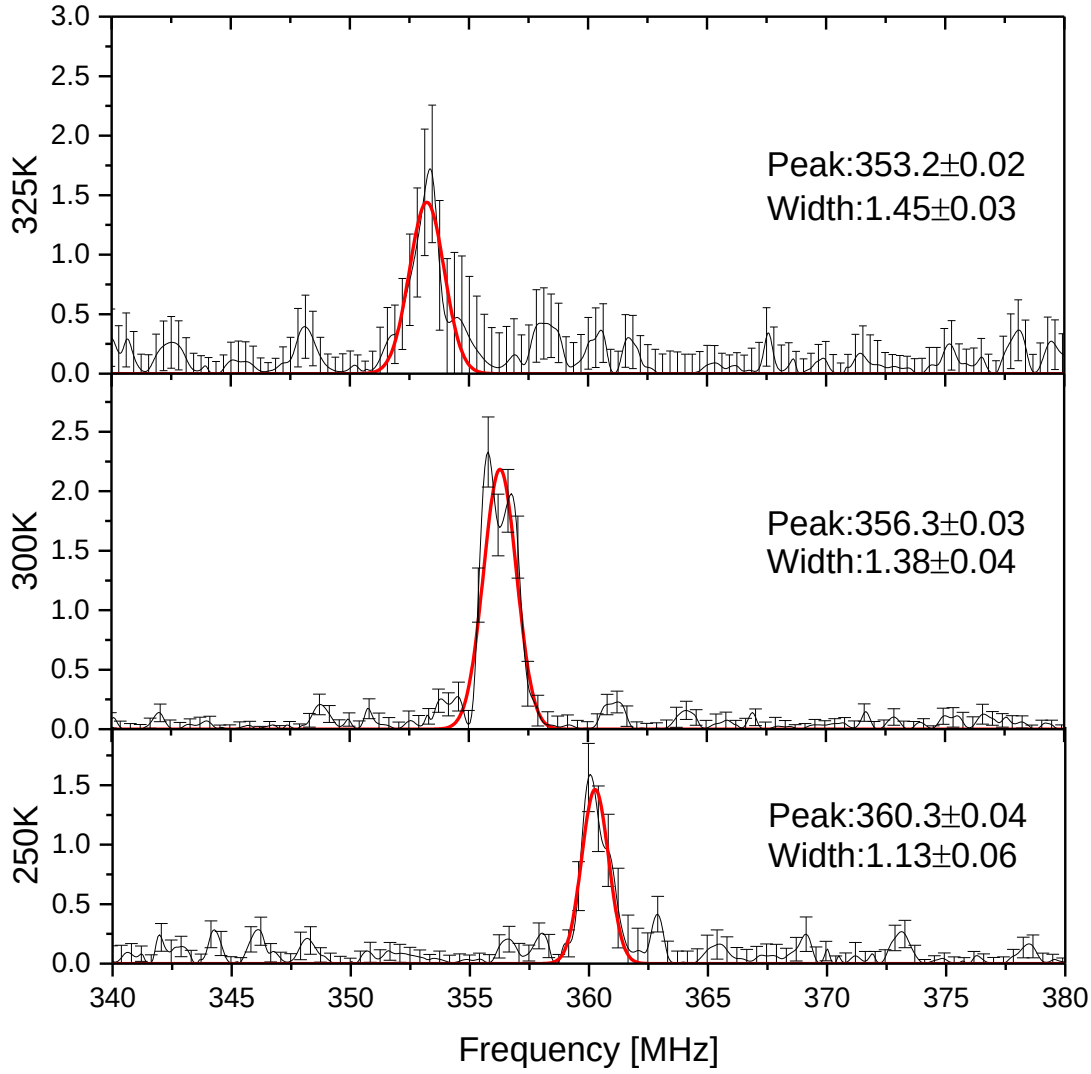

Figure 62 Correlation spectra of SiNPs solutions at three different temperatures in 1000 G

5.5. Discussions

5.5.1. Determination of muon adduct sites

When the muonium is formed by combining a positive muon with an electron, the particle behaves like a hydrogen. In order to form radicals, the isotopes would allocate to different adduct sites on unsaturated bonds or aromatic rings in the phenylacetylene ligands. These positions and their associated coupling constant can be calculated by the DFT simulation.

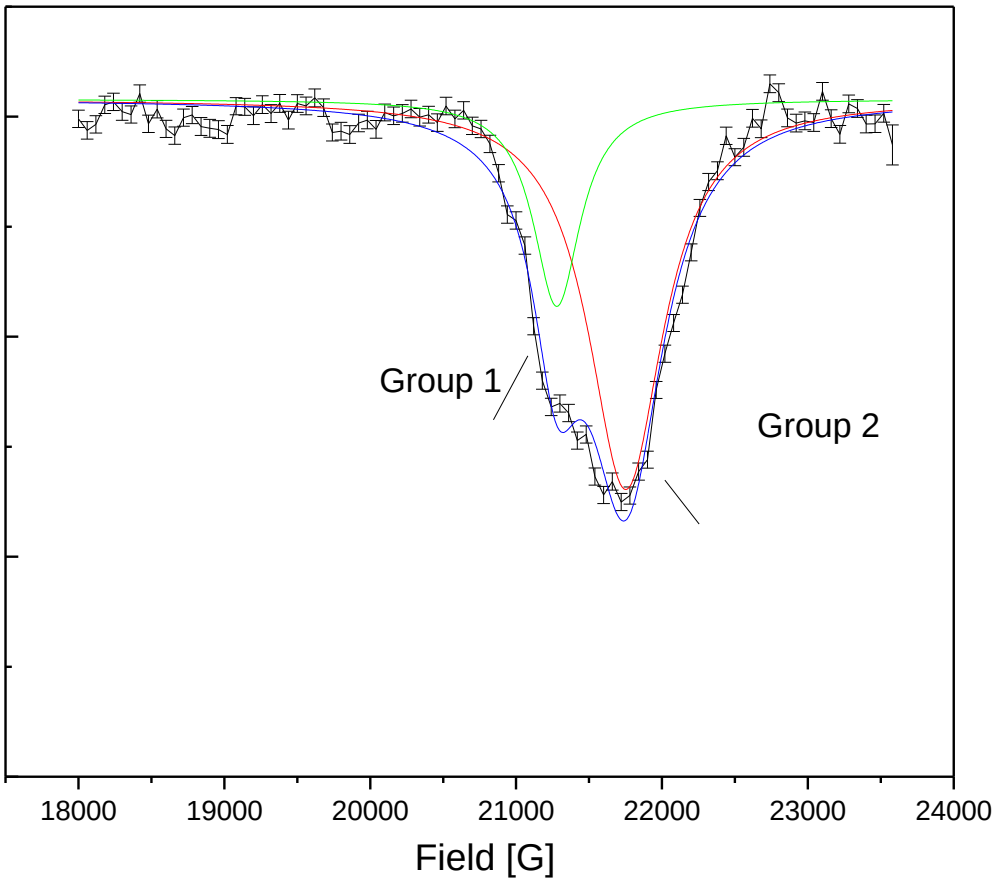

Figure 63 Solid state ALC of model molecule

The modelling gave all resonances of the ALC spectra and the hyperfine coupling constant values. When allocating peaks with computational values, in Figure 63, Group

1 is assigned to C1, and Group 2 is C4/8 and C5/7. C3 is a tertiary carbon and not a suitable site for muonium as it prefers a secondary carbon.[15] C2 is related to peak in higher field and C6 in lower field.

The solution state spectrum in Figure 59 shows a similar situation. Peaks between 1.4 and 2.1 T fall into two groups with peaks in lower field assigned to C6.

When it comes to phenylacetylene capped SiNPs, muon addition reaction is highly limited by steric effects, with only one location being observed as muon adduct site. As indicated in Figure 60 and Figure 62, only one type of hyperfine interaction occurs in SiNPs solution. (Splitting in correlation spectrum is false positive as there is no indication in the corresponding FT spectrum)

5.5.2. Temperature dependence and electron transfer

As shown in ALC spectra, temperature plays an important role in the resonance.

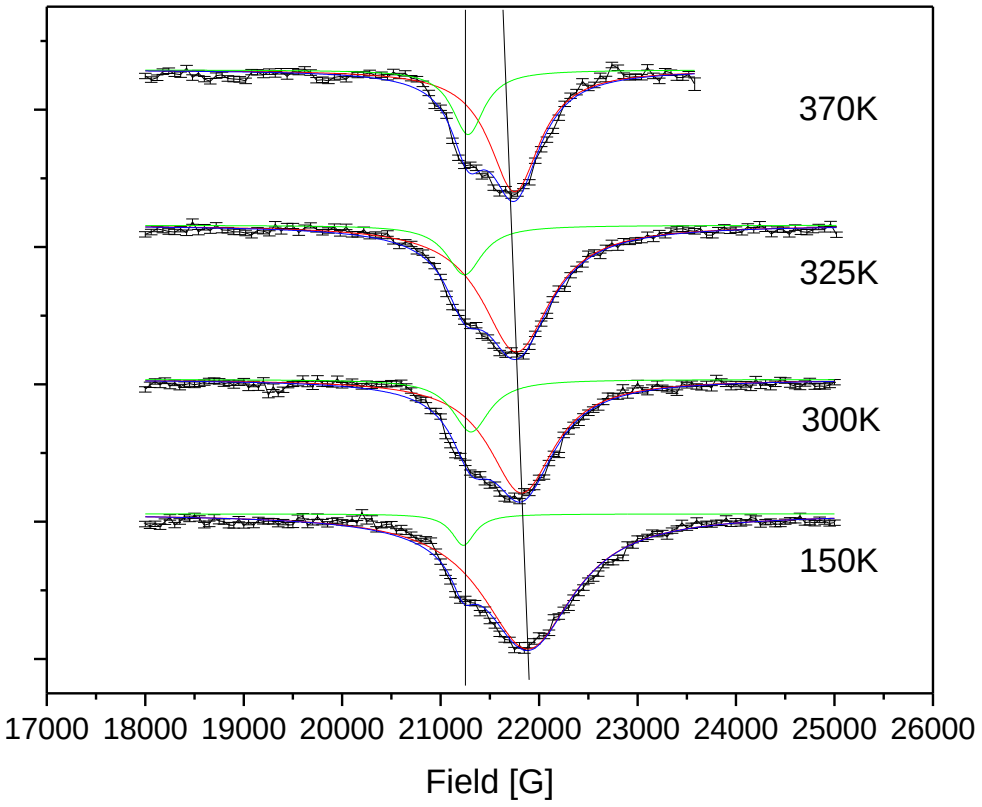

Figure 64 Solid state ALC spectra of model molecule at four different temperatures

Figure 64 shows the influence of temperature on the peak positions. By comparing results from four different temperatures at 370, 325, 300 and 150 K, certain trends are observed.

As temperature drops, Group 1 stay in the same position while Group 2 shift into higher field. While assuming the torsional energy falls in a Boltzmann population, the thermodynamic rotation of phenyl group about C1-C2 bond direction develops a rotation barrier.[16] This temperature dependent energy barrier results in the temperature dependence of coupling constant following the Boltzmann average function:[16]

$$\mathrm{Ae\mu(T)} = \frac{\sum_i Ae^{-E_i/k_BT}}{\sum_i e^{-E_i/k_BT}}$$

The higher temperature induces a more rapid rotation and hence a lower hyperfine coupling constant value.

The spin rotation of phenyl group doesn't affect Group 1 as the carbon is on the rotation axis.

Same situation occurs when it comes to solution sample shown in Figure 65.

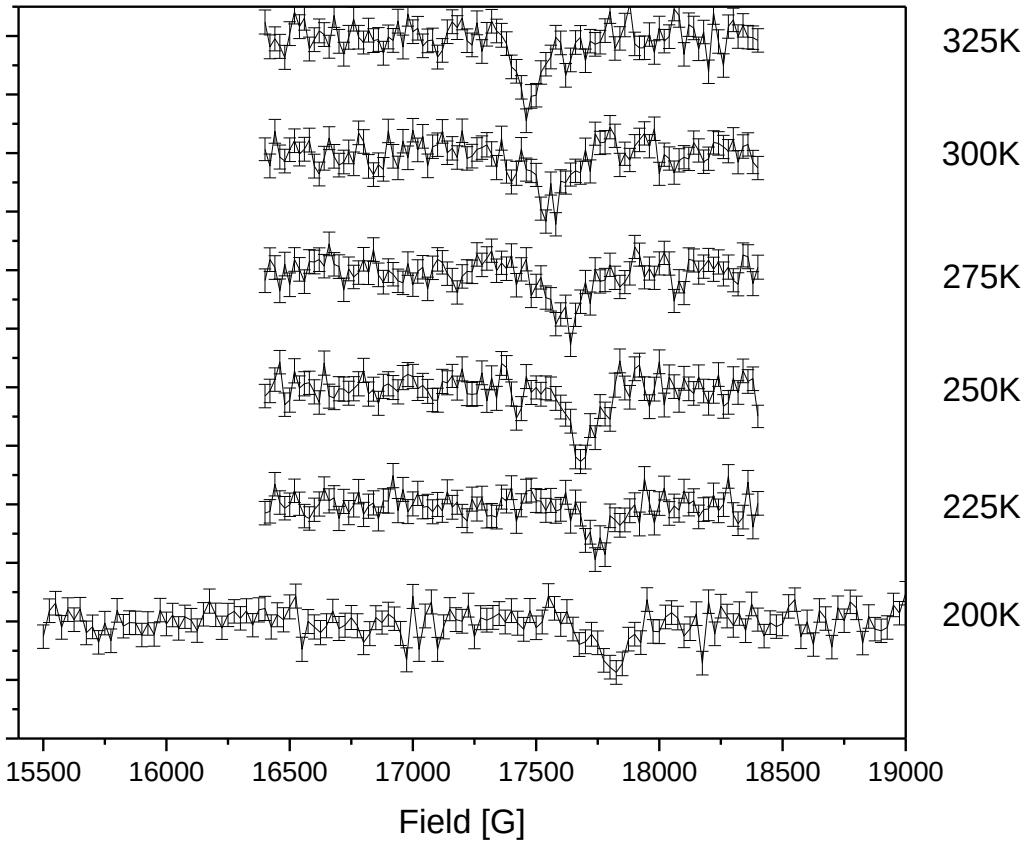

Figure 65 ALC spectra of SiNPs solution at six different temperatures

In solution, the rotation of nanoparticles obeys the same rule, causing the peak position shifting to higher field as temperature drops. The single resonance peak is assigned to C6, which does not rotate in the solid state. However, the rotation of nanoparticle itself

follows the principle of thermodynamics, resulting in energy barrier changes dependent on temperature.

The integral asymmetry of resonance shares the same trend. The peak area increases as the temperature gets lower. With the data fitting into an Arrhenius model, this indicates a vibrational contribution to the resonance. At higher temperature, the increasing thermodynamic movements in ligands lead to weaker signals suggesting process falls out of muon time window of measurement.

When comparing the two samples, solid state resonance shows stronger signal in SiNPs than model molecule. The lower flexibility of ligands on nanoparticles gives a stable target for muonium to attach. The stalking of phenyl groups makes a pathway for the free electrons to travel across and between the ligands and the silicon nanoparticles.

Reference

1. L. Schulz, K. Wang, M. Willis, L. Nuccio, P. Murahari, S. Zhang, F. L. Pratt, J. S. Lord, N. A. Morley, C. Bernhard, and A. J. Drew, *Journal of Physics: Conference Series* 551, 012042 (2014).

2. K. Venkateswaran, M. V. Barnabas, Z. Wu, J. M. Stadlbauer, B. W. Ng, and D. C. Walker, *Chemical Physics* 137, 239 (1989).

3. I. McKenzie, and E. Roduner, *Naturwissenschaften* 96, 873 (2009).

4. S. J. Blundell, *Chem Rev* 104, 5717 (2004).

5. I. McKenzie, *Journal of Physical Chemistry A* 114, 12759 (2010).

6. V. S. Oganesyan, A. N. Cammidge, G. a. Hopkins, F. M. Cotterill, I. D. Reid, and U. a. Jayasooriya, *Journal of Physical Chemistry A* 108, 1860 (2004).

7. J. Lord, *Physica B: Condensed Matter* 374, 472 (2006).

8. T. Bian, J. N. Peck, S. P. Cottrell, U. A. Jayasooriya, and Y. Chao, *Journal of Electronic Materials* 46, 3221 (2017).

9. N. J. Clayden, *Physica Scripta* 88, (2013).

10. I. McKenzie, *Annual Reports Section "C" (Physical Chemistry)* 109, 65 (2013).

11. E. Roduner, K. Prassides, R. M. Macrae, I. M. Thomas, C. Niedermayer, U. Binninger, C. Bernhard, A. Hofer, and I. D. Reid, *Chemical Physics* 192, 231 (1995).

12. B. W. Lovett, S. J. Blundell, J. S. Stiessberger, F. L. Pratt, T. Jestaadt, W. Hayes, S. P. Cottrell, and I. D. Reid, *Physical Review B* 63, (2001).

13. F. L. Pratt, *Physica B: Condensed Matter* 289-290, 710 (2000).

14. F. L. Pratt, S. J. Blundell, T. Jestadt, B. W. Lovett, R. M. Macrae, and W. Hayes, *Magnetic Resonance in Chemistry* 38, S27 (2000).

15. I. McKenzie, *The Journal of Physical Chemistry A* 114, 12759 (2010).

16. M. J. Ramos, D. McKenna, B. C. Webster, and E. Roduner, *Journal of the Chemical Society, Faraday Transactions 1: Physical Chemistry in Condensed Phases* 80, 255 (1984).

Chapter 6 Conclusions and future work

The solution reduction synthesis method is proven to be an efficient way in producing surface-functionalized silicon nanoparticles. Thiophene oligomer capped SiNPs show a great potential in the application as thermoelectric material, especially after oxidation and graphene doping. However, there is a lot of room for improvements in several aspects not only in the way of what contents could be used but also how the material could be constructed.

Contents

6.1. Conclusions

6.1.1. Monomer and oligomer capped nanoparticles

The solution reduction synthesis method appears to be the way of manufacturing several types of ligands capped silicon nanoparticles under similar reaction conditions, as shown in chapter 3 and 5. Although the surface coverage and surface oxidation level varies between ligands, there is no denying that the method combines silicon nanoparticles and conjugated organic compounds to create the hybrid obtaining advantages from both sides. $NOBF_4$ doping of the ligands appears to be a clear effect on TE performance. With the increasing doping level, ZT shows an increase followed by a decrease with a peak around 0.5 as a common ground for hybrid materials in discussion.

6.1.2. Graphene doping

The contribution of graphene in doping thermoelectric material is impossible to ignore. The increase in electrical conductivity is noteworthy while the worrying thermal conductivity of graphene does not seem to raise any noticeable concerns. This graphene doping technique is not just for hybrid TE material but for all sorts.

6.1.3. Microscopic conductivity and muon spectroscopy

The microscopic conductivity experiments are not just a way of study the nanoparticles. With muon spectroscopy being a developing technique, experiments using molecule and nanoparticles in different physical conditions are also exploring the potential of this technique. Molecule solution with low concentration has limited numbers of precedent in muon spectroscopy, let alone nanoparticle solution.

6.2. Future work

6.2.1. Doping nanoparticles

Due to the limitation of organic polymer, materials can be doped to generate p-type TE material only. In the development of n-type capped nanoparticles, doping of the particle is a direct path. By capping undoped ligand on n-type silicon nanoparticles, the manufacture of n-type hybrid material would be expected as the counterpart of the material in hand.

6.2.2. Uniformed ligands with high coverage

Terthiophene capped SiNPs obtains a low surface coverage of ligands and in turns suffer from the higher surface oxidation level, while polythiophene capped SiNPs contains oligomer capping in different chain length and pattern. By looking at the shortcomings of previous oligomer capped SiNPs, a type of uniformed ligand with high coverage is required as ligand structure and surface coverage are two of the urgent defects affecting the performance of materials. A way of synthesizing crosslinked ligand in control would also optimise the TE performance in the way of increasing efficient doping level.

6.2.3. Muon spin spectroscopy

In the case of muon spectroscopy, microscopic conductivity measurement has the potential of being introduced to other materials. The study of this technique is not limited to nanoparticles or conjugated organic compounds.